Studying biosphere-atmosphere exchange of CO$_2$ through Carbon-13 stable isotopes

Ivar van der Velde

Thesis committee

Promotors

Prof. Dr M.C. Krol
Professor of Air Quality and Atmospheric Chemistry
Wageningen University

Prof. Dr W. Peters
Professor of Atmospheric Composition Modeling
University of Groningen
Associate professor, Meteorology and Air Quality Group
Wageningen University

Co-promotor

Dr J.B. Miller
Senior Research Scientist
National Oceanic and Atmospheric Administration – Earth System Research Lab, Boulder, US
Cooperative Institute for Research in Environmental Sciences, University of Colorado, Boulder, US

Other members

Prof. Dr M. Herold, Wageningen University
Dr S. Houweling, Netherlands Institute for Space Research, Utrecht, the Netherlands
Prof. Dr H. Meijer, University of Groningen, the Netherlands
Prof. Dr E. Moors, Wageningen University

Studying biosphere-atmosphere exchange of CO_2 through Carbon-13 stable isotopes

Ivar van der Velde

Thesis

submitted in fulfilment of the requirements for the degree of doctor

at Wageningen University

by the authority of the Academic Board,

in the presence of the

Thesis Committee appointed by the Academic Board

to be defended in public

on Friday 5 June 2015

at 01.30 p.m. in the Aula.

Contents

Chapter 1

Introduction

1.1 Background

Prediction of the Earth's climate is difficult due to large uncertainties in the global carbon cycle and its future fate. The carbon cycle is a natural process that has been ongoing throughout the Earth's history; it is the biogeochemical cycle by which carbon is exchanged among the biosphere, hydrosphere, and atmosphere of our planet. Since the industrial revolution, anthropogenic activity has modified the carbon cycle by changing its components' functions and directly adding carbon to the atmosphere. There is an accelerating rate of carbon dioxide (CO_2) emissions from fossil fuel combustion, but the rate of carbon storage by the natural ecosystems is not keeping pace. We particularly lack a good understanding of the carbon cycle in the terrestrial biosphere [*Cox et al.*, 2013]. If the terrestrial biosphere were to maintain its current carbon absorption rate, atmospheric CO_2 abundance will likely reach 600 parts per million (ppm) around 2050 [*Ciais et al.*, 2013]. This is an increase of 50% over 2015 levels; an enormous rate of change over a relatively short time span. In contrast, it took over 260 years to raise CO_2 levels by 40%, from 280 ppm since the start of the industrial revolution in the 1700s to the current level of 400 ppm.

CO_2 is the primary anthropogenic greenhouse gas: i.e., it impacts the radiative forcing and temperature of the Earth's surface. The radiative forcing of CO_2 from 1750 to 2011 has been estimated at $1.82\,\mathrm{W\,m^{-2}}$, comprising 80% of the total increase in greenhouse gas radiative forcing [*Myhre et al.*, 2013]. Consequently, the increases in global mean temperatures in recent years are attributed primarily to increasing CO_2 levels. Model projections show possible temperature increases of 1.4 to $3.0\,^{\circ}\mathrm{C}$ by 2050 [*Rowlands et al.*, 2012]. Such changes will affect most ecosystems on Earth, but the impact on the ecosystem services they provide, such as food production, is of paramount concern

to low-income countries [*Mora et al.*, 2013a]. Changes in precipitation patterns, and the melting of snow and glaciers will alter the hydrological cycle and thus the availability of water resources [*IPCC*, 2014]. Food security will also be affected through the impact of altered weather patterns on crop and animal disease epidemics [*Garrett et al.*, 2011]. There is little doubt that low-income countries will remain on the frontline of human-induced climate change over the next century.

Another harmful consequence of the rapid increase of atmospheric CO_2 is ocean acidification. As more anthropogenic carbon is dissolved in the surface layers of the oceans, the acidity of the seawater rises due to changes in the chemical balance between dissolved CO_2, carbonic acid, and bicarbonate and carbonate ions [*Rhein et al.*, 2013]. The projected decrease of ocean pH in the 21st century in combination with other ocean biogeochemical changes could deteriorate the functioning of marine biota [*Mora et al.*, 2013b]. Corals and phytoplankton will find it increasingly difficult in the future to maintain their calcium carbonate skeletons under higher acidity levels. By 2050, some of the Southern ocean waters could become undersaturated in calcium carbonate to a point that the shell structure of organisms starts to dissolve [*Orr et al.*, 2005].

The development of strategies to mitigate climate forcing from increased atmospheric CO_2 require a better understanding of the global carbon cycle and improvement of monitoring techniques. We know the global distribution of CO_2 relatively well due to an extensive monitoring network of observations. What is still highly uncertain is the capacity of the oceans and terrestrial biosphere to absorb a large fraction of the CO_2 emitted by fossil fuel combustion [*Tans et al.*, 1990]. Currently around 50% of the carbon from anthropogenic CO_2 emissions is absorbed by the oceans and terrestrial biosphere, but the future rate of uptake is hard to predict. In the terrestrial biosphere the net uptake of CO_2, or the net ecosystem production (NEP), depends on two larger fluxes: the gross primary production (GPP), and terrestrial ecosystem respiration (TER). Both of these fluxes are highly dependent on environmental conditions, such as temperature, precipitation, radiation, and nutrients [*Friedlingstein et al.*, 2006]. For example, extreme drought can force GPP to decrease and TER to increase to a point where regional NEP is reversed from a carbon sink to a carbon source [*Ciais et al.*, 2005]. These dynamic responses and climate-carbon feedbacks are now an integral part of climate models and can help us to predict the carbon cycle given a climate scenario where droughts are more extreme and more frequent [*Booth et al.*, 2012, *Dai et al.*, 2012]. The magnitude of these responses to droughts and changes in environmental conditions is still uncertain. Efforts to reduce these uncertainties open new research avenues that can help to narrow the range of possible projections of climate forcing and ocean acidification.

Currently we can monitor ongoing changes in the carbon cycle using different methods: (1) accounting techniques to estimate carbon stocks; (2) a wide range of observational data from different ecosystems and the atmosphere, including data from remote areas using space-borne platforms; and (3) detailed modeling of all the important processes involved. Each of these methods has its own utility and although it is often advantageous to combine them, these approaches still do not provide the complete picture. To bridge the gap between these information streams we must employ a more integrated approach. Such a system would include process-based carbon cycle models, atmospheric transport modeling, multiple streams of observational data, and a data-assimilation method to combine them all. Before such a system is fully operational, fundamental scientific research on all components must be completed. The work described in this thesis details a novel approach to understanding some of the important processes of the carbon cycle, and aims to provide new observational constraints.

1.2 CO_2 budget

In the atmosphere CO_2 is the most abundant trace gas containing carbon. The Fifth Assessment Report of IPCC reported a global average concentration of 390.5 ppm for 2011, which corresponds to an atmospheric mass of 828 Pg carbon (Pg C, Petagram=10^{15} grams, *Ciais et al.* [2013]). These estimates are derived from a large collection of sampling sites combined in the Greenhouse Gas Reference Network of the National Oceanic and Atmospheric Administration/Earth System Research Laboratory (NOAA/ESRL). CO_2 together with other atmospheric trace gases play an important role in establishing the global energy balance that makes terrestrial and marine life possible. The atmosphere is relatively transparent for solar shortwave radiation, therefore absorption mostly takes place at the Earth's surface. The Earth emits longwave radiation that interacts with greenhouse gases, as these absorb and emit the terrestrial radiation very effectively [*Hartmann*, 1994]. The interactions of greenhouse gases with radiant energy are a key component of the Earth's climatic state. The rise in CO_2 from 278 ppm in 1750 to 390.5 ppm in 2011 originates from the combustion of fossil fuels. The longest record of direct CO_2 measurements in the atmosphere started in the late 1950s at the Mauna Loa Observatory in Hawaii [*Keeling et al.*, 1976], which currently (2015) shows a growth rate of approximately 2 ppm yr^{-1}, and a concentration of approximately 400 ppm (Figure 1.1). Historical mole fractions of atmospheric CO_2 were determined from ice-core measurements [*Etheridge et al.*, 1996].

A large proportion of CO_2 comes from anthropogenic activities. For the period 2002-2011 the average fossil fuel-derived flux (rate of flow) was estimated at 8.3±0.7 Pg C yr^{-1}

[*Boden et al.*, 2011, *Ciais et al.*, 2013]. Around 96 % of these CO_2 emissions originate from the combustion of fossil fuels (coal, gas, oil) for energy consumption. Cement production is the second major cause. Total CO_2 emissions have increased by $3.2 \% \, yr^{-1}$ over the last decade (2000-2009), in comparison to a lower increase of $1.0 \% \, yr^{-1}$ in the 1990s, and $1.9 \% \, yr^{-1}$ in the 1980s [*Ciais et al.*, 2013]. Considering all carbon sources and sinks, the fossil fuel and cement flux term has the smallest relative uncertainty of 8 %. This value increases, however, as a result of emissions from emerging economies with less reliable energy statistics [*Gregg et al.*, 2008].

An additional source of CO_2 comes from land-use change (LUC). LUC refers to different activities, such as deforestation (removal or burning of trees to change the land usage), afforestation (deliberate planting of new trees), and regrowth of vegetation on abandoned land [*Ciais et al.*, 2013]. The latest estimate for the period 2002-2011 is $0.9 \pm 0.8 \, Pg\,C\,yr^{-1}$. Another 1 to 2 $Pg\,C\,yr^{-1}$ originates from naturally recurring wildfires, but this source is often accounted for as part of the gross respiration CO_2 flux over land (such as in IPCC).
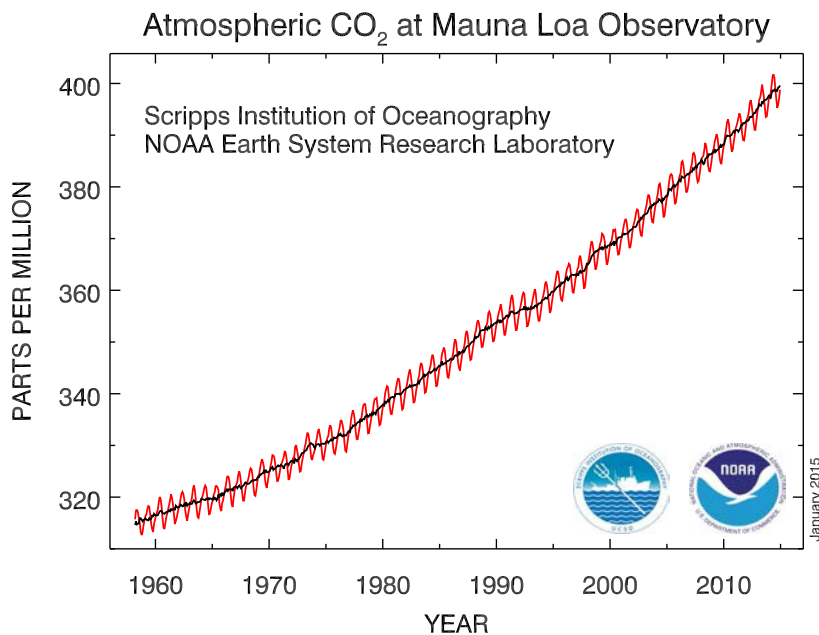
FIGURE 1.1: Observed atmospheric CO_2 record (red curve) and the long-term trend (black curve) at the Mauna Loa Observatory, Hawaii, United States. This is the oldest record of directly measured CO_2 [source: NOAA/ESRL].

In the terrestrial biosphere CO_2 is absorbed and released by plant and microbial life. The main process responsible is photosynthesis, which absorbs approximately $120 \, Pg\,C\,yr^{-1}$ from the atmosphere (gross primary production, or GPP). It is the process used by plants and other organisms to create chemical energy and oxygen from sunlight, CO_2,

and water [*Rabinowitch and Govindjee*, 1969]. There are three main metabolic pathways for carbon fixation: C_3, C_4, and CAM [*Leegood*, 2000].

The C_3 type plants are the most abundant on Earth (95 % of all plant biomass) and thrive in areas with moderate sunlight intensity and cool temperatures. Most plant and tree species use C_3 metabolism, including some of the major crops, such as rice and barley. It is not the most efficient carbon fixation pathway, however. Under higher temperature regimes C_3 plants lose large amounts of water and their CO_2 uptake is limited. In these more extreme regions other metabolic pathways perform better. The C_4 type of metabolism has a uniquely modified biochemistry and leaf anatomy to avoid the inefficiencies in C_3 metabolism that arise in more hot and arid environments [*Furbank et al.*, 2000]. Typically, C_4 plants are grasses located around the tropical latitudes and crops growing at the midlatitudes, such as maize and sugar cane. In the most arid environments, plants such as cacti often use the Crassulacean acid metabolism (CAM). In some of those species CO_2 uptake occurs exclusively at night as stomata are fully closed during the day to prevent evaporative water loss [*Herrera*, 2009].

Besides the large influx of carbon through photosynthesis, there is an almost equivalent return flux of CO_2 back to the atmosphere. Approximately half of the GPP is returned to the atmosphere within a few days in the form of autotrophic respiration. This flux results from maintenance respiration in leaves, stems and roots to keep the existing plant biomass alive and functioning. The remainder of the GPP is the net primary production (NPP), most of which is eventually released back to the atmosphere as heterotrophic respiration at different time intervals; bacteria, fungi and soil organisms decompose plant organic matter and respire CO_2 back to the atmosphere. As mentioned earlier, a smaller fraction of CO_2 returns to the atmosphere as a result of wildfires. The averaged net sink over land is estimated at $-2.5 \pm 1.3 \, \mathrm{Pg \, C \, yr^{-1}}$ for the period 2002-2011 [*Ciais et al.*, 2013].

Over the oceans air-sea gas exchange of CO_2 occurs. It is typically computed using the observed partial pressure difference of CO_2 between atmosphere and seawater, the solubility of CO_2 in seawater and the gas transfer velocity [*Rhein et al.*, 2013]. The IPCC reported an averaged net carbon sink of $-2.4 \pm 0.7 \, \mathrm{Pg \, C \, yr^{-1}}$ for the period 2002-2011, resulting from two much larger gross fluxes of around $80 \, \mathrm{Pg \, C \, yr^{-1}}$ in and out of the ocean [*Ciais et al.*, 2013]. The absorbed CO_2 in seawater is converted into dissolved inorganic carbon becoming available for phytoplankton to photosynthesize. The amount of inorganic carbon in the oceans is estimated to be 50 times larger than the amount stored in the atmosphere [*Sabine et al.*, 2004].

The global growth rate of carbon in the atmosphere (C_a in the form of CO_2) can be described in the following mass balance equation:

$$\frac{\mathrm{d}}{\mathrm{d}t} C_a \;=\; \underset{(4.3)}{F_{ff}} \;+\; \underset{(8.3)}{N_{bio}} \;+\; \underset{(-1.6)}{N_{oce}}. \underset{(-2.4)}{} \tag{1.1}$$

The different carbon flux terms are separated as follows: fossil fuel combustion and cement production (F_{ff}), net exchange over land, including land-use change (LUC), forest fires and forest regrowth (N_{bio}), and net exchange over the oceans (N_{oce}). The sum of the averaged fluxes (2002-2011 given in parentheses under Equation 1.1, based on *Ciais et al.* [2013]) equals an averaged growth rate of $4.3\,\mathrm{Pg\,C\,yr^{-1}}$ in the atmosphere, which is approximately equivalent to the $2\,\mathrm{ppm\,yr^{-1}}$ increase observed at Mauna Loa (Figure 1.1).

The research community has come a long way to understanding the global carbon budget as depicted in Equation 1.1, but there are still large uncertainties, especially in N_{bio} and N_{oce}. The starting point of this thesis research was therefore to investigate whether other observations besides CO_2 can provide an additional constraint on the global carbon budget. Special emphasis was put on the use of Carbon-13 (^{13}C) in CO_2. As explained in the following sections, under the right circumstances Carbon-13 can help us recognize changes in plant photosynthesis under extreme drought. Until now, efforts to use these isotope measurements in an integrated data-assimilation system have been very limited.

1.3 $^{13}CO_2$ budget

Interestingly, the exchange of CO_2 between the atmosphere and the Earth's surface relates to more than just one isotopologue. In nature different carbon isotopes exist (Figure 1.2). The most common natural stable isotope is Carbon-12 (^{12}C), which makes up $98.9\,\%$ of all carbon on Earth [*Chang*, 2005]. In the atmosphere it forms the abundant trace gas $^{12}CO_2$ as well as other molecules such as $^{12}CH_4$ and ^{12}CO. The isotope ^{12}C contains 6 neutrons and 6 protons [*Greenwood and Earnshaw*, 1997]. The isotope with an additional neutron is Carbon-13 (^{13}C), which is also a natural stable isotope and constitutes almost the remainder of all Earth's carbon [*Chang*, 2005]. Only a small fraction of all natural carbon exist as Carbon-14 (^{14}C) and is radioactive with a half-life of 5715 years [*Greenwood and Earnshaw*, 1997]. Because dead plant matter and organisms slowly lose ^{14}C due to radioactive decay, the detection of the remaining amount of ^{14}C is widely used in the field of archeology for dating purposes. In the atmospheric sciences ^{14}C is also becoming a tool to inform us on regional fossil fuel emissions using the notion that the ^{14}C content in fossil fuels have long since decayed [*Levin et al.*, 2003].
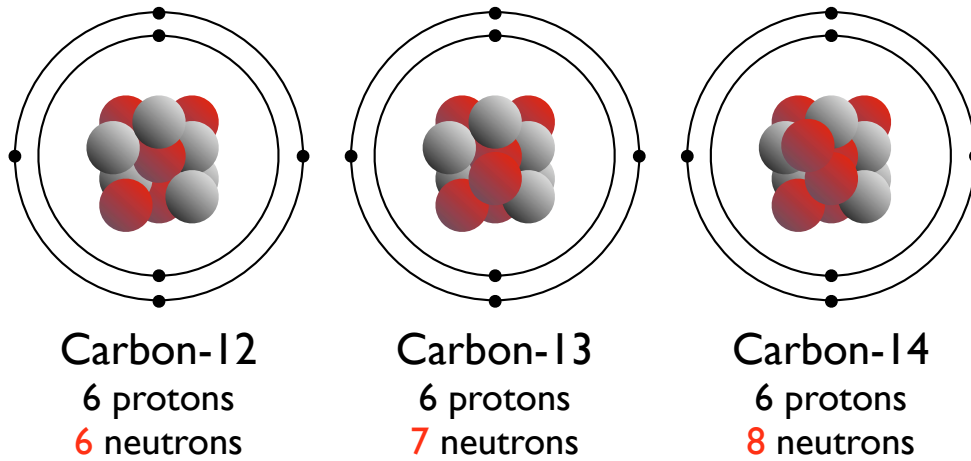
FIGURE 1.2: The three naturally occurring carbon isotopes: Carbon-12, Carbon-13 and Carbon-14. They all have the same number of positively charged protons giving them the atomic number of 6, but each have a different atomic mass due to different numbers of zero charge neutrons. [image inspired by Press and Siever, 2007]

The $^{13}CO_2$ molecules are advected, transferred, exchanged, and photosynthesized just like the more abundant $^{12}CO_2$ molecules. Slight preferences for the lighter $^{12}CO_2$ during exchange and enzymatic processes, however, can change the relative atmospheric $^{13}CO_2/^{12}CO_2$ ratio and likewise the $^{13}C/^{12}C$ ratio (R_{sample}) in biological material [*Ciais et al.*, 1995]. As changes in R_{sample} are usually small it is customary to report this ratio as $\delta^{13}C$ in per mille (‰). Throughout this thesis we refer to $\delta^{13}C$ as the isotopic signature or isotopic composition and its values differ with respect to an established reference material R_{ref}:

$$\delta^{13}C = \left(\frac{R_{sample} - R_{ref}}{R_{ref}} \right) \cdot 1000. \tag{1.2}$$

R_{ref} is the reference standard Vienna Pee Dee Belemnite (VPDB), which is based on the original PDB material from a Cretaceous marine fossil *Belemnitella Americana* that was collected from the Pee Dee river in South Carolina. This material had an exceptionally high $^{13}C/^{12}C$ ratio (0.0112372) and was chosen as a baseline ratio for $^{13}C/^{12}C$ [*Craig*, 1957]. As a consequence, most of the other $^{13}C/^{12}C$ samples measured on Earth are smaller than VPDB.

Direct $^{13}C/^{12}C$ measurements from the atmosphere have been made regularly since 1991

at the Institute of Arctic and Alpine Research (INSTAAR). Prior to this it was measured at a limited number of sites, e.g., by groups at Scripps Institution of Oceanography (SIO) and Commonwealth Scientific and Industrial Research Organization (CSIRO) [*Fung et al.*, 1997]. As is the case for CO_2, a global network of $\delta^{13}C$ observations is available. Fossil fuel combustion not only increased CO_2 levels but also had an impact on the depletion of atmospheric $\delta^{13}C$ levels in CO_2 [*Bush et al.*, 2007]. From additional ice-core measurements [*Francey et al.*, 1999] it was determined that since the industrial era $\delta^{13}C$ decreased from around $-6.4\,‰$ to the current levels (2015) of $-8.4\,‰$. The depletion effect is illustrated in the timeseries diagram of atmospheric $\delta^{13}C$ in Figure 1.5b on page 18. This effect was originally discovered in the atmospheric ratio of ^{14}C to ^{12}C by Hans Suess in the 1950s [*Bowling et al.*, 2014]. Carbon emitted by fossil fuel combustion was old enough to have all the ^{14}C removed, therefore fossil fuel combustion was an important source for ^{14}C depletion. It not only changed the $^{14}C/^{12}C$ ratio in atmospheric CO_2 but also altered the $^{14}C/^{12}C$ ratio in wood due to photosynthetic carbon uptake [*Suess*, 1955]. This effect is now known to us as the 'Suess-effect' and the term was subsequently used by *Keeling* [1979] to indicate the decrease in $\delta^{13}C$ due to the addition of ^{13}C depleted CO_2 from fossil fuel combustion.

The uptake of $^{13}CO_2$ molecules over the oceans and the terrestrial biosphere proceeds less easily than the uptake of $^{12}CO_2$ molecules. That means that for each mole of CO_2 that is removed from the atmosphere a relatively higher amount of $^{13}CO_2$ than $^{12}CO_2$ stays behind in the atmosphere. Carbon uptake thus has an enriching effect on the isotopic composition of the atmosphere, an opposite tendency against the strong draw down by fossil fuel combustion (i.e., carbon uptake works against the downward trend in $\delta^{13}C$). This effect is especially visible at seasonal scales. As illustrated in Figure 1.5, the timeseries diagram on page 18, uptake lowers the seasonal CO_2 concentrations, but it simultaneously increases $\delta^{13}C$. This is because there is approximately a one order of magnitude difference in discrimination against ^{13}C between plant photosynthesis and dissolution of CO_2 in the oceans. This is due to differences in ocean and photosynthetic isotope fractionation effects [*Ciais et al.*, 1995], which are the processes that change the isotopic ratios during CO_2 exchange. This concept has been used in previous inverse modeling studies to better partition the ocean and terrestrial carbon uptake [*Ciais et al.*, 1995, *Keeling et al.*, 1989]. On regional scales, changes in atmospheric $\delta^{13}C$ reflect differences in photosynthetic fractionation [*Randerson et al.*, 2002]. Firstly, the metabolic pathways as described above discriminate differently against ^{13}C. For example, the impact of C_3 plants on the atmospheric $\delta^{13}C$ signature is fives time larger than that of C_4 plants. Secondly, photosynthetic discrimination can also vary in response to changes in environmental conditions [*Bowling et al.*, 2002, *Ekblad and Högberg*, 2001, *Suits et al.*, 2005]. Under drought stress plants close their stomata to limit evaporative water loss

while photosynthetic carbon uptake is maintained. This also reduces the fractionation in C_3 plants. Regional changes in atmospheric $\delta^{13}C$ can therefore be used to distinguish changes in photosynthetic activity resulting from drought stress [*Ballantyne et al.*, 2010]. This topic is investigated further in Chapter 3.

As for the CO_2 budget (Equation 1.1) we can describe the $^{13}CO_2$ growth rate ($^{13}C_a$) using the same fluxes in a mass balance equation:

$$\frac{d}{dt}{}^{13}C_a = {}^{13}F_{ff} + {}^{13}N_{bio} + {}^{13}N_{oce}. \tag{1.3}$$

The content of ^{13}C in each of the fluxes is about $1.1\,\%$ of the total CO_2 fluxes in Equation 1.1, meaning the averaged growth rate of $^{13}CO_2$ is approximately $0.047\,\mathrm{Pg\,C\,yr^{-1}}$. We can write Equation 1.3 as a function of the total CO_2 fluxes and the isotopic fractionation effects:

$$\frac{d}{dt}{}^{13}C_a = F_{ff}R_{ff} - \alpha_{ph}F_{al}R_a + F_{la}R_v - \alpha_{ao}F_{ao}R_a + \alpha_{oa}F_{oa}R_o, \tag{1.4}$$

where N_{bio} is split into an atmosphere-to-land flux (F_{al}) and a land-to-atmosphere flux (F_{la}). For the sake of parsimony, fires, regrowth, and other LUC effects are apportioned to these two fluxes. The N_{oce} is separated into an atmosphere-to-ocean flux (F_{ao}) and an ocean-to-atmosphere flux (F_{oa}). The R values depict the isotopic composition ($^{13}C/(^{13}C+^{12}C)$, approximately 0.011) in the various carbon reservoirs: the atmosphere (R_a), fossil fuels (R_{ff}), land vegetation and soils (R_v), and ocean surface water (R_o). Multiplication of a CO_2 flux with the isotopic ratio R from the originating reservoir determines the $^{13}CO_2$ flux without fractionation effects. The α values are the isotopic fractionation factors, which range from 0.99 to 0.98 [*Tans et al.*, 1993]. The respiration flux $F_{la}R_v$, however, is often assumed to have no fractionation effects associated. Equation 1.4 describes the $^{13}CO_2$ mass balance quite accurately, but it would be better if the influence of net exchange is separated from the gross fluxes, in particular for budgeting studies of the carbon cycle. After some manipulation we obtain:

$$\begin{aligned}
\frac{d}{dt}{}^{13}C_a &= F_{ff}R_{ff} + (F_{al} - F_{la})\,\alpha_{ph}R_a + (F_{ao} - F_{oa})\,\alpha_{ao}R_a \\
&\quad + F_{la}\,(R_v - R_v^{eq}) + F_{oa}\alpha_{ao}\,(R_a^{eq} - R_a).
\end{aligned} \tag{1.5}$$

The ratio $R_a^{eq} = (\alpha_{oa}/\alpha_{ao})R_o$ and depicts the isotopic ratio of CO_2 that is in equilibrium with the ocean surface. The other ratio $R_v^{eq} = \alpha_{ph}R_a$ depicts the ratio in terrestrial vegetation that is in equilibrium with the current atmosphere. As the absolute $^{13}CO_2$ content is not a reported property it is useful to express Equation 1.5 as the rate of change of $\delta^{13}C$, which is explained in the following section.

1.4 Combined CO_2 and $\delta^{13}C$ budget

An expression for the rate of change in atmospheric $\delta^{13}C$ (δ_a) was derived in detail by *Tans et al.* [1993] by manipulating Equation 1.1 and Equation 1.5. First, the rate of change in $^{13}C_a$ can be written as:

$$\frac{d}{dt}{}^{13}C_a = C_a \frac{d}{dt}R_a + R_a \frac{d}{dt}C_a, \tag{1.6}$$

therefore, the rate of change in R_a is written as:

$$C_a \frac{d}{dt}R_a = \frac{d}{dt}{}^{13}C_a - R_a \frac{d}{dt}C_a. \tag{1.7}$$

Substitution of Equation 1.1 and 1.5 in Equation 1.7 gives:

$$
\begin{aligned}
C_a \frac{d}{dt}R_a &= F_{ff}\left(R_{ff} - R_a\right) + \left(F_{al} - F_{la}\right)\left(\alpha_{ph} - 1\right)R_a + F_{la}\left(R_v - R_v^{eq}\right) \\
&+ \left(F_{ao} - F_{oa}\right)\left(\alpha_{ao} - 1\right)R_a + F_{oa}\alpha_{ao}\left(R_a^{eq} - R_a\right).
\end{aligned} \tag{1.8}
$$

By dividing the ratios R in Equation 1.8 with the standard ratio $^{13}C/(^{13}C+^{12}C)$ adopted from the VPDB reference sample and assuming $\epsilon = (\alpha - 1)$ equals the fractionation factor in ‰, we can write:

$$
\begin{aligned}
C_a \frac{d}{dt}\delta_a &= F_{ff}\left(\delta_{ff} - \delta_a\right) + N_{bio}\epsilon_{ph} + F_{la}\left(\delta_v - \delta_v^{eq}\right) \\
&+ N_{oce}\epsilon_{ao} + F_{oa}\left(\delta_a^{eq} - \delta_a\right),
\end{aligned} \tag{1.9}
$$

where $N_{bio} = (F_{al} - F_{la})$ and $N_{oce} = (F_{ao} - F_{oa})$, and the multiplicative factors of R_a/R_{ref} and α_{ao} are set to one as an approximation [*Tans et al.*, 1993].

An advantage of Equation 1.5 and 1.9 is that the net exchange fluxes N_{bio} and N_{oce} are separated from the gross fluxes F_{la} and F_{oa}. For example, the term $N_{bio}\epsilon_{ph}$ represents the net isoflux in $Pg\,C\,‰\,yr^{-1}$ as a result of photosynthetic fractionation and has a positive effect on the rate of change of δ_a. Assuming N_{bio} is $-1.6\,Pg\,C\,yr^{-1}$ and ϵ is $-20\,‰$, it would give a positive isoflux of $32\,Pg\,C\,‰\,yr^{-1}$.

The terms containing F_{la} and F_{oa} are the so-called isodisequilibrium fluxes. These fluxes represent an additional flux of $^{13}CO_2$ molecules even if the net exchange over ocean and land equals zero. As fossil fuel emissions add isotopically depleted CO_2 in the atmosphere ($\delta_{ff} \approx -30\,‰$), the biosphere signature δ_v follows with a time lag dependent on the carbon residence time in plants and soils [*Tans et al.*, 1993]. This is a direct result of the Suess effect mentioned in Section 1.3. Thus, δ_v is less isotopically depleted than δ_v^{eq}, which

is in equilibrium with the current atmosphere. The term $F_{\mathrm{la}}\,(\delta_{\mathrm{v}} - \delta_{\mathrm{v}}^{\mathrm{eq}})$ therefore has an enriching tendency on the δ_{a} rate of change. Similarly, the isotopic signature in ocean water is out of equilibrium with the current signature in the atmosphere, also affecting the δ_{a} rate of change.
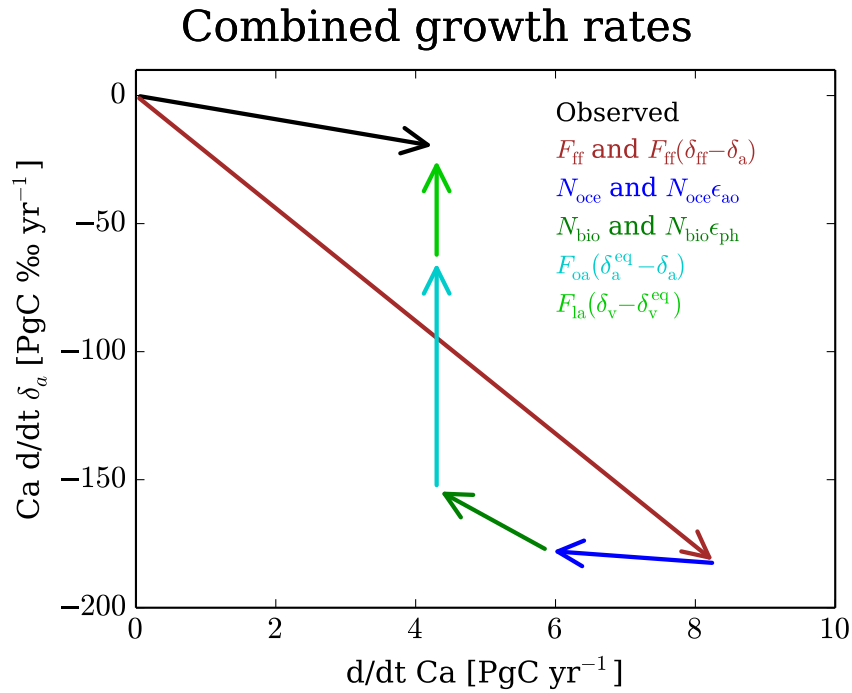
FIGURE 1.3: The annual carbon (along the x-axis) and δ_{a} (along the y-axis) budget using averaged estimates from the recent literature. The colored arrows depict the sources and sinks of Equation 1.1 and Equation 1.9. There is a closed budget if the sum of all colored arrows returns to the black arrowhead (observed rate of change in atmosphere).

The closing of the δ_{a} and CO_2 budgets is best illustrated using an arrow diagram (Figure 1.3). The different sources and sinks affecting the annual growth rates of CO_2 along the x-axis and δ_{a} along the y-axis are displayed as colored arrows. A closed budget for both tracers is accomplished if the sum of all colored arrows returns to the black arrowhead, which represents the observed growth rate of CO_2 and δ_{a}. Using IPCC flux estimates and typical isotopic ratios and fractionation values from the literature [e.g., *Alden et al.*, 2010, *Tans et al.*, 1993] we can close the mean budget. It is clearly visible that F_{ff} has a strong positive impact on the CO_2 budget, but a negative impact on the δ_{a} budget, causing the slow net downward draw of δ_{a} over time. As stated earlier, the impact of land uptake on the δ_{a} budget is approximately 5-10 times greater than that of ocean uptake. Timeseries of the separate flux components are displayed in Figure 2.2 on page 34, and show the relative contributions of each on the CO_2 and δ_{a} budgets.

One of the reasons to study the δ_a budget is to improve the estimates of the two net carbon exchange fluxes (N_{bio} and N_{oce}). This cannot be accomplished by solving only Equation 1.1 as there are two unknowns in one equation. Combining Equation 1.1 and 1.9, together with reasonable estimates for fossil fuel emissions, gross fluxes and isotopic properties, we can estimate consistent N_{bio} and N_{oce} that are in agreement with observed growth rates of CO_2 and δ_a. This so-called 'double deconvolution' method has been used previously in inverse modeling studies [e.g., *Ciais et al.*, 1995, *Fung et al.*, 1997] and will be used in Chapter 2. There is a caveat: it requires realistic estimates of the isodisequilibrium fluxes, which we cannot neglect in the budget of δ_a (arrows are vertical in Figure 1.3). The magnitudes of isodisequilibrium fluxes from land and ocean are highly uncertain as they are strongly dependent on accurate estimates of the gross fluxes F_{la} and F_{oa}, and the correct aggregation of the Suess effect in the ocean and land isotopic signatures. Another uncertainty in the δ_a budget is isotopic fractionation. As opposed to the uniform ocean fractionation parameter ϵ_{ao}, the photosynthetic fractionation parameter ϵ_{ph} is far more heterogeneous due to metabolic pathway differences among plants and variations in the response to environmental conditions.

The carbon flux estimates in Figure 1.3 show that we have an approximate closed budget in both CO_2 and $\delta^{13}C$. Whether the fluxes also have enough leverage to close the interannual variability (IAV) budget is studied in Chapter 2. The main research questions formulated there are:

RQ1: How can we close the IAV budget in δ^{13}C given a closed budget in CO_2 and low IAV in ocean uptake?

RQ2: What are the main drivers responsible for terrestrial isodisequilibrium IAV?

1.5   Terrestrial biosphere modeling

To understand the processes underlying ^{13}C exchange we must focus our attention to the terrestrial biosphere. As explained in Section 1.4, terrestrial isotope exchange explains

the largest natural variations in atmospheric $\delta^{13}C$ in two ways: (1) through fractionation acting on the net photosynthetic uptake of CO_2 and (2) through isotopic disequilibrium. To accurately simulate trace gases like CO_2 or isotope ratios like $\delta^{13}C$, the terrestrial biosphere model must represent a large variety of biogeochemical processes on very short (minutes) to very long (decades) timescales, and on small spatial scales (1 km) to global scales [*Schaefer et al.*, 2008]. Many different models have been developed to estimate CO_2 exchange over land, but only a few include the $^{13}CO_2$ exchange required to simulate atmospheric $\delta^{13}C$. For example, earlier estimates of C_3 and C_4 isotope fractionation were made in terrestrial biosphere models by, e.g., *Lloyd and Farquhar* [1994] and *Fung et al.* [1997]. Isotope fractionation effects were included in the Lund-Potsdam-Jena vegetational model (LPJ) to simulate not only the terrestrial cycle of CO_2 and $^{13}CO_2$ but also the storage of ^{13}C in plants and soils to account for the isotopic disequilibrium flux [e.g., *Kaplan et al.*, 2002]. Subsequently, this model was used to infer net carbon exchange fluxes by closing the atmospheric budget of $\delta^{13}C$ [*Scholze et al.*, 2003] and to study LUC effects on the isodisequilibrium flux [*Scholze et al.*, 2008]. Another system, the SiB (Simple Biosphere) model was originally developed by *Sellers et al.* [1986] to estimate fluxes of carbon, water, energy, and momentum on a vegetated surface. A revised version of SiB was presented ten years later that improved the biophysical mechanisms and enabled the use of satellite derived vegetation data as input [*Sellers et al.*, 1996a,b]. The additional exchange of $^{13}CO_2$ was implemented in SiB version 2.5 by *Suits et al.* [2005] using separate formulations for C_3 and C_4 isotopic fractionation. They studied the response in fractionation to changes in environmental conditions, such as relative humidity and precipitation.

Other models, e.g., the Carnegie-Ames-Stanford Approach (CASA) model, provide less detailed CO_2 exchange estimates but were primarily developed to calculate the long-term changes in carbon stocks at monthly time steps [*Potter et al.*, 1993, *Randerson et al.*, 1996]. This makes CASA and similar models well suited to estimate carbon losses from fire disturbances [e.g., *van der Werf et al.*, 2010]. The models SiB and CASA were combined by *Schaefer et al.* [2008] to create SiBCASA, as neither model was able to simulate all the mechanisms of the terrestrial carbon cycle. SiB alone cannot predict biomass and heterotrophic respiration and CASA alone cannot predict detailed CO_2 exchange at a high temporal resolution. SiBCASA is therefore a more complete biosphere model.

In this thesis, we used SiBCASA as our main terrestrial biosphere model to predict fluxes of CO_2 and $^{13}CO_2$. We developed additional components for fire disturbances (driven by satellite data), the exchange of $^{13}CO_2$, and the storage of ^{13}C in the different carbon pools (e.g., leaves, stems, soil), as explained in more detail in Chapters 2 and 3. Calculation of GPP (mol m^{-2} s^{-1}) and water transpiration (E; mol m^{-2} s^{-1}) is coupled

with stomatal conductance of water vapor (g_s; mol m^{-2} s^{-1}). This common approach provides a GPP that is fully consistent with evaporative demand and CO_2 gradients from atmosphere to leaf interior.

To derive $^{13}CO_2$ fluxes we must also account for isotopic fractionation, or discrimination. It is expressed as $\alpha_{ph} = R_v^{eq}/R_a$, and is usually not smaller than 0.98. Parameter α_{ph} was previously described in the absolute ^{13}C mass balance Equation 1.4. Discrimination is also often expressed in ‰, either as

$$\Delta = \left(1 - \frac{R_v^{eq}}{R_a}\right) \cdot 1000 = (1 - \alpha_{ph}) \cdot 1000, \tag{1.10}$$

in biosphere modeling, or as:

$$\epsilon_{ph} = (\alpha_{ph} - 1) \cdot 1000 = -\Delta, \tag{1.11}$$

in inverse budgeting studies such as in Equation 1.9. Thus if α_{ph} is 0.98, then Δ is 20‰ and ϵ_{ph} -20‰.

There are two major processes during photosynthesis where there is discrimination against the heavier ^{13}C isotope. Plants fractionate with 4.4‰ (Δ_s) when CO_2 diffuses from the atmosphere through the stomata, and fractionate with 28‰ (Δ_f) when CO_2 reacts with the enzyme Ribulose-1,5-bisphosphate (Rubisco). The CO_2 gradient-weighted fractionation formula for C_3 plants is [*Farquhar et al.*, 1989]:

$$\Delta_{C3} = \Delta_s \frac{c_a - c_i}{c_a} + \Delta_f \frac{c_i}{c_a} = \Delta_s + (\Delta_f - \Delta_s)\frac{c_i}{c_a}, \tag{1.12}$$

where c_a and c_i represent CO_2 partial pressures in the atmosphere and leaf interior. This is a simplified formulation that omits several other (but minor) fractionation effects (see also Chapters 2 and 3). We can approximate the signature of newly assimilated carbon, δ_v^{eq}, by subtracting Δ_{C3} from the atmospheric signature δ_a:

$$\delta_v^{eq} \approx \delta_a - \Delta_{C3}. \tag{1.13}$$

That would give δ_v^{eq} a value of -28‰, assuming $\delta_a = -8$‰ and $\Delta_{C3} = 20$‰. It should be noted that the stomatal conductance g_s affects Δ_{C3} through changes in the CO_2 gradient. An increase in relative humidity (RH) enhances stomatal conductance and the ratio of c_i/c_a if carbon uptake remains unchanged. This adds more weight to the Rubisco fractionation and therefore Δ_{C3} increases. When the air is dry the opposite happens; a decrease in RH reduces the ratio of c_i/c_a and ultimately reduces Δ_{C3}. The sensitivity of Δ_{C3} and thus δ_v^{eq} to changes in RH is mainly determined by g_s. Improvements in

modeled δ_v^{eq} were realized by modifying the g_s formulation [*Ballantyne et al.*, 2010]. The sensitivity of Δ_{C3} to stomatal conductance is studied in detail in Chapter 3.
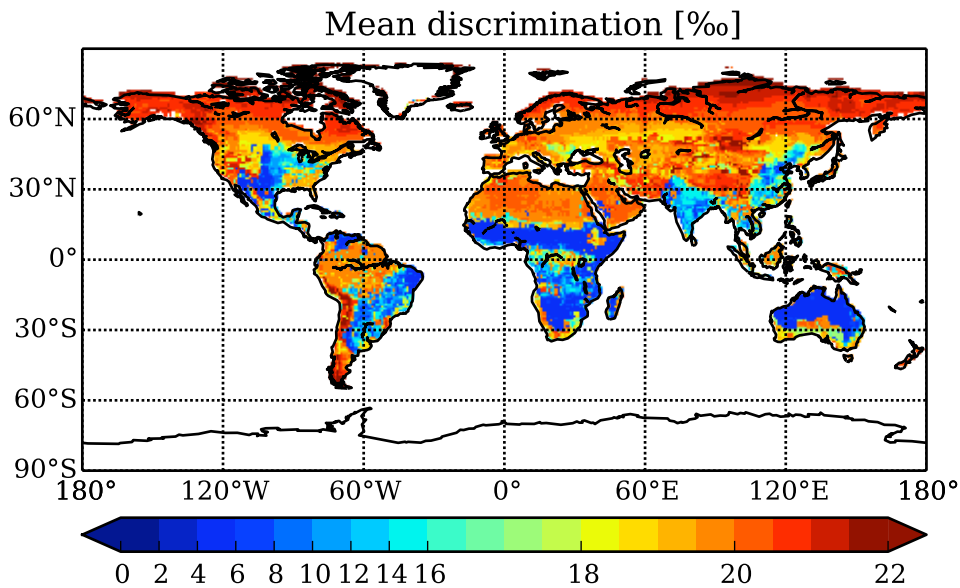
FIGURE 1.4: SiBCASA's annual plant discrimination. Differences in C_3 and C_4 metabolic pathways provide a clear spatial contrast in the annual mean discrimination. Smaller variations in discrimination are largely driven by RH, precipitation, and soil moisture conditions. This figure is discussed in more detail in Chapter 3. Note that the color scale is nonlinear.

C_4 plants are able to fix almost all $^{13}CO_2$ through the enzyme Phosphoenolpyruvate carboxylase (PEPC), and therefore the only fractionation effects are those involved in transport, hence, $\Delta_{C4} \approx 4.4\,\permil$ [*Suits et al.*, 2005]. The discrimination against ^{13}C is therefore approximately 5 times smaller for C_4 plants than for C_3 plants.

In SiBCASA, the differences in metabolic pathways result in distinct spatial differences in global plant discrimination (Figure 1.4). The C_4 dominant areas have a much lower discrimination value as seen in the South American grasslands, the African subtropical savannas, in Northern Australia, and in North American crop production areas. Within C_3 dominated areas there are smaller differences in discrimination caused by climatic conditions, water availability, and RH.

The transfer of carbon and the $^{13}C/^{12}C$ ratio is further modeled for a series of biogeochemical pools. Given realistic turnover rates, the isotopic signal carries through the different carbon pools, which ultimately respires back to the atmosphere (and causes the terrestrial isodisequilibrium flux). There is evidence that numerous additional fractionation effects exist that can alter the isotopic ratio in these successive steps, but their responses to changing environmental conditions are often complex to model and are not

yet fully understood [*Brüggemann et al.*, 2011]. Therefore, no additional fractionation is included in the SiBCASA model.

A more complete analysis on the framework of ^{13}C exchange in SiBCASA is provided in Chapter 3. We also include an analysis of the new biomass burning flux estimates of CO_2 and $^{13}CO_2$. The main research question in Chapter 3 is:

RQ3: Does modeled discrimination in photosynthesis respond sufficiently to changes in environmental conditions?

1.6   Inverse modeling

The final method to improve our understanding of the carbon cycle is data-assimilation. Data-assimilation is an inverse modeling approach that integrates information from atmospheric observations, mechanistic models, and emission statistics into a consistent analysis of the carbon cycle. We use data-assimilation to refine global-scale predictions of atmospheric carbon uptake and release, and minimize differences between modeled and observed patterns of CO_2 and δ^{13}C in the atmosphere. Uncertainties in these fluxes are currently still large, because: (1) it is difficult to accurately separate the ocean carbon sink from the land carbon sink, and (2) the net carbon exchange flux N_{bio} remains uncertain as the gross GPP and TER fluxes are poorly understood. Extreme drought is known to have a large impact on this exchange as it can reverse a regional net carbon sink into a net carbon source. To better constrain such extreme environmental changes we use a large collection of atmospheric δ^{13}C observations alongside CO_2 in the inversion method. The measurable changes in δ^{13}C in the atmosphere may relate to a reduction of the net carbon sink, or to a reduction in the discrimination against ^{13}C during CO_2 uptake (see Section 1.5), or to a combination of both processes.

The use of atmospheric observations to study the global carbon cycle has been ongoing for many years [e.g., *Ciais et al.*, 1995, *Francey et al.*, 1995, *Peters et al.*, 2007, *Tans et al.*, 1990]. In earlier inverse modeling studies, CO_2 fluxes were solved over a multi-year period and only for a limited number of large regions [e.g., *Gurney et al.*, 2002, *Rayner*

and Law, 1999]. For most of these studies the CO_2 observational constraint was provided by GlobalView; a gap-filled data product derived from real measurements [*Masarie and Tans*, 1995]. Although they were successful at deriving continental-scale fluxes, they lacked the detail required to explain regional changes in the carbon cycle [*Rayner and Law*, 1999]. Other studies solved fluxes on a grid-scale level [e.g., *Rödenbeck et al.*, 2003] by using a covariance structure as an additional constraint to handle the greatly increased number of unknowns. These methods were computationally expensive due to the need to invert large matrices in a single operation, and to establish linear relationships between the unknown CO_2 fluxes and CO_2 concentrations. To overcome these hurdles *Peters et al.* [2005] developed a data-assimilation system that is based on a time-stepping algorithm used in numerical weather prediction (NWP) models. It employs an ensemble Kalman filter approach that solves a Bayesian system in smaller subsets of unknown fluxes (of 5 week periods), and thus greatly reduces the size of matrices involved. Moreover, it allows us to solve for fluxes in a nonlinear model and can easily be modified for other trace gases, such as $\delta^{13}C$. The same system was later branded "CarbonTracker" and was used to estimate regional patterns of net exchange for North America [*Peters et al.*, 2007] and Europe [*Peters et al.*, 2010].

In this thesis we modified CarbonTracker to assimilate atmospheric observations of $\delta^{13}C$ alongside CO_2, in order to better constrain the carbon cycle. Instead of solving for net CO_2 fluxes alone, our modifications enable a solution for net $^{13}CO_2$ fluxes to determine the optimal rate of change of CO_2 and $\delta^{13}C$, simultaneously. The mass balance equations shown before (Equation 1.1 and Equation 1.5) take the following form in CarbonTracker:

$$\frac{\mathrm{d}}{\mathrm{dt}}C_\mathrm{a} = F_\mathrm{ff} + F_\mathrm{fire} + \lambda_\mathrm{bio}N_\mathrm{bio} + \lambda_\mathrm{oce}N_\mathrm{oce}, \tag{1.14}$$

$$\begin{aligned}\frac{\mathrm{d}}{\mathrm{dt}}{}^{13}C_\mathrm{a} = {}& F_\mathrm{ff}R_\mathrm{ff} + F_\mathrm{fire}\alpha_\mathrm{ph}R_\mathrm{a} + \lambda_\mathrm{bio}N_\mathrm{bio}\alpha_\mathrm{ph}R_\mathrm{a} + \lambda_\mathrm{oce}N_\mathrm{oce}\alpha_\mathrm{ao}R_\mathrm{a} \\ & + F_\mathrm{la}\left(R_\mathrm{v} - R_\mathrm{v}^\mathrm{eq}\right) + F_\mathrm{oa}\alpha_\mathrm{ao}\left(R_\mathrm{a}^\mathrm{eq} - R_a\right),\end{aligned} \tag{1.15}$$

where λ_bio and λ_oce are land and ocean scaling factors derived in the assimilation step to refine the net exchange fluxes. Fires are separated from net land exchange and remain unscaled in CarbonTracker, as are fossil fuel emissions and isodisequilibrium fluxes. From the modeled C_a and $^{13}C_\mathrm{a}$ content we derive the corresponding $\delta^{13}C$ signatures using Equation 1.2.

Atmospheric transport provides the link between exchange fluxes of CO_2 at the Earth's surface and observations of CO_2 and $\delta^{13}C$ in the atmosphere. Winds caused by differences in air pressure transport CO_2 around the world and as a result, local events like
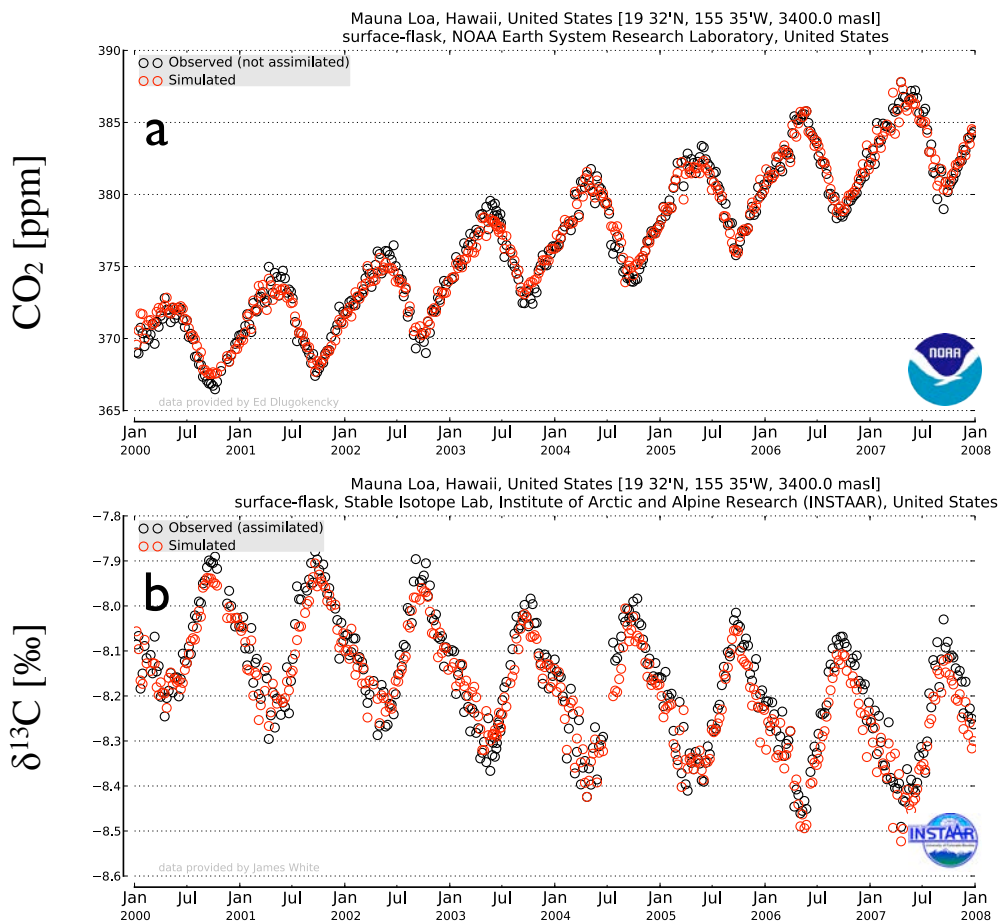
FIGURE 1.5: Simulated levels (red circles) of CO_2 in panel (a) and $\delta^{13}C$ in panel (b) in comparison to flask observations (black circles) at the Mauna Loa Observatory, Hawaii, United States. Measurements of CO_2 and $\delta^{13}C$ were provided by NOAA/ESRL and INSTAAR lab, respectively.

forest fires, vegetation growth, and ocean carbon exchange influence CO_2 and $\delta^{13}C$ levels at larger scales. Within CarbonTracker we use Transport Model 5 (TM5) to account for atmospheric transport [*Krol et al.*, 2005]. The meteorological fields such as winds, temperature, and pressure are updated every 3 hours and come from a NWP model developed by the European Centre for Medium-Range Weather Forecasts (ECMWF). CarbonTracker's ability to reproduce the observational record of atmospheric CO_2 and $\delta^{13}C$ is displayed in Figure 1.5 as an example. Modeled CO_2 and $\delta^{13}C$ represent the data very well at Mauna Loa observatory due to the spatial and temporal scaling of N_{bio} and N_{oce}.

CarbonTracker is fed by initial first guess estimates and uncertainties (the prior) of the surface CO_2 and $^{13}CO_2$ fluxes to be refined in the assimilation process. The terrestrial first guess estimate for net exchange comes from SiBCASA as outlined in Section 1.5.

For all other fluxes and isotopic properties we use estimates from process based models and inventories discussed in detail in Chapter 4.

CarbonTracker also permits nonlinear calculations, which allow us to solve for isotope discrimination parameter ϵ_{ph} alongside N_{bio}, and predict the regional variations in atmospheric $\delta^{13}C$ to specific plant physiological processes integrated over a larger region. Capturing large-scale drought dynamics in the fluxes and isotopic discrimination could potentially inform us about drought stress in plants that changes stomatal conductance. This is also studied in detail in Chapter 4 with the following research question:

RQ4: Are regional droughts detectable by assimilating both CO_2 and $\delta^{13}C$ in an atmospheric inversion?

Chapter 2

Global simulations of interannual variability in terrestrial $^{13}\text{C}/^{12}\text{C}$ exchange

Abstract

Previous studies suggest that a large part of the variability in the atmospheric ratio of $^{13}\text{CO}_2/^{12}\text{CO}_2$ (δ_{a}) originates from carbon exchange with the terrestrial biosphere rather than with the oceans. Since this variability is used to quantitatively partition the total carbon sink, we investigated the contribution of interannual variability (IAV) in biospheric exchange to the observed atmospheric δ_{a} variations.

We used the SiBCASA biogeochemical model, including a detailed isotopic fractionation scheme, separate ^{12}C and ^{13}C biogeochemical pools, and satellite-observed fire disturbances. This model of $^{13}\text{CO}_2$ and $^{12}\text{CO}_2$ exchange thus produced return fluxes from its differently aged pools, contributing to the so-called isodisequilibrium flux. Our simulated terrestrial ^{13}C budget closely resembled previously published model results for plant discrimination and disequilibrium fluxes, and similarly suggests that variations in C_3 discrimination and year-to-year variations in C_3 and C_4 productivity were the main drivers of their IAV. The year-to-year variability in the isotopic disequilibrium flux was

much lower ($\pm$ 1.5 Pg C ‰ yr^{-1}; 1σ) than required ($\pm$ 12.5 Pg C ‰ yr^{-1}) to match atmospheric observations, however, under the common assumption of low variability in net ocean CO_2 fluxes and constant discrimination. This contrasts with earlier published results.

It is currently unclear how to increase IAV in these drivers suggesting that SiBCASA still misses processes that can enhance variability in plant discrimination and changes in C_3/C_4 productivity. Alternatively, ^{13}C budget terms other than terrestrial disequilibrium fluxes, including possibly the atmospheric growth rate, must have significantly different IAV in order to close the atmospheric ^{13}C budget on a year-to-year basis.

2.1   Introduction

Measured atmospheric CO_2 and its ^{13}C/^{12}C ratio (expressed as δ^{13}C in ‰) are complementary and have been combined to estimate net oceanic and terrestrial exchange at the Earth's surface [e.g., *Ciais et al.*, 1995, *Francey et al.*, 1995, *Fung et al.*, 1997, *Joos and Bruno*, 1998, *Rayner et al.*, 2008, *Tans et al.*, 1993]. The ratio of the ^{13}C and ^{12}C stable isotopes provide an additional constraint on the net global carbon uptake from the atmosphere by either the terrestrial biosphere or by the ocean, given that each flux discriminates slightly differently against the heavier ^{13}C isotope of CO_2. This process is called 'isotopic fractionation' or discrimination, and gives terrestrial and oceanic carbon exchange its own isotopic signature and its own distinct influence on the atmospheric δ^{13}C ratio.

The use of atmospheric δ^{13}C to partition the ocean and land uptake requires detailed knowledge of other processes in the ^{13}C budget. For instance, special attention must be given to the isotopic disequilibrium flux [*Tans*, 1980, *Tans et al.*, 1993], which stems from differences in isotopic composition between 'old' carbon released from oceanic and terrestrial reservoirs and the current atmosphere. The continuing depletion of atmospheric δ^{13}C by the addition of ^{13}C depleted fuel-derived CO_2 (also known as the Suess effect; *Suess* [1955]) gives the 'old' carbon that is released from the reservoirs an isotopic signature that is heavier and out of equilibrium with the current atmospheric signature. In addition to this low frequency component of disequilibrium flux, year-to-year changes in fractionation resulting from either C_3-only and/or C_3:C_4 productivity changes can induce interannual variability (IAV) in disequilibrium flux [e.g., *Scholze et al.*, 2008].

Close attention must also be paid to seasonal and spatial variations of C_3 and C_4 plant isotopic fractionation. Variations in C_3 fractionation are controlled by stomatal opening and closing, which are typically modeled as being driven by leaf-atmosphere water vapor gradients. Fractionation during photosynthesis can be accounted for by simulating the

leaf interior CO_2 as a function of assimilation and stomatal conductance, as in the studies of *Fung et al.* [1997], *Lloyd and Farquhar* [1994]. In recent studies more detailed process descriptions have been used to estimate plant fractionation [e.g., *Kaplan et al.*, 2002, *Scholze et al.*, 2003, *Suits et al.*, 2005]. Some of them included a complete terrestrial cycling framework of CO_2 and $^{13}CO_2$ that included year-to-year changes in both isotopic fractionation and disequilibrium fluxes. *Scholze et al.* [2003] found that IAV in ^{13}C exchange was controlled by fractionation changes caused by climate variability and gross primary production (GPP) shifts between areas dominated by C_3 or C_4 vegetation. Fires and land use change contributed only on the longer time scales, which are relevant for the disequilibrium fluxes [*Scholze et al.*, 2008]. If these were ignored the partitioning of net carbon fluxes derived from atmospheric CO_2 and δ^{13}C in a traditional 'double deconvolution' [e.g., *Ciais et al.*, 1995] method would change by $1\,\mathrm{Pg\,C\,yr^{-1}}$.

When isotopic fractionation and low frequency disequilibrium fluxes (and fossil fuel emissions) are properly accounted for, double deconvolution can be a method for separating the average net ocean and net land uptake fluxes over longer time scales. In contrast, the year-to-year variability on these estimated net fluxes is more problematic: when only net biosphere and net ocean fluxes are estimated in a double deconvolution the resultant IAV on ocean fluxes is much larger than bottom-up ocean models support [*Le Quere et al.*, 2003, *Winguth et al.*, 1994]. This unrealistically large ocean variability anti-correlates with the estimated IAV in terrestrial fluxes from this method, which are needed to match the observed variability in δ^{13}C. *Alden et al.* [2010] addressed this unrealistic outcome of the IAV in traditional double deconvolution estimates, and suggested that under the common assumption of low IAV of ocean exchange, the terrestrial disequilibrium flux could instead be given large IAV to match the year-to-year changes in the atmospheric δ^{13}C. Thus, the ocean and terrestrial biosphere net flux variability would be identical to our best estimates from CO_2-only based estimates, and process model simulations. This explanation of atmospheric δ^{13}C variability from *Alden et al.* [2010], along with the traditional one from *Ciais et al.* [1995], is visually illustrated in Figure 2.1b, and further explained in Section 2.3.1. In addition, *Randerson et al.* [2002] suggested that if IAV in terrestrial C_3 fractionation covaries with IAV in GPP (e.g., poor growth conditions along with reduced fractionation), smaller year-to-year changes in net ocean and land fluxes are needed to explain the atmospheric δ^{13}C variability.

In this study we examined the extent to which previous findings by *Alden et al.* [2010], *Randerson et al.* [2002], and *Scholze et al.* [2003] are supported by a new bottom-up terrestrial biosphere model. Like the model of *Scholze et al.* [2003], our model incorporated a detailed description of the exchange of ^{12}C and ^{13}C with the atmosphere from hourly to decadal time scales. We specifically focused our analysis on the IAV of the ^{13}C fluxes produced by our model, and what they imply for the variability of net terrestrial CO_2

fluxes if we try to close the ^{13}C/^{12}C budgets in a double deconvolution approach. This necessitated a detailed examination of the IAV of the terrestrial disequilibrium flux due to its key role in this estimation and supposed large variability [*Alden et al.*, 2010]. (1) Can the terrestrial biosphere cause large variability in ^{13}C exchange? (2) Can the covariation between GPP and terrestrial isotopic fractionation contribute to atmospheric δ^{13}C variability as suggested by *Randerson et al.* [2002]? And if not, (3) then what process should be reconsidered to close the ^{13}C budget from the point of view of IAV?

2.2   Methodology

2.2.1   SiBCASA model

Previous efforts led to the development of the SiBCASA model, which combines photosynthesis and biophysical processes from the SiB (Simple Biosphere) model version 3 with carbon biogeochemical processes from the Carnegie-Ames-Stanford Approach model [*Schaefer et al.*, 2008]. Meteorological driver data is provided by the European Centre for Medium-Range Weather Forecasting (ECMWF) from 2000 up to 2008. SiBCASA calculates the surface energy, water, and CO_2 fluxes at 10 minute time steps on a spatial resolution of 1 × 1 degrees, and predicts the moisture content and temperature of the canopy and soil [*Sellers et al.*, 1996a]. In an iterative process, the uptake of carbon is calculated by the Ball-Berry stomatal conductance model [*Collatz et al.*, 1991] in combination with a C_3 enzyme kinetic model [*Farquhar et al.*, 1980] and a C_4 photosynthesis model [*Collatz et al.*, 1992]. This coupled framework can therefore be used to determine the CO_2 concentration ratio between the leaf chloroplast and atmosphere.

These ratios are further used in a modified version of the fractionation scheme [*Farquhar*, 1983, *Lloyd and Farquhar*, 1994, and *Suits et al.*, 2005] to calculate at each time step a gradient-weighted C_3 plant fractionation factor Δ:

$$
\begin{aligned}
\Delta_{C3} \;=\; & \Delta_{\mathrm{b}}\left(\tfrac{c_{\mathrm{a}}-c_{\mathrm{s}}}{c_{\mathrm{a}}}\right) + \Delta_{\mathrm{s}}\left(\tfrac{c_{\mathrm{s}}-c_{\mathrm{i}}}{c_{\mathrm{a}}}\right) \\
& + (\Delta_{\mathrm{diss}} + \Delta_{\mathrm{aq}})\left(\tfrac{c_{\mathrm{i}}-c_{\mathrm{c}}}{c_{\mathrm{a}}}\right) + \Delta_{\mathrm{f}}\left(\tfrac{c_{\mathrm{c}}}{c_{\mathrm{a}}}\right),
\end{aligned}
\tag{2.1}
$$

where the c's represent the partial pressures of CO_2 at canopy air space (c_{a}), leaf boundary layer (c_{s}), leaf stomata (c_{i}), and chloroplast (c_{c}). The isotopic fractionation effects (Δ) represent the relative reduction of ^{13}C to ^{12}C at different uptake stages from canopy air space to leaf chloroplasts. These stages are: CO_2 diffusion from c_{a} to c_{s} ($\Delta_{\mathrm{b}} = 2.9\,‰$) and CO_2 diffusion to c_{i} ($\Delta_{\mathrm{s}} = 4.4\,‰$), dissolution of CO_2 in mesophyll and transport to

the chloroplast ($\Delta_{\mathrm{diss}} = 1.1$ and $\Delta_{\mathrm{aq}} = 0.7\,\text{‰}$, respectively). The largest isotope effect, however (i.e., that causing the strongest reduction of ^{13}C relative to ^{12}C), is associated with fixation of CO_2 by the enzyme Rubisco in the chloroplast ($\Delta_{\mathrm{f}} = 28.2\,\text{‰}$). C_4 plant discrimination is held constant at $\Delta_{\mathrm{C4}} = \Delta_{\mathrm{s}} = 4.4\,\text{‰}$ and no discrimination is assigned to the respiration fluxes. The time invariant C_3/C_4 plant distribution map is determined from ecosystem modeling, satellite data, and agricultural maps [*Still et al.*, 2003].

In the CASA part of the model [*Randerson et al.*, 1996], we implemented 13 biogeochemical pools for total carbon (^{12}C+^{13}C) and also for ^{13}C (separately). The assimilated carbon and ^{13}C are added to two separate storage pools and become available for plant growth. In subsequent stages the carbon is propagated to their own separate live carbon pools, surface litter pools, and layered soil pools. For each pool, the carbon stocks are solved as a first order linear differential equation depending on gains from other pools, losses to other pools and respiration losses due to (heterotrophic) microbial decay and (autotrophic) plant growth [*Schaefer et al.*, 2008]. SiBCASA now has a semi-prognostic canopy, which means that the leaf pool is prognostic but the photosynthesis calculations are constrained by remotely sensed absorbed fraction of Photosynthetically Active Radiation (fPAR). No discrimination effects were considered for transfers of carbon between pools. The average turnover times, as well as the scaling factors for temperature, freezing, and moisture were taken from the original CASA scheme.

Our implementation of fire emissions (CO_2 and $^{13}CO_2$) followed the methodology of *van der Werf et al.* [2003, 2010]. The estimated fire emissions are driven by multiple remotely-sensed burned area products combined in the Global Fire Emissions Database (GFED) version 3.1 [*Giglio et al.*, 2010]. Only above ground, fine litter pools, and coarse woody debris at the surface were considered as sources of combustion. Peat burning [*Page et al.*, 2002] and organic soil carbon combustion were not yet taken into account. The global averaged biomass burning flux for the period 1991-2007 amounts to $1.82 \pm 0.17\,\mathrm{Pg\,C\,yr^{-1}}$, which is similar to the value of $2.0\,\mathrm{Pg\,C\,yr^{-1}}$ published by *van der Werf et al.* [2010]. A more detailed analysis of biomass burning and the pool configuration is given in Chapter 3.

2.2.2 Mass balance of atmospheric CO_2 and $^{13}CO_2$

Atmospheric CO_2 and $^{13}CO_2$ mole fractions reflect the sum of several flux terms at the Earth's surface and they can be expressed by two mass balance equations:

$$\frac{\mathrm{d}}{\mathrm{dt}}C_{\mathrm{a}} \quad = \quad F_{\mathrm{ff}} + F_{\mathrm{fire}} + N_{\mathrm{bio}} + N_{\mathrm{oce}}, \tag{2.2}$$

$$\frac{\mathrm{d}}{\mathrm{dt}}{}^{13}C_{\mathrm{a}} \quad = \quad {}^{13}F_{\mathrm{ff}} + {}^{13}F_{\mathrm{fire}} + {}^{13}N_{\mathrm{bio}} + {}^{13}N_{\mathrm{oce}}, \tag{2.3}$$

where C_a represents the amount of carbon in atmospheric CO_2, N_{bio} and N_{oce} represent net CO_2 exchange fluxes in the terrestrial biosphere and oceans, respectively. F_{ff} represents CO_2 emissions due to fossil fuel combustion and cement production, and F_{fire} represents CO_2 emissions due to biomass burning. The $^{13}CO_2$ counterparts are labeled with superscript 13. Equations 2.2 and 2.3 can be manipulated following *Tans et al.* [1993] to give a budget equation expressed as the rate of change of atmospheric $\delta^{13}C$ (henceforth δ_{a}):

$$
\begin{aligned}
C_{\mathrm{a}}\frac{\mathrm{d}}{\mathrm{dt}}\delta_{\mathrm{a}} \quad = \quad & F_{\mathrm{ff}}\left(\delta_{\mathrm{ff}} - \delta_{\mathrm{a}}\right) \quad + \quad F_{\mathrm{fire}}\epsilon_{\mathrm{ph}} && \text{[emission forcing terms]} \\
& + \quad N_{\mathrm{bio}}\epsilon_{\mathrm{ph}} \quad + \quad N_{\mathrm{oce}}\epsilon_{\mathrm{ao}} && \text{[net exchange forcing terms]} \\
& + \quad F_{\mathrm{la}}\left(\delta_{\mathrm{v}} - \delta_{\mathrm{v}}^{\mathrm{eq}}\right) \quad + \quad F_{\mathrm{fire}}\left(\delta_{\mathrm{fire}} - \delta_{\mathrm{v}}^{\mathrm{eq}}\right) && \text{[terrestrial disequilibrium forcing terms]} \\
& + \quad F_{\mathrm{oa}}\left(\delta_{\mathrm{a}}^{\mathrm{eq}} - \delta_{\mathrm{a}}\right) && \text{[ocean disequilibrium forcing term].}
\end{aligned}
\tag{2.4}
$$

The subscripts oa and la refer the direction of the one-way gross fluxes, i.e., F_{la} refers to the autotrophic and heterotrophic respiration fluxes from land-to-atmosphere and F_{oa} refers to ocean-to-atmosphere outgassing. The isotopic signatures (δ_{xx}) are expressed in ‰ deviation relative to the VPDB standard. These signatures refer to the ^{13}C composition in different reservoirs: fossil fuels (δ_{ff}), biomass affected by burning (δ_{fire}), vegetation and soils (δ_{v}), vegetation that is in equilibrium with the current atmosphere ($\delta_{\mathrm{v}}^{\mathrm{eq}}$), and the atmosphere that is in equilibrium with the ocean surface ($\delta_{\mathrm{a}}^{\mathrm{eq}}$). Negative δ values indicate that the $^{13}C/^{12}C$ ratio of a given sample is smaller than the VPDB standard.

The fractionation effects in Equation 2.4 are represented by ϵ_{ph} for photosynthesis and ϵ_{ao} for ocean exchange. ϵ_{ph} is estimated by $-\Delta$ from SiBCASA (see Section 1.5). Given

the atmospheric δ_{a} signature and the estimated Δ, we can also compute $\delta_{\mathrm{v}}^{\mathrm{eq}}$ using Equation 1.13. The signatures of δ_{v} and δ_{fire} are calculated by taking the ratio of SiBCASA's $^{13}CO_2$ and $^{12}CO_2$ fluxes of F_{la} and F_{fire}, respectively. Their isotopic signals carried over time through the carbon pools have a signature that is generally more enriched in ^{13}C than in current $\delta_{\mathrm{v}}^{\mathrm{eq}}$.

The biomass burning emission term is split up into two separate terms: $F_{\mathrm{fire}}\epsilon_{\mathrm{ph}}$ and $F_{\mathrm{fire}}\left(\delta_{\mathrm{fire}} - \delta_{\mathrm{v}}^{\mathrm{eq}}\right)$. The latter term quantifies the influence of biomass burning on the disequilibrium flux, whereas the former term includes biomass burning as part of the terrestrial net flux, which scales with terrestrial fractionation. The main advantage of writing the isotopic ratio of the fire flux in this way is that it allows for calculating δ_{fire} directly from the $^{13}C/^{12}C$ ratio in F_{fire}, rather than using an approximation derived from δ_{v}.

The mean terrestrial disequilibrium flux is the consequence of a long-term draw down of the atmospheric $^{13}C/^{12}C$ ratio due to fossil fuel emissions of isotopically light CO_2. That makes the older carbon that is released to the atmosphere richer in ^{13}C (δ_{v} and δ_{fire}) compared to the carbon that is currently taken up by the sinks ($\delta_{\mathrm{v}}^{\mathrm{eq}}$). For the terrestrial biosphere, this isotopic difference is designated as the isodisequilibrium forcing coefficient [*Alden et al.*, 2010], and is separately defined for biological respiration $I_{\mathrm{la}} = \delta_{\mathrm{v}} - \delta_{\mathrm{v}}^{\mathrm{eq}}$ and for biomass burning $I_{\mathrm{fire}} = \delta_{\mathrm{fire}} - \delta_{\mathrm{v}}^{\mathrm{eq}}$. It exterts a strong degree of control over the budget equation because the isodisequilibrium coefficient scales with large gross fluxes. The total isotopic disequilibrium flux from the terrestrial biosphere D_{bio} is:

$$
\begin{aligned}
D_{\mathrm{bio}} &= F_{\mathrm{la}}\left[\delta_{\mathrm{v}} - \delta_{\mathrm{v}}^{\mathrm{eq}}\right] + F_{\mathrm{fire}}\left[\delta_{\mathrm{fire}} - \delta_{\mathrm{v}}^{\mathrm{eq}}\right] \\
&= F_{\mathrm{la}}I_{\mathrm{la}} + F_{\mathrm{fire}}I_{\mathrm{fire}}.
\end{aligned} \tag{2.5}
$$

The global area-weighted averaged D_{bio} in units of $\mathrm{Pg\,C\,\text{‰}\,yr^{-1}}$ is calculated using SiB-CASA output variables:

$$
\begin{aligned}
D_{\mathrm{bio}} &= \left[\sum_{\mathrm{x}=1}^{n} F_{\mathrm{la}}[x] \cdot (\delta_{\mathrm{v}}[x] - \delta_{\mathrm{v}}^{\mathrm{eq}}[x]) \cdot GA[x]\right. \\
&\quad \left. + \sum_{\mathrm{x}=1}^{n} F_{\mathrm{fire}}[x] \cdot (\delta_{\mathrm{fire}}[x] - \delta_{\mathrm{v}}^{\mathrm{eq}}[x]) \cdot GA[x]\right] \times UC,
\end{aligned} \tag{2.6}
$$

where the fluxes $F_{\mathrm{la}}[x]$ and $F_{\mathrm{fire}}[x]$ for each grid cell x are given in $\mathrm{\mu mol\,m^{-2}\,s^{-1}}$, where n represents the total number of land grid cells, $GA[x]$ is the grid area in $\mathrm{m^2}$ for each grid cell x, and UC is a unit conversion factor to convert from $\mathrm{\mu mol\,\text{‰}\,s^{-1}}$ to $\mathrm{Pg\,C\,\text{‰}\,yr^{-1}}$.

Besides D_{bio} and ϵ_{ph} from SiBCASA, the other sources of annual fluxes and isotopic signatures in Equation 2.4 are: (1) F_{ff} and δ_{ff}, compiled from the Carbon Dioxide Information and Analysis Center [*Boden et al.*, 2009] and British Petrol Statistical Review of World Energy June (2009), (2) F_{fire}, estimated by SiBCASA, (3) N_{oce}, estimated by *Le Quere et al.* [2007], (4) ocean fractionation ϵ_{ao}, kept constant at $-2\,‰$ [*Zhang et al.*, 1995], (5) N_{bio}, the leftover residual from Equation 2.2, and (6) ocean disequilibrium flux D_{oce}, from *Alden et al.* [2010].

The global quantities of CO_2 and δ^{13}C were derived from a large collection of sampling sites in the Cooperative Air Sampling Network of the National Oceanic and Atmospheric Administration/Earth System Research Laboratory (NOAA/ESRL). The isotopic analysis of each sample was performed at the University of Colorado Institute of Arctic and Alpine Research/Stable Isotope Lab (INSTAAR/SIL).

Equation 2.4 allows us to distinguish the changes in the atmospheric isotopic ratios brought by (1) the discrimination processes during the net CO_2 exchange in the terrestrial biosphere and oceans, and (2) by isotopic disparity between the release and uptake of CO_2 at Earth's surface. As explained in the Section 2.1, we are particularly interested if the *simulated* interannual variability (IAV) on the right-hand side of the equation can balance the *measured* variability on the left-hand side. Incorrect IAV in disequilibrium flux, combined with that observed in the atmosphere, can lead to errors in projected variability in net land, and therefore by residual, in net ocean fluxes.

2.2.3   Reynolds decomposition on D_{bio}

Our first question (which processes contribute most to variability in terrestrial biosphere?) requires a way to separate the yearly fluctuations from the trend, for each process that contributes to D_{bio} in Equation 2.5, i.e., F_{la}, I_{la} or I_{fire}. One technique to achieve this separation is Reynolds decomposition, where for a certain quantity x, the fluctuating part is separated from the mean: i.e., $x = x' + \overline{x}$ [*Reynolds*, 1895]. Applying a Reynolds decomposition on Equation 2.5 gives us 8 terms in total:

$$
\begin{aligned}
\overline{D}_{\text{bio}} + D'_{\text{bio}} \;=\; & \overline{F}_{\text{la}}\overline{I}_{\text{la}} + \overline{F}_{\text{la}}I'_{\text{la}} + F'_{\text{la}}\overline{I}_{\text{la}} + F'_{\text{la}}I'_{\text{la}} \\
& + \;\overline{F}_{\text{fire}}\overline{I}_{\text{fire}} + \overline{F}_{\text{fire}}I'_{\text{fire}} + F'_{\text{fire}}\overline{I}_{\text{fire}} + F'_{\text{fire}}I'_{\text{fire}},
\end{aligned}
\tag{2.7}
$$

To allow D'_{bio} to represent the year-to-year changes on short time-scales rather than decadal changes in the mean, we let $\overline{D}_{\text{bio}}$ include a linear trend over a time period (for

TABLE 2.1: Description of the four different simulations.

name simulation	variable Δ_{C3}	variable δ_a	fire	run time
ISOVAR	✓	✓	✓	1851-2008
ISOFIX	fixed at 19.2 ‰	✓	✓	1851-2008
ISOFIX-FA (Fixed Atmosphere)	fixed at 19.2 ‰	fixed δ_a	✓	ISOFIX restart from 1975
ISOVAR-NF (No Fires)	✓	✓	−	1851-2008

this study 1991-2007). Although the sum of the 8 Reynolds terms characterize D_{bio} completely, the total *variance* in D_{bio} is equal to the sum of variances of each the 8 terms plus all their possible covariances according to:

$$\text{VAR}(D_{bio}) = \sum_{i=1}^{8} \sum_{j=1}^{8} \text{COV}(X_i X_j). \tag{2.8}$$

Applying this to Equation 2.7 gives a total of 64 (co-)variance terms. These terms placed in a covariance matrix facilitate a quick analysis of the major contributing terms of the total variability; both the variance of the single terms, as well as the covariances between terms. With the summation of the appropriate terms, we can isolate specific drivers of variability in D_{bio}. For instance, the variance caused by changes in the isodisequilibrium coefficient ($\overline{F}_{la}I'_{la}$) is expressed by the diagonal variance term. Any other covariances between ($\overline{F}_{la}I'_{la}$) and other terms can be obtained by adding up the off-diagonal covariances. By dividing $\text{VAR}(\overline{F}_{la}I'_{la})$ by $\text{VAR}(D_{bio})$ we can also obtain its relative contribution to the total variance in %. In a similar way, this method also allows separation of variance of other contributors.

2.2.4   Experimental setup

We ran SiBCASA globally, for each simulation, from 1851 through 2008. The initial carbon pool sizes were solved analytically by setting the time-derivatives of the pools to zero. This approximation implies biospheric steady state (NEE≈0); an assumption often made for biogeochemical models when observations of biomass are not available [*Schaefer et al.*, 2008]. Our datasets combined (meteorology, remotely sensed vegetation data, and GFED3) allowed a model run with actual driver data for the period 2000 through 2008. For each model year from 1851-1999, the meteorological driver datasets, satellite vegetation, and GFED3 fire data were randomly selected from the 2000-2008 dataset. Our framework therefore excluded any variability from long-term climate change effects, such as a rise in global temperature. The records of atmospheric δ_a and CO_2

concentration did have a realistic long-term trend, however. The monthly δ_a record, as a function of latitude, was based on ice-core measurements [*Francey et al.*, 1999], and from 1989 onwards, atmospheric observations (ftp://ftp.cmdl.noaa.gov/ccg/co2c13). The long-term trend of atmospheric CO_2 was taken from a curve fit of the GlobalView data set [*Masarie and Tans*, 1995] and included observed seasonal cycles derived at sites in the Northern Hemisphere, near equator, and Southern Hemisphere.

In this study we performed four different simulations (Table 2.1). All simulations included the prescribed records of atmospheric CO_2 and δ_a, the same C_3/C_4 distribution map, and the same SiBCASA driver files as described earlier. The ISOVAR simulation (we borrowed the same terminology as *Scholze et al.* [2003 and 2008]) included the dynamic fractionation scheme, whereas the ISOFIX simulation used fixed values for C_3 and C_4 plant discrimination (19.2 and 4.4 ‰ respectively) instead. In addition, the ISOFIX simulation was restarted from 1975 onward with fixed δ_a to investigate the variability induced by atmospheric ^{13}C/^{12}C ratios (ISOFIX-FA, Fixed Atmosphere). We ran a fourth simulation to investigate the extent to which exclusion of fire disturbances increased the D_{bio} flux. This simulation was similar to ISOVAR but lacked the fire fluxes (ISOVAR-NF, No Fires), where total carbon exchange remained largely unaffected because the excluded fire disturbances were compensated by increased respiration.

2.3 Results

2.3.1 Total δ^{13}C budget

We first addressed the question of whether simulated terrestrial flux IAV can close both the CO_2 and δ^{13}C budget under the assumption of low ocean flux IAV. Hence, we first closed the CO_2 budget (Equation 2.2 and Table 2.2), given the rate of change of CO_2, the rate of fossil fuel combustion, the rate of biomass burning, as well as the ocean exchange to be known, and thus assigning the remainder of budget to terrestrial net exchange. The solution to this 'single deconvolution' is shown graphically in Figure 2.2a. Increases in CO_2 from F_{ff} and F_{fire} were partly countered by uptake in the terrestrial biosphere and oceans. The remainder of the emitted CO_2 accumulated on average with $3.6 \, \mathrm{Pg\,C\,yr^{-1}}$ in the atmosphere. In particular, note the anti-correlation between N_{bio} and N_{oce} which cannot be uniquely solved for (two unknowns) using only CO_2 (one equation). Numerical results are given in Table 2.2. The four flux terms of the CO_2 budget were used to close the δ^{13}C budget in a double deconvolution (two unknowns, two equations).

After filling the budget terms on the right-hand side of the δ^{13}C equation 2.4 with values from SiBCASA and from other estimates, we obtained a sum of the mean isofluxes

TABLE 2.2: 1991-2007 averaged observed records of C_a d/dt δ_a and d/dt C_a balanced by the flux terms defined by Equation 2.2 and Equation 2.4. The left-hand side of both equations are separated from the right-hand side flux terms by a horizontal line. The mass balance of CO_2 and δ^{13}C include columns containing the standard deviation (1σ) and the variance ($1\sigma^2$) respectively of the linear detrended IAV. Other adopted values, which are also averaged over 1991-2007, are given in the most right-hand side columns. The sources of the data are provided by the footnotes.

Mass balance δ^{13}C budget $[\mathrm{Pg\,C\,‰\,yr^{-1}}]$				Mass balance C budget $[\mathrm{Pg\,C\,yr^{-1}}]$				other values	
	mean	1σ	$1\sigma^2$		mean	1σ	$1\sigma^2$		mean
C_a d/dt δ_a [a]	−18.7	± 21.32	454.41	d/dt C_a [a]	3.6	±1.00	1.01	δ_a [a]	−8.0 ‰
$F_{ff}(\delta_{ff} - \delta_a)$	−141.9	± 4.00	16.00	F_{ff} [b]	6.9	±0.24	0.06	δ_{ff} [b]	−28.6 ‰
$F_{fire}\epsilon_{ph}$	−27.8	± 2.30	5.28	F_{fire} [c]	1.8	±0.15	0.02	$\epsilon_{ph} = -\Delta$ [i]	−15.2 ‰
$N_{oce}\epsilon_{ao}$	4.2	± 0.37	0.14	N_{oce} [d]	−2.1	±0.19	0.04	ϵ_{ao} [j]	−2.0 ‰
$N_{bio}\epsilon_{ph}$	45.6	± 18.07	326.52	N_{bio} [e]	−3.0	±1.19	1.42	C_a [a]	779.2 Pg C
D_{bio} [f]	25.4	± 1.46	2.14	covariances [h]	0		−0.53	d/dt δ_a [a]	−0.024 ‰ yr^{-1}
D_{oce} [g]	48.7	± 1.48	2.21						
residual [h]	27.1	± 10.11	102.12						

a Observed global average derived from the Cooperative Air Sampling Network of NOAA/ESRL and INSTAAR/SIL.
b Global average compiled from CDIAC and British Petrol Statistical Review of World Energy.
c Global average calculated by SiBCASA biomass burning module.
d Global average estimated by *Le Quere et al.* [2007].
e Global average estimated by closing the average carbon budget (Equation 2.2).
f Global average calculated from SiBCASA's records of F_{la}, F_{fire}, δ_v^{eq}, δ_v, and δ_{fire}.
g Global average calculated from observed records of pCO$_2$ and δ^{13}C in dissolved inorganic carbon, and estimated F_{oa}.
h Leftover residuals to close the CO$_2$ and δ_a budgets (Equation 2.2 and Equation 2.4).
i Land fractionation during photosynthetic uptake calculated as Δ by SiBCASA.
j Ocean fractionation during air-sea transfer.

of ^{13}CO$_2$ that required an additional $\sim$27 Pg C ‰ yr^{-1} to match the left-hand side (see Table 2.2). In addition, more than 100 $[\mathrm{Pg\,C\,‰\,yr^{-1}}]^2$ of IAV was missing in the simulated budget. Although this seemed like a large missing fraction, closer inspection pointed to only a few processes that dominated the budget and thus could be held responsible. We illustrate this in Figure 2.2b with numerical values given again in Table 2.2.

The mean observed δ^{13}C growth rate (C_a d/dt δ_a) was negative (black line) and showed a considerable amount of variability (*mean ± 1σ detrended standard deviation*: −18.7 ± 21.3 Pg C ‰ yr^{-1}). The negative sign in the mean flux implies that the atmosphere became increasingly depleted in ^{13}CO$_2$ relative to ^{12}CO$_2$. On the mean flux side, combustion of isotopically light fossil fuels (shaded brown) dominated this draw down, with a small contribution from fires (shaded red). Neither one of these calculated terms had much variability, but the fire contribution (−27.8 ± 2.3 Pg C ‰ yr^{-1}) may be more variable than simulated in SiBCASA because of its intermittent nature and capacity to shift between C$_3$ and C$_4$ dominated ecosystems, with large consequences for its signature.

The sum of these two negative terms ($\sim$ −170 Pg C ‰ yr^{-1}) was partly balanced by
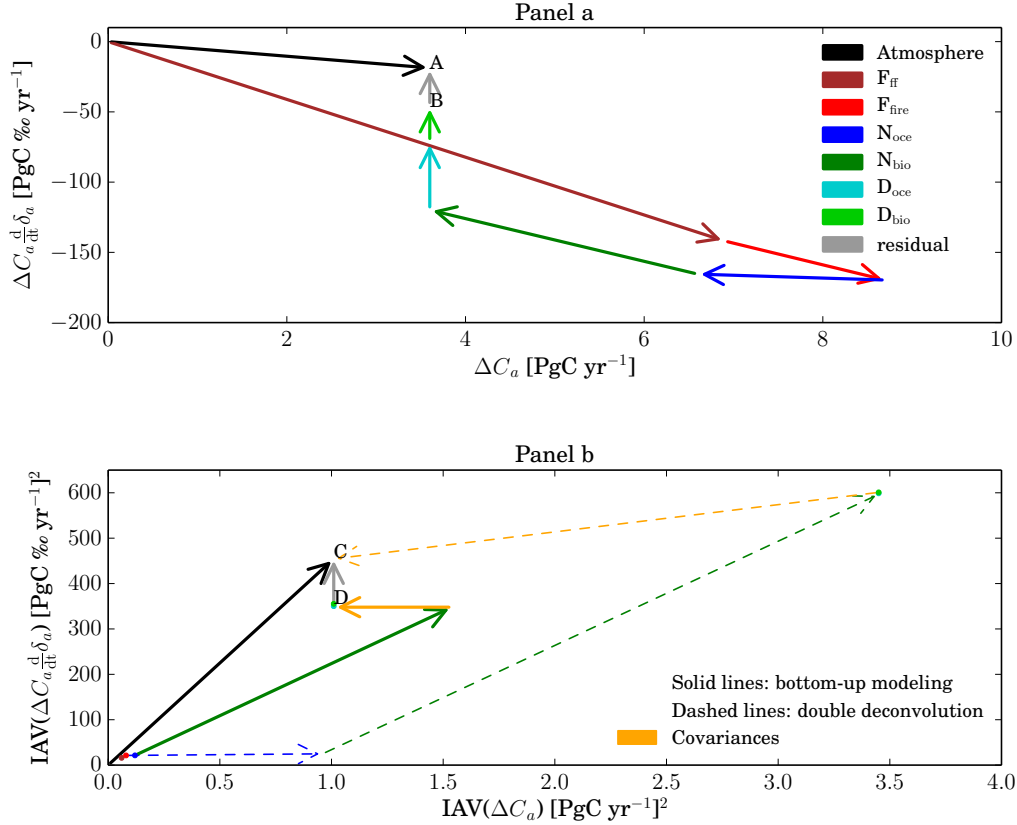
FIGURE 2.1: In panel (a) the vector plot of the average rate of change of CO_2 and δ^{13}C observed in the atmosphere (black vector pointing to A) and the contributions from the different bottom-up terms from Equation 2.2 and Equation 2.4 (add up to point B). The gap between A and B represents the missing mean $27.1\,\mathrm{Pg\,C}\,\permil\,\mathrm{yr}^{-1}$ isoflux in the δ^{13}C budget, which could be accounted for by scaling D_{bio} and D_{oce}. Panel (b) shows the vector plot of the IAV ($1\sigma^2$) in the fluxes. Again, observed IAV is depicted by the black vector pointing to C, and the colored vectors (pointing to D) represent the different terms of the CO_2 and δ^{13}C budgets. The smallest terms of the budget are presented as dots. Covariances, largely due to anti-correlation between N_{bio} and N_{oce} are depicted by the orange vectors. Moving the model representation of IAV at point D towards observed IAV at point C requires either (1) more IAV in the disequilibrium fluxes, shown by the solid vectors or (2) more IAV in the land and ocean uptake fluxes shown by the dashed vectors.

four positive flux terms that tended to increase the ratio of $^{13}CO_2$ and $^{12}CO_2$ in the atmosphere. Of these four fluxes, the ocean disequilibrium term (light blue) had the strongest impact on the balance, but was estimated to have only small IAV ($48.7 \pm 1.5\,\mathrm{Pg\,C}\,\permil\,\mathrm{yr}^{-1}$). This is a consequence of large gross CO_2 fluxes towards the atmosphere and the relatively large isotopic difference between δ^{13}C in the ocean surface and atmosphere. The role of net CO_2 exchange in the oceans (blue) was small ($4.2 \pm 0.4\,\mathrm{Pg\,C}\,\permil\,\mathrm{yr}^{-1}$) due to the low IAV in ocean model simulations, and the assumed constant fractionation of $-2\,\permil$.

Exchange with the terrestrial biosphere also contributed through a net flux and a disequilibrium term. The net terrestrial biosphere CO_2 exchange (green) contributed strongly to the mean isoflux and also caused large IAV in simulated isofluxes ($45.6 \pm 18.1 \, \mathrm{Pg\,C\,\permil\,yr^{-1}}$). The terrestrial disequilibrium D_{bio} was important for the mean budget, but exhibited quite low IAV ($25.4 \pm 1.5 \, \mathrm{Pg\,C\,\permil\,yr^{-1}}$), even when variations in C_3 discrimination and changes in C_3:C_4 productivity were included (ISOVAR). When excluded, the variability was reduced even further to $\pm \, 1.2 \, \mathrm{Pg\,C\,\permil\,yr^{-1}}$ (ISOFIX).

This poses the question $-$ why did the simulated budget miss $27.1 \pm 10.1 \, \mathrm{Pg\,C\,\permil\,yr^{-1}}$ of isofluxes? Arrow diagrams of the CO_2 and δ^{13}C budgets (Figure 2.1) provide a visual aid to identify the terms that can provide extra leverage. Point A in Figure 2.1a represents the measured growth rate in the atmosphere that we were trying to match, but adding all the bottom-up terms culminated in point B, i.e., $27.1 \, \mathrm{Pg\,C\,\permil\,yr^{-1}}$ less than needed to close the budget. The disequilibrium fluxes do not affect the CO_2 budget; hence, they only appear as vertical vectors. Moving from B to A can therefore be achieved relatively easily by scaling the vertical ocean and land disequilibrium vectors as in *Alden et al.* [2010]. This can be justified as the processes that determine these fluxes, on land especially, are still uncertain. The gross CO_2 fluxes towards the atmosphere and the turn-over times of the carbon pools as simulated in SiBCASA were not constrained by observations. More problematic, however, was the fraction of variability in the budget that is unaccounted for in our simulations. In Figure 2.1b, point C represents the observed IAV in the atmosphere, but we again fell short with our bottom-up framework and ended at point D, around $100 \, [\mathrm{Pg\,C\,\permil\,yr^{-1}}]^2$ under. Note that F_{ff}, F_{fire}, and N_{oce} only had a small influence on the IAV budget (their arrows are packed tightly together in the lower left corner) so adjustments to these fluxes would barely help to close the variability gap. In contrast, N_{bio} had a large influence on δ^{13}C IAV, but anti-correlated with the N_{oce}, as dictated by the CO_2 constraint, and thus could not be adjusted without a change in the latter. Thus, one of two solutions are available to close the double deconvolution budget (moving from D to C): (1) assume the missing IAV resides in D_{oce}, or more likely in D_{bio}, as per *Alden et al.* [2010], or (2) project all unexplained IAV onto the net uptake fluxes, as shown by the dashed vectors, as per *Ciais et al.*. Solution 1 appears easier, but is not supported by our bottom-up modeling as we will show in the next section. Solution 2, on the other hand, gives unrealistically large (and anti-correlating) IAV in both ocean and land uptake, and is also not supported by bottom-up modeling of net ocean fluxes [e.g., *Le Quere et al.*, 2007]. In Section 2.4 we will analyze the implications of this outcome and suggest possible alternative ways to close the budget. First, we will examine our terrestrial disequilibrium flux in more detail.
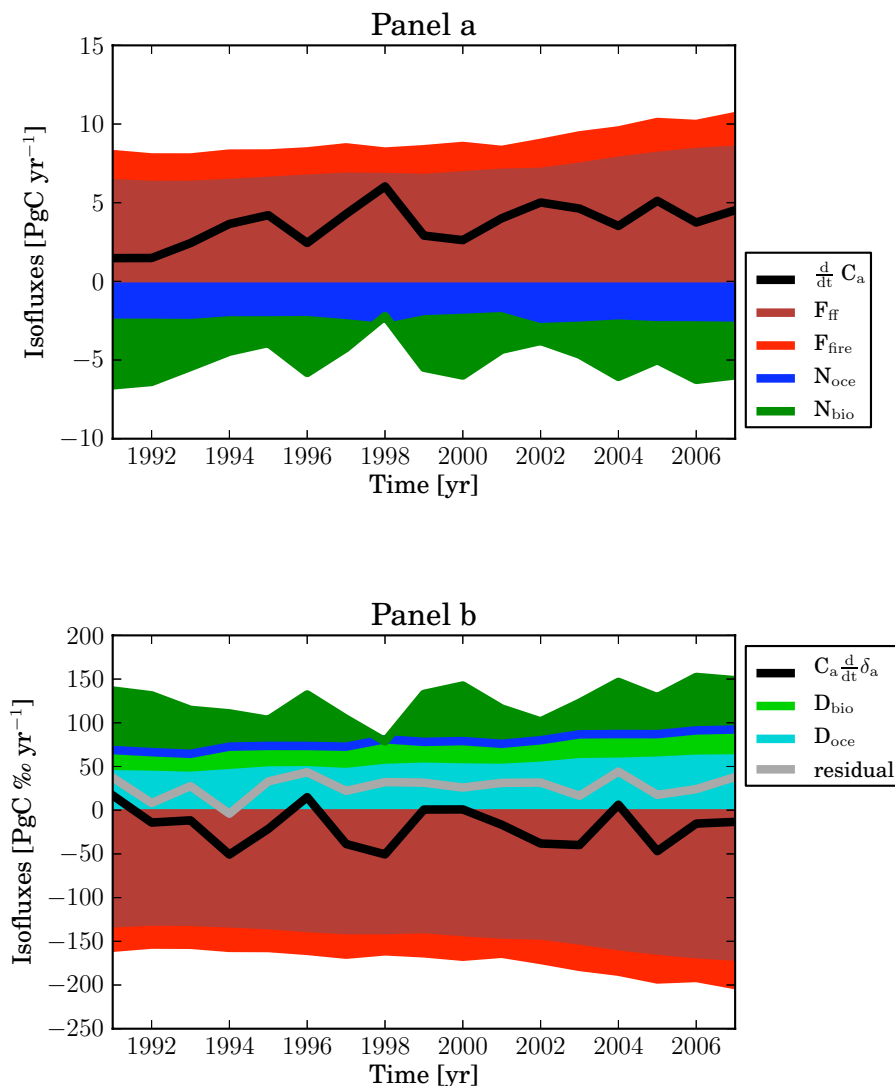
FIGURE 2.2: Timeseries of each term of the CO_2 budget Equation 2.2 in panel (a) and δ^{13}C budget Equation 2.4 in panel (b). The global annual isofluxes (right-hand side of the equations) are plotted as stacked area timeseries. Global annual observed $\mathrm{d}/\mathrm{dt}\, C_\mathrm{a}$ and $C_\mathrm{a}\, \mathrm{d}/\mathrm{dt}\, \delta_\mathrm{a}$ (left-hand side of the equations) are plotted using black lines, and the global annual residual isoflux is plotted as a gray line.

2.3.2   Variability in terrestrial fluxes

The results from the Reynolds decomposition applied on terrestrial disequilibrium flux (D_bio, Equation 2.7) is summarized graphically in Figure 2.3 in the form of a covariance matrix, where we show only the important contributing terms. The summations of different terms are in the same colors as in the schematic overview of important variability

contributions (Figure 2.4). The sum of the complete matrix gives the detrended year-to-year variability in D_{bio} (2.13 [Pg C ‰ yr^{-1}]^2, or $\pm$ 1.46 Pg C ‰ yr^{-1}). Three-quarters of the complete covariance matrix was responsible for only 4 % of total variability and is therefore omitted from Figure 2.3. The variability in terrestrial disequilibrium was mostly (96 %) due to respiration driven disequilibrium ($F_{la}I_{la}$), while fire driven disequilibrium ($F_{fire}I_{fire}$) had a negligible impact (4 %). This result was expected due to the small fire flux of 1.8 Pg C yr^{-1} and similarly small variability (± 0.2 Pg C yr^{-1}; 1σ). The contribution from fires can potentially be enhanced by higher fire emissions during El Niño events (e.g., 1997-1998), but in SiBCASA we did not simulate all processes thought to contribute to additional high fire emissions, like peat burning. Despite the small size of the variability there was a marked $\sim$10 % impact of fires on global total disequilibrium, as fires shorten the residence time of carbon in the biosphere and hence decrease the isotopic difference between respired carbon and assimilated carbon. This mostly affects tropical fluxes, where fires dominate and residence times are generally longer due to the preponderance of C$_3$ plant species. Between 1991-2007 the ISOVAR-NF simulation had a global average D_{bio} flux of 27.1 Pg C ‰ yr^{-1}, as opposed to 25.4 Pg C ‰ yr^{-1} in the standard ISOVAR simulation.

Of the 96 % of respiration driven IAV in disequilibrium, only 6 % came from IAV in the respiration flux F_{la} (green), whereas 90 % came from IAV in the disequilibrium forcing coefficient I_{la} (purple). This is in good agreement with the conclusions of *Scholze et al.* [2008] and *Alden et al.* [2010], who also ascribe terrestrial disequilibrium variability to isotopic forcing rather than respiration variations. This is physically consistent with the idea that respiration variability is fundamentally limited by the large pool sizes from which it comes. Variability in I_{la} was further decomposed into three parts: (1) 19 % of variability in I_{la} resulted from variations in the global averaged discrimination factor Δ as the relative uptake (GPP) over C$_3$ vegetated areas (with large Δ_{C3}) and C$_4$ vegetated areas (with small Δ_{C4}) shifted, e.g., a 0.5 % relative increase of C$_4$ GPP caused a 0.08 ‰ reduction in global average Δ; (2) an additional 48 % increase in variability resulted from variations in the atmospheric δ_a, which together with the global Δ determined δ_v^{eq}; and (3) a further 33 % came from changes in Δ_{C3}, which is the second contributor to global averaged Δ and was assumed to vary only in C$_3$ plants acting mostly as a short-term response to drought conditions. This latter contribution was excluded in the ISOFIX simulation and its variability in our simulations was slightly smaller than in *Scholze et al.* [2003]. In contrast, our simulations showed larger variations in the C$_3$/C$_4$ contributions to global Δ as opposed to Δ_{C3}. Compared against the total variability in D_{bio}, the three contributors in I_{la} together represented 90 % of the variability with the following relative contributions: (1) 17 %, (2) 43 % and (3) 30 %.
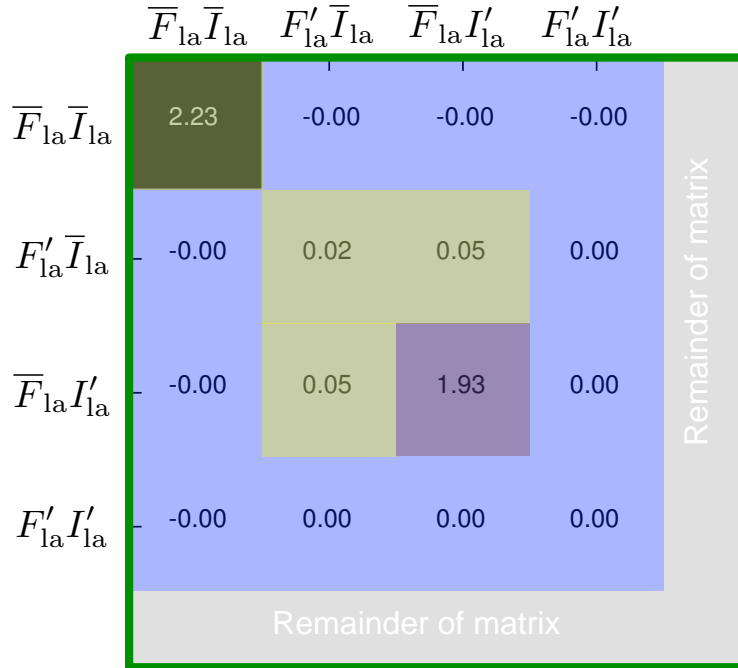
FIGURE 2.3: The outcome of Reynolds decomposition (Equation 2.7) applied to a covariance matrix. The sum of the whole matrix equals the total IAV in D_{bio} and is indicated by the green border. We let the mean fluxes and disequilibrium coefficients include a linear trend over the period investigated (1991-2007). We therefore exclude the covariance term between the mean terms in our summations (black box) as they provide no information about year-to-year variations. The sum of the gray area represents only a small portion of the total IAV, which is mainly caused by covariances between biomass burning and biological respiration (off diagonal terms). Everything inside the blue area represents the IAV caused by biological respiration. Contributions are further dissected between I_{la}' (purple) and a selection of the remainder terms (light green).

Given that the variability from D_{bio} was rather low, much of the terrestrial variability originated from the net exchange flux (N_{bio}), as we saw in the previous section. An interesting aspect is that less IAV in N_{bio} and N_{oce} was required to explain the observed year-to-year changes in atmospheric CO_2 and $\delta^{13}C$ if GPP and plant discrimination covary in response to drought stress. This idea was first presented by *Randerson et al.* [2002], who assumed that a 1 % increase in GPP would result in a 0.5 % increase in discrimination when solving their double deconvolution setup. This resulted in a substantial reduction of the minimum to maximum range of the yearly terrestrial and ocean carbon sinks (0.7 Pg C yr^{-1} and 0.4 Pg C yr^{-1}, respectively), compared to a double deconvolution with constant discrimination.

In SiBCASA the drought responses of C$_3$ GPP and fractionation were included in the model itself, as reductions in relative humidity (RH) and water stress tend to close the

leaf stomata. This reduces GPP and the day-time chloroplast-atmosphere (c_c/c_a) ratio, and hence, simultaneously reduces Δ_{C3} through Equation 2.1. We find that linearly detrended C_3 GPP and Δ_{C3} did indeed covary ($r = +0.6$) as hypothesized by *Randerson et al.* [2002], but only 10 % of the total variability in the isoflux (GPPΔ_{C3}) came from covariances, as opposed to the 45 % we would obtain if we used the GPP-Δ_{C3} dependence proposed by *Randerson et al.* [2002]. This raises an important question as to whether the *Randerson et al.* hypothesis is realistic, or the sensitivity of GPP and discrimination to climate variations is parameterized correctly in SiBCASA.

1. **Total detrended D_{bio}**
   ± 1.46 PgC‰/yr (2.13)
2. Fire driven D_{bio}
   ± 0.29 PgC‰/yr (0.08)
3. **Respiration driven D_{bio}**
   ± 1.43 PgC‰/yr (2.05)
4. F_{la} and other terms
   ± 0.36 PgC‰/yr (0.12)
5. I_{la}
   ± 1.39 PgC‰/yr (1.93)

I_{ba} further separated in three parts:

- Variability from C3/ C4 productivity
- Variability from C3 Δ
- Variability from δa
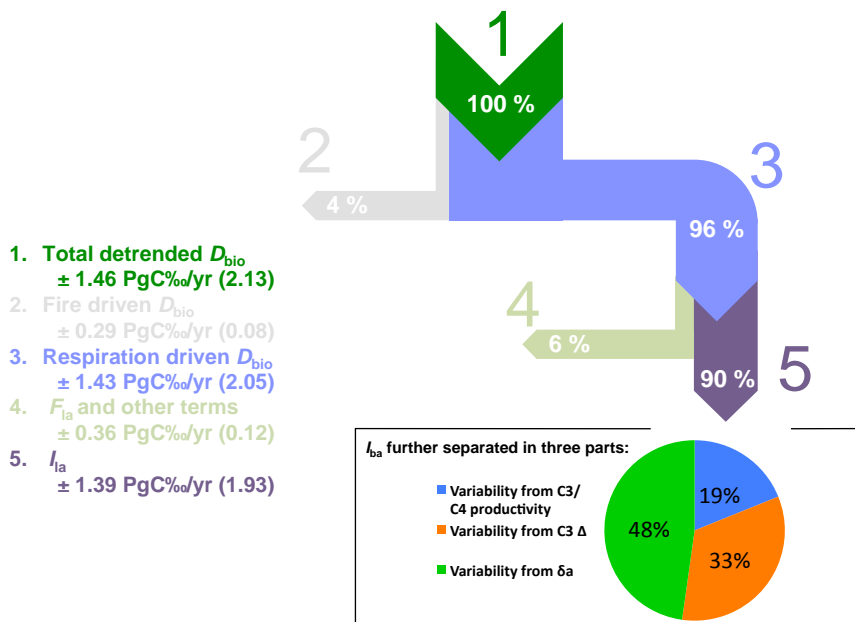
FIGURE 2.4: Schematic outcome of the important processes contributing to total IAV in ISOVAR D_{bio} ($2.13\,[\mathrm{Pg\,C\,‰\,yr^{-1}}]^2$, $1\sigma^2$). Colors and percentages of different components correspond with the summed areas in the covariance matrix in Figure 2.3. The numbered processes include 1σ standard deviation and $1\sigma^2$ variance in parentheses. At the top of the figure, the total detrended variability in D_{bio}, which holds 100 % of the IAV, is separated into a respiration component ($2.05/2.13 = 96\%$ of total IAV) and a rest term that includes fire effects ($0.08/2.13 = 4\%$ of total IAV). The respiration component is further separated into contributions from $\overline{F_{\mathrm{la}}}I'_{\mathrm{la}}$ ($1.93/2.13 = 90\%$) and $F'_{\mathrm{la}}\overline{I_{\mathrm{la}}}$ including other rest terms ($0.12/2.13 = 6\%$). In $\overline{F_{\mathrm{la}}}I'_{\mathrm{la}}$, the fluctuations originate from three processes: variability in C_3/C_4 uptake ratio affecting global Δ (19 %), variability in Δ_{C3} (33 %) and variability in δ_a (48 %). The variability from changes in C_3 and C_4 uptake was determined from the variance in the ISOFIX-FA simulation. The variability from Δ_{C3} was determined by analyzing the difference in variance between ISOVAR with the ISOFIX simulations. The δ_a variability was determined by comparing the variance of ISOFIX and ISOFIX-FA.

2.3.3   Variability in δ^{13}C observations

The single largest number in the IAV budget of δ^{13}C is variation in the growth rate itself ($C_a \, \mathrm{d}/\mathrm{d}t \, \delta_a$, Table 2.2). This number is the product of a very large atmospheric CO_2 abundance (C_a), and a small δ_a growth rate ($\mathrm{d}/\mathrm{d}t$). As a consequence, small errors in the growth rate of δ_a are highly magnified in the final budget necessitating a closer examination of its uncertainty.

The red line in the first two panels of Figure 2.5 shows the 17-year evolution of CO_2 and δ_a determined from a set of 39 marine boundary-layer (mbl) sites. The seasonal variations in CO_2 and δ_a clearly anti-correlate as summertime CO_2 uptake leaves the atmosphere heavier in ^{13}C, whilst on the decadal time scale the increase of CO_2 due to fossil fuel emissions causes an opposite trend in δ_a as isotopically light fossil fuel carbon (with a mean signature of $-28.6\,‰$) is added. The annual growth rate for δ_a in the third panel is determined from the difference between consecutive δ_a values, as is commonly done. The similarity between the δ_a growth rate in the third panel and the isoflux term ($C_a \, \mathrm{d}/\mathrm{d}t \, \delta_a$) in the fourth panel indicates that the IAV in the latter term is dominated by δ_a growth rate variations and not by C_a variability.

To determine the uncertainty in the growth rate and atmospheric isoflux, we followed the bootstrapping procedure introduced by *Masarie and Tans* [1995] and used 100 alternative atmospheric monitoring configurations for the global network. A total of 39 random sites were drawn (with replacement) from the available network of 39 observing mbl sites, and subsequently used to determine $\mathrm{d}/\mathrm{d}t \, \delta_a$ and $C_a \, \mathrm{d}/\mathrm{d}t \, \delta_a$. We ensured that the random set of mbl sites specified for δ_a were identical to those for CO_2 for each bootstrap realization. This ensured that CO_2 and δ_a trends determined from each bootstrap run were comparable. The random selection of sites thus addressed the uncertainty in the global $C_a \, \mathrm{d}/\mathrm{d}t \, \delta_a$ that results from an incomplete and uneven coverage of the globe by the network. The different growth rates resulting from the bootstrap analysis are shown graphically in the four panels in Figure 2.5 using gray lines.

The distribution of IAV ($1\sigma^2$, over 17 years) from the 100 realizations is provided in the histograms on the right-hand side of the third and fourth panel. The mean IAV value is approximately $450\,[\mathrm{Pg\,C\,‰\,yr^{-1}}]^2$, which is close to the mean IAV realization recorded in Table 2.2. Most importantly, we find that this IAV can deviate significantly and can range from 400 to $500\,[\mathrm{Pg\,C\,‰\,yr^{-1}}]^2$ within a $68\,\%$ confidence interval. In other words, IAV in the global growth rate of δ_a leaves significant room for smaller, or greater, atmospheric variability. This confidence interval is about three times larger than the calibration variability in δ_a measurements [*Alden et al.*, 2010].
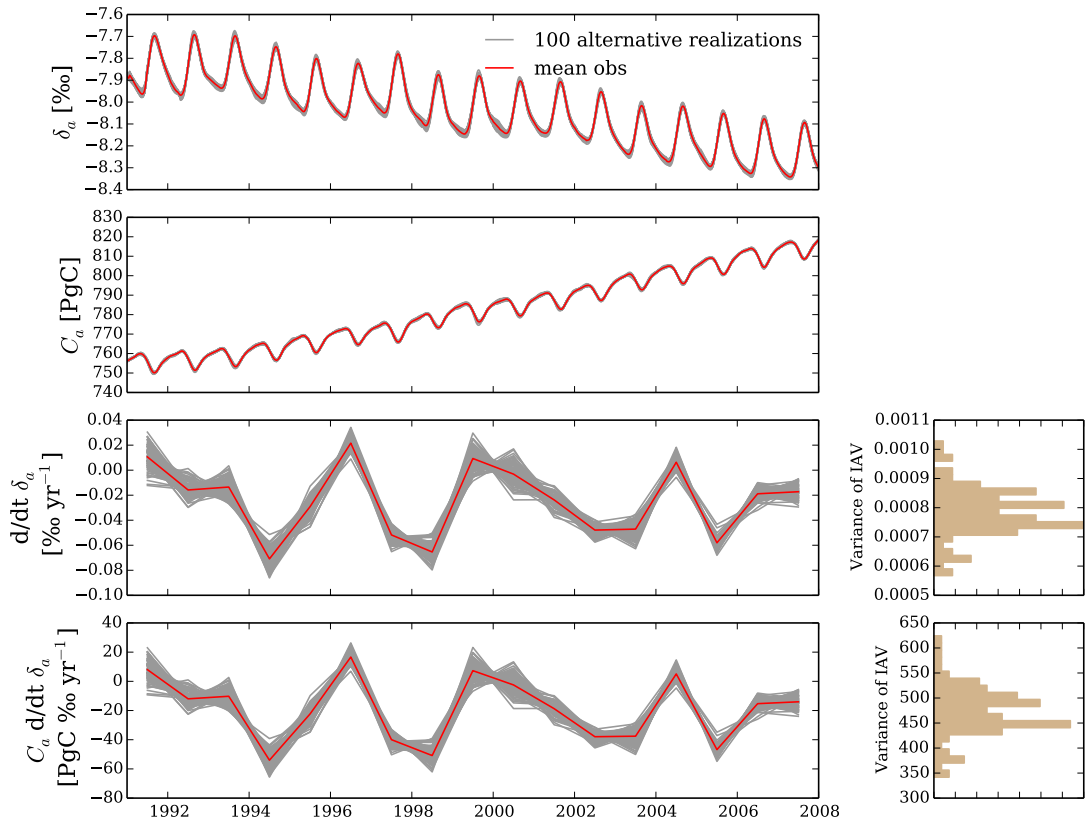
FIGURE 2.5: Four time series of δ_a, C_a, $d/dt\,\delta_a$, and $C_a d/dt\,\delta_a$. In the upper panel, we displayed the 100 realizations of δ_a from the bootstrap analysis (gray) and the mean δ_a in ‰ (red). The same configuration is shown in the second panel, but with the atmospheric CO_2 content in Pg C. By taking the first δ_a value from one year minus the first value of the previous year we determined the mean (red) and each of the 100 (gray) $d/dt\,\delta_a$ and $C_a d/dt\,\delta_a$, respectively. The last two panels are accompanied by a distribution histogram showing the IAV in $1\sigma^2$ ($[‰\,yr^{-1}]^2$ and $[Pg\,C\,‰\,yr^{-1}]^2$) of each of the 100 realizations.

This result has potential consequences for our analysis of the IAV budget of δ_a. If the true atmospheric IAV is towards the lower end of our estimates (1σ: $\pm20\,Pg\,C\,‰\,yr^{-1}$, $1\sigma^2$: $400\,[Pg\,C\,‰\,yr^{-1}]^2$), the residual IAV required to close the budget would be $\pm6.9\,Pg\,C\,‰\,yr^{-1}$, as opposed to the current $10.1\,Pg\,C\,‰\,yr^{-1}$ (see Table 2.2). The unexplained fraction of IAV to be projected onto net terrestrial and ocean CO_2 fluxes in a traditional double deconvolution with CO_2 and δ_a would thus be smaller, as would the IAV in the resulting fluxes. For the oceans this would mean that atmospherically based estimates are in closer agreement with bottom-up ocean models, as *Alden et al.* [2010] achieved with an IAV increase in disequilibrium fluxes. Net terrestrial CO_2 flux IAV would also be lowered, bringing the large IAV ($\pm1.6\,Pg\,C\,yr^{-1}$) currently estimated in a double deconvolution closer (a reduction of $\sim0.2\,Pg\,C\,yr^{-1}$ in standard deviation) to estimates based on CO_2 observations only ($\pm1.2\,Pg\,C\,yr^{-1}$). We note, however, that this sensitivity is not large

enough to bring bottom-up modeling and single-deconvolution based flux estimates in full agreement with the double deconvolution, as the latter still generates a substantial amount of variability in N_{oce}. Note that the assumption that atmospheric IAV is lower than currently believed can equally likely be replaced by the assumption that IAV is in reality higher, until we investigate in more detail the ability of the current observing network to detect all variations in $\mathrm{d}/\mathrm{dt}\,\delta_{\mathrm{a}}$ resulting from all terrestrial and ocean carbon exchange. Attempts to improve our interpretation of these variations are currently being undertaken, but are beyond the scope of this work.

2.4 Discussion and conclusions

This study demonstrates a dichotomy between bottom-up and top-down estimates of IAV in the disequilibrium flux. From a top-down perspective, a closed δ^{13}C budget with low variability in net ocean exchange can be achieved if a substantial fraction of IAV resides in the terrestrial disequilibrium flux ($\pm 12.5\,\mathrm{Pg\,C\,\permil\,yr}^{-1}$ in *Alden et al.* [2010]). However, the bottom-up simulated variability in the terrestrial disequilibrium flux, as calculated in this study, is 8 times smaller ($\pm 1.5\,\mathrm{Pg\,C\,\permil\,yr}^{-1}$). Our results suggest that IAV in C$_3$ discrimination (Δ_{C3}) is one of the drivers of IAV in D_{bio}, as do the results in *Scholze et al.* [2003 and 2008]. As these two bottom-up terrestrial ^{13}C models agree on the rather small year-to-year variability in global discrimination, our study suggests that other factors beside Δ_{C3} (such as underestimated variations in modeled C$_3$ and C$_4$ productivity) make a substantial contribution to IAV in D_{bio}, but are not sufficient to produce the suggested $\pm\,12.5\,\mathrm{Pg\,C\,\permil\,yr}^{-1}$ D_{bio} variations in *Alden et al.* [2010]. It is possible that the fractionation parameterization scheme used (including stomatal conductance) is lacking sensitivity to water stress. Sensitivity of stomatal conductance to atmospheric water vapor, radiation, and temperature must be better quantified in the future since these properties together have an effect on the isotopic fractionation. Sensitivity in Δ_{C3} could also depend on the chosen stomatal conductance formulation, as shown by *Ballantyne et al.* [2010]. Increased IAV in either C$_3$/C$_4$ distributions or their relative responses to climate anomalies could invoke more IAV in global Δ, and thus indirectly in D_{bio} as well. Ultimately, if we cannot explain the unaccounted fraction of variability here, we must look to other terms in the budget equation.

The suggestion that the mean residual can easily be absorbed by D_{bio} has already been discussed in Section 2.3.1 and in *Alden et al.* [2010]. The traditional double deconvolution solution, as presented under option (2) in Section 2.3.1 and in Figure 2.1b (dashed lines), warrants further discussion. The 17-year average land sink N_{bio} and ocean sink N_{oce}

would remain unchanged at -3 and $-2.1\,\mathrm{Pg\,C\,yr^{-1}}$, respectively. The IAV in N_{bio} and N_{oce} increases considerably, however, towards ±1.6 and $\pm0.9\,\mathrm{Pg\,C\,yr^{-1}}$ with a strong anti-correlation, as previously noted. The latter number for ocean IAV is not considered realistic based on recent ocean carbon exchange estimates [e.g., *Le Quere et al.*, 2007]. The variability in biospheric exchange is also higher than current estimates, e.g., in CarbonTracker [*Peters et al.*, 2007]. This is based on CO_2 inversions alone and could therefore simply lack vital information from δ^{13}C data. Spatially and temporal explicit solutions of CO_2 and δ^{13}C inversions are discussed in Chapter 4.

One of the budget terms under investigation was the atmosphere. In Section 2.3.3 we found that the constraint on the IAV of δ_{a} growth rate might not be as robust as previously thought. Out of the 100 realistic realizations of $C_{\mathrm{a}}\,\mathrm{d/dt}\,\delta_{\mathrm{a}}$ we found a realistic spread of $\pm50\,[\mathrm{Pg\,C\,\permil\,yr^{-1}}]^2$ in IAV, which is large compared to most variance terms in Table 2.2. One of the limitations of the network used is that the region with likely high isotopic variability is also the one that is least observed. Tropical carbon exchange is a strong mixture of C_3 and C_4 dominated species, and their signals are quickly transported from the surface to higher altitudes and could be hidden from the network for some time. Furthermore, interannual variations in the vertical mixing strength would contribute to the signal remaining at the surface, but it cannot be accounted for in the global mass balance calculations presented here. Inclusion of vertical profile observations that are increasingly becoming available could help further close the δ^{13}C budget. The large uncertainty on IAV in the atmospheric burden also poses the question whether previous carbon flux inversion studies that included atmospheric δ_{a} took the 'lack of constraint' in observed IAV into consideration, forcing an unnecessarily high IAV to be invoked in the ocean and terrestrial net exchanges fluxes. However, it should be noted that our analysis of the ^{13}C growth rate uncertainty could just as likely enlarge the residual variance of $100\,[\mathrm{Pg\,C\,\permil\,yr^{-1}}]^2$ as reduce it; in either case the central value of IAV for the growth rate would remain unchanged at $450\,[\mathrm{Pg\,C\,\permil\,yr^{-1}}]^2$.

It is also worth considering if D_{oce} could be another candidate for additional IAV. As in *Alden et al.* [2010], we assumed that ocean disequilibrium IAV is reasonably well described and an unlikely source for atmospheric ^{13}C variability. The small IAV of $\sim2\,[\mathrm{Pg\,C\,\permil\,yr^{-1}}]^2$ in the calculated value of D_{oce} (see Table 2.2 and Figure 4 in *Alden et al.* [2010]), results from interannual changes in both I_{oce} and F_{oa}. For I_{oce} ($=\delta_{\mathrm{a}}^{\mathrm{eq}}-\delta_{\mathrm{a}}$), $\delta_{\mathrm{a}}^{\mathrm{eq}}$ changes as a result of changing surface ocean ^{13}C of DIC, prescribed according to Figure 15 in *Gruber et al.* [1999]. The impact of changes in ^{13}C of DIC resulting from, e.g., reduction in upwelling waters in the eastern tropical Pacific during El Niño and the impact of sea surface temperature changes affecting the equilibrium fractionation factor [*Zhang et al.*, 1995] are neglected. F_{oa} is parameterized as a function of surface ocean

pCO_2 and wind speed, after *Takahashi et al.* [2009]. Although pCO_2 is assumed to increase according to the atmospheric CO_2 trend, wind speed (and sea water solubility) is assumed to be constant from year-to-year. While there is some room for additional variability beyond that specified, the argument put forward in Section 2.3.2 that respiration variability is fundamentally limited by the large pool sizes from which it comes is even more appropriate for the gross ocean-to-atmosphere flux. Uncertainty in the IAV of I_{oce} resulting from changes in ^{13}C of DIC are probably small because of the pool size effect. Sea surface temperatures can affect the equilibrium fractionation factor at a rate of $0.1\,‰\,K^{-1}$ [*Zhang et al.*, 1995]. In the ENSO regions SST can change significantly, but these are also regions of low wind speed where F_{oa} (and thus D_{oce}) is likely to be small. Although the IAV of D_{oce} deserves more rigorous treatment, we feel it is an unlikely candidate to explain the residual variance in Table 2.2.

Another potential candidate that can account for the unexplained fraction of variability is the fossil fuel isoflux. If we assume $\pm 0.2\,Pg\,C\,yr^{-1}$ as a realistic uncertainty in F_{ff} and prescribe this as IAV, we need an IAV of $\pm 1.3\,‰\,(1\sigma)$ in global mean δ_{ff} to produce a fossil fuel isoflux with enough IAV to close the variability gap. This begs the question: is such an IAV in δ_{ff} realistic? The total yearly isotopic ratio δ_{ff} can be separated into contributions from different fuel types, where each type has its own characteristic range of isotopic signatures, i.e., $\delta_{ff} = (F_{coal}\delta_{coal} + F_{oil}\delta_{oil} + F_{gas}\delta_{gas})/F_{ff}$. The signatures themselves have uncertainties but δ_{coal} and δ_{oil} are known to be within 1 or $2\,‰$. The isotopic composition of natural gas is much more variable and even within a single production field the isotopic signature can vary widely. The global average isotopic signature for natural gas is typically $-44\,‰$, while deviations exist if natural gas is either associated with coal or with marine sediments [-20 or $-100\,‰$ respectively; *Andres et al.*, 2000]. This makes the estimation of global weighted averages difficult [*Andres et al.*, 2000] and in that light, varying contributions to the global total fossil fuel mixture by natural gas of varying isotopic signatures could provide additional IAV. Interestingly, in the past when F_{ff} was 4 or $5\,Pg\,C\,yr^{-1}$, both uncertainty and variability in δ_{ff} was only half as important as it is today.

In conclusion, our main questions are answered. (1) Our new terrestrial bottom-up results cannot confirm the *Alden et al.* [2010] suggestion of a closed $\delta^{13}C$ budget that allows low prescribed ocean net exchange variability. As our model calculates low IAV in terrestrial disequilibrium flux, it suggests that other terms in the mass balance must accommodate the unaccounted variability. We identify several possible candidates: the atmospheric term, the fossil fuel emissions, and the terrestrial CO_2 net exchange term. Considering the small isofluxes, variability in forest fires is unlikely to provide the necessary leverage. (2) We found that C_3 GPP and Δ_{C3} do covary as suggested by *Randerson et al.* [2002], but their contribution to the variance in the C_3 uptake isoflux is rather small (10 %).

And finally, (3) we found that variations in Δ_{C3}, C_3 and C_4 productivity, and δ_a are the main drivers of variability in the disequilibrium flux. Fire and respiration variations play a minor role. We cannot rule out the possibility of more variability in globally averaged plant discrimination, either as a result of higher C_3 discrimination sensitivity to water stress than parameterized in the model, or more IAV in either C_3/C_4 distributions or their relative responses to climate anomalies.

Chapter 3

Terrestrial cycling of $^{13}CO_2$ by photosynthesis, respiration, and biomass burning in SiBCASA

Abstract

We present an enhanced version of the SiBCASA terrestrial biosphere model that is extended with: (a) biomass burning emissions from SiBCASA carbon pools using remotely sensed burned area data from the Global Fire Emissions Database (GFED), (b) an isotopic discrimination scheme that calculates ^{13}C signatures of photosynthesis and autotrophic respiration, and (c) a separate set of ^{13}C pools to transfer isotope ratios to heterotrophic respiration. We used the extended model to quantify the terrestrial exchange of CO_2 and $^{13}CO_2$ as a function of environmental changes in humidity and biomass burning.

Implementation of biomass burning produced similar fluxes as CASA-GFED both in magnitude and spatial patterns. Implementation of isotope exchange gave a global mean discrimination value of 15.2‰ and ranged between 4 and 20‰ depending on the photosynthetic pathway in the plant. These results compared favorably (annually and seasonally) with other published values. Similarly, the isotopic disequilibrium was comparable to other studies that included biomass burning. The newly modified starch/sugar storage

pools improved the propagation of isotopic discrimination anomalies to respiration, and results compared well with measurements. In addition, the amplitude of the drought response by SiBCASA was smaller than suggested by the measured isotope ratios. We also found that a slight increase in stomatal closure for large vapor pressure deficits amplified the respired isotope ratio variability. Our study highlights the importance of isotope ratio observations of ^{13}C to assess and improve biochemical models like SiBCASA, especially with regard to the allocation and turnover of carbon and the responses to drought.

3.1 Introduction

A key challenge in current carbon cycle research is to estimate the terrestrial and ocean carbon fluxes and to understand their variability. The accumulation of atmospheric CO_2 represents the sum of all sources and sinks and is currently widely used to close the carbon budget. For example, in the year 2010 $9.1 \pm 0.5\,Pg\,C$ (= $10^{15}\,g$) was emitted to the atmosphere as a result of fossil fuel emissions. Land use change added another $0.9 \pm 0.7\,Pg\,C$ to the atmosphere. The sum of these emissions put an additional burden of CO_2 in the atmosphere ($5.0 \pm 0.2\,Pg\,C$), with the remainder taken up by the terrestrial biosphere and oceans [*Peters et al.*, 2012]. How the sink can be partitioned among ocean and land remains hard to quantify.

Fortunately, as more and more isotope ratio observations become available, we now have the opportunity to use ^{13}C to provide information about the different exchange processes of carbon absorbed by the terrestrial biosphere and oceans. For example, measurements of the $^{13}C/^{12}C$ ratio in atmospheric CO_2 (designated as δ_a) have been used as an additional tracer alongside mole fractions of CO_2 [e.g., *Alden et al.*, 2010, *Ciais et al.*, 1995, *Keeling and Revelle*, 1985, *Keeling et al.*, 1989, *Nakazawa et al.*, 1993, *Rayner et al.*, 2008, *Siegenthaler and Oeschger*, 1987, *Tans et al.*, 1993]. Plants assimilate the heavier $^{13}CO_2$ molecules less efficiently than $^{12}CO_2$ (by approximately $2\,\%$), whereas net ocean exchange does not significantly discriminate against the heavier isotope (just $0.2\,\%$). The most dominant photosynthetic pathway in the terrestrial biosphere (C_3) also discriminates significantly more than the less common (C_4) pathway. Patterns in atmospheric CO_2 and δ_a are therefore potentially useful for providing insight into carbon fluxes.

The heterogeneous structure of the terrestrial biosphere and its response to weather and climate make CO_2 and $^{13}CO_2$ exchange variable in space and time. The extent to which plants discriminate against $^{13}CO_2$ is strongly dependent on environmental conditions that act on photosynthesis. A combination of atmospheric humidity, precipitation, and soil moisture are factors that determine the stomatally induced variations in isotopic

discrimination [*Farquhar et al.*, 1989, *Wingate et al.*, 2010]. In addition, the global distribution of C_3 and C_4 plants have a strong effect on the global mean discrimination [*Still et al.*, 2003]. Carbon that respires back to the atmosphere is heavier in ^{13}C than newly assimilated carbon and acts as an additional flux of $^{13}CO_2$ molecules towards the atmosphere (disequilibrium flux). This stems from a constant dilution of δ_a by isotopically depleted CO_2 from fossil fuel combustion [also known as the Suess effect; *Keeling*, 1979, *Suess*, 1955]. Errors in the representation of disequilibrium fluxes can lead to errors in the estimated land/ocean mean flux partitioning, as well as in the estimated variability of each sink. For example, an underestimation in the calculated isotopic signature of the carbon pools, or their turnover, could cause an underestimation of the disequilibrium flux, requiring a change in the estimated partitioning of the net biosphere flux and ocean flux. Current research efforts are therefore heavily focused on improving the realism of ocean and biosphere carbon exchange and its impact on the isotopic ratio.

A similar argument can be made for flux variability. *Alden et al.* [2010] and *van der Velde et al.* [2013] (previous chapter) showed that observed variability in $^{13}CO_2$ is difficult to reproduce when ocean variability is assumed to be low. To close the atmospheric ^{13}C budget the variability in the biosphere must be larger than currently accounted for in SiBCASA [*van der Velde et al.*, 2013]. The current lack of understanding of the atmospheric budget is therefore an important justification to explore isotope exchange with the atmosphere and the terrestrial biosphere in more detail.

Previously, significant attention has been given to realistic simulation of the seasonal and spatial variations of C_3 and C_4 plant discrimination, and the coupling between carbon assimilation and leaf CO_2 concentration on monthly time intervals [e.g., *Fung et al.*, 1997, *Lloyd and Farquhar*, 1994]. In recent studies more detailed process descriptions have been used to estimate plant discrimination [e.g., *Suits et al.*, 2005], but these models could not simulate the isotopic disequilibrium because they lacked descriptions of terrestrial carbon pools. *Scholze et al.* (2003 and 2008) used a full terrestrial cycling framework of CO_2 and $^{13}CO_2$ in the Lund-Potsdam-Jena dynamic vegetational model (LPJ). This model included the isotopic fractionation model of *Kaplan et al.* [2002] and above and below ground biogeochemical pools to store the total carbon and ^{13}C in consistent ratios.

In this study we developed several novel additions to the SiBCASA biosphere/biogeo-chemical model: (1) a representation of biomass burning emissions that are consistent with the predicted amount of standing biomass; (2) a framework of ^{13}C exchange, and (3) a modified storage pool to simulate isotopic signals in respired CO_2 more accurately. We investigated how the new model performed compared to similar models and observations,

and where there was need for improvement. We included an isotopic discrimination parameterization scheme from *Suits et al.* [2005] to simulate isotopic composition on a high spatial and temporal resolution. Our aim was three-fold: (1) to evaluate SiBCASA isotopic discrimination using published literature; (2) to evaluate SiBCASA return fluxes to the atmosphere, namely the isotopic disequilibrium and biomass burning fluxes; and (3) to simulate the short-term plant discrimination and respiration response to environmental conditions, and compare those with observations.

3.2   Methodology

3.2.1   SiBCASA model

The SiBCASA model [*Schaefer et al.*, 2008] combines two biogeochemical process models in a single framework. The biophysical part of the model is based on the Simple Biosphere model, version 3 [SiB, *Sellers et al.*, 1996a], with carbon biogeochemistry from the Carnegie-Ames-Stanford Approach [CASA, *Potter et al.*, 1993] model. The joint model framework calculates the exchange of carbon, energy, and water in 10 minute time intervals at a spatial resolution of 1×1 degrees. In the canopy air space the CO_2 concentration, temperature, and humidity are calculated as prognostic variables [*Vidale and Stockli*, 2005]. Effects of rainfall, snow cover, and aerodynamic turbulence are included in the computation of latent and sensible heat fluxes [*Sellers et al.*, 1996a].

For plant photosynthesis, SiBCASA uses the Ball-Berry stomatal conductance model as modified by *Collatz et al.* [1991] coupled to a modified version of the *Farquhar et al.* [1980] C_3 enzyme kinetic model and the *Collatz et al.* [1992] C_4 photosynthesis model. Leaf photosynthesis is scaled to the canopy level using the absorbed fraction of Photosynthetically Active Radiation (fPAR), derived from remotely sensed AVHRR Normalized Difference Vegetation Index [NDVI, *Sellers et al.*, 1994, 1996a, 1996b].

The photosynthetic carbon flux is calculated for two physiological plant types (currently C_3 and C_4). The global 1×1 degree map detailing the distribution (fraction) of C_4 plants was provided by *Still et al.* [2003]; a static map that represents the mean C_4 distribution for 1980s and 1990s. For grid cells that contain a fraction of both C_3 and C_4 plant types, carbon uptake is computed separately for each plant type, then combined into the carbon pools using a (fractional) weighted average. Respiration flux is then calculated from the combined pools.

As displayed in Figure 3.1a, the total amount of photosynthesized carbon ($^{13}C + {}^{12}C$) is allocated to a series of different live carbon pools (leaf, root, wood), surface litter
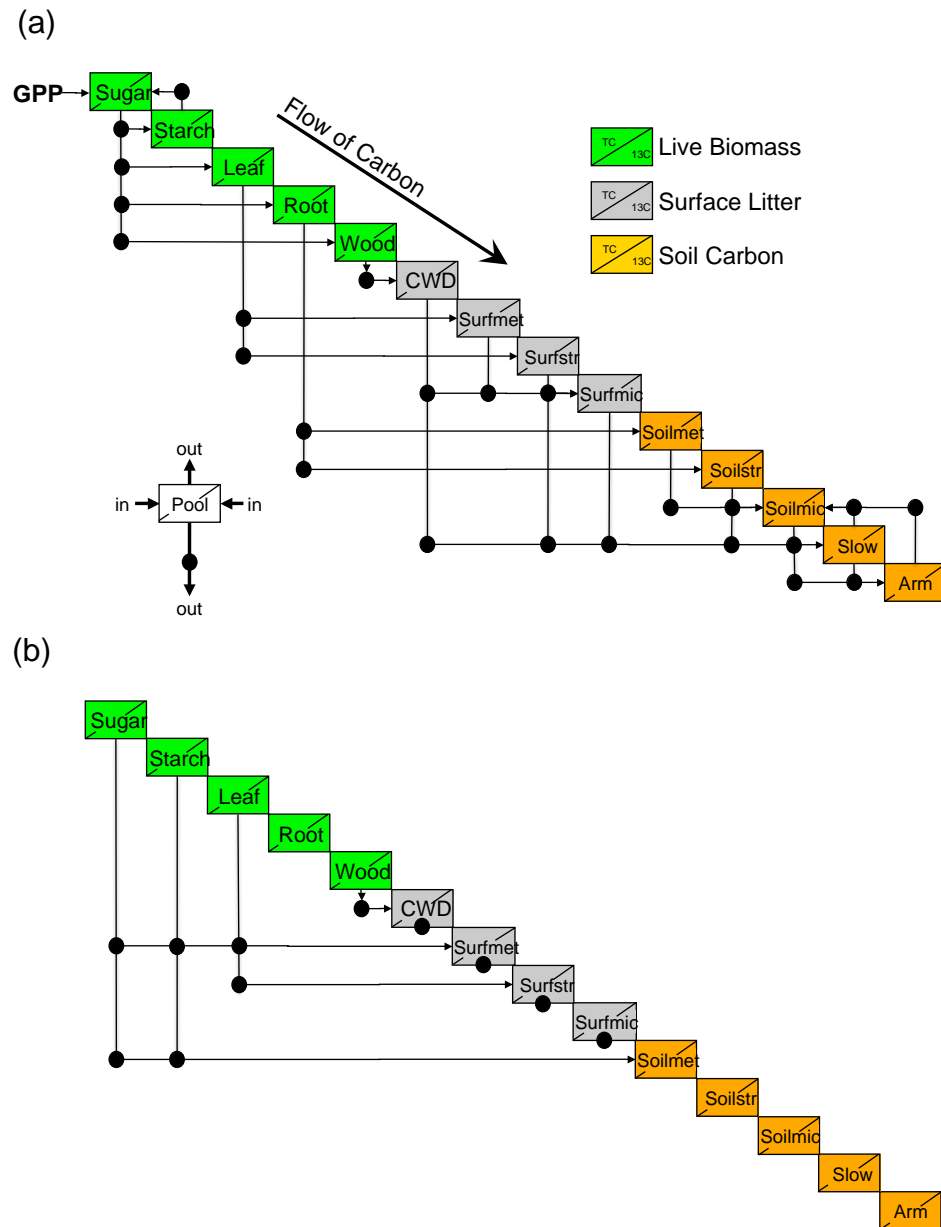
FIGURE 3.1: The modified SiBCASA pool configuration (a), where each box represents a total carbon (TC) and a ^{13}C pool. Carbon generally flows from upper left to lower right: vertical lines are losses from each pool, horizontal arrows are gains to each pool, and dots represent the transfer of carbon from one pool to another, where a fraction is lost to the atmosphere as respiration. GPP minus the canopy respiration puts sugars into the sugar pool, which becomes available for growth and maintenance of leaves, roots, and wood. Sugar and starch transform back and forth from one pool to the other to keep the ratio between sugar and starch close to 1:9. Dying of biomass is simulated by transferring carbon to the structural, metabolic, and microbial surface and soil pools. Autotrophic respiration results from growth and maintenance in the live biomass pools and heterotrophic respiration from microbial decay in the surface litter and soil carbon pools. The other pool configuration (b) displays the flow of carbon introduced by fire disturbances. Vertical lines represent pool losses, horizontal lines represent pool gains, and dots represent the TC and ^{13}C fire losses to the atmosphere.

pools (coarse woody debris, metabolic, structural, and microbial) and layered soil pools (metabolic, structural, microbial, slow, and armored). The amount of carbon in each of the 14 biogeochemical pools is solved prognostically as a first order linear differential equation depending on gains from other pools, losses to other pools and respiration losses due to (heterotrophic) microbial decay and (autotrophic) plant growth [*Schaefer et al.*, 2008]. The leaf pool is a special case because its carbon stocks are computed semi-prognostically. This means that photosynthesis calculations are constrained by remotely sensed leaf area and the leaf pool is prognostic, but can only vary within limits of remotely sensed leaf area.

$^{13}CO_2$ fluxes are computed in the isotopic discrimination model that we implemented in SiBCASA (see Section 3.2.2). We keep the ^{13}C stocks separate from the total carbon stocks by defining 14 additional biogeochemical pools for ^{13}C. Similar to total carbon, ^{13}C transfers from one pool to another as shown in Figure 3.1a. No discrimination effects are considered for transfer of carbon between pools and during respiration. The average turnover times and scaling factors for temperature, freezing, and moisture were taken from the original SiBCASA scheme. The separation of C_3 and C_4 pools is not yet realized, therefore carbon resulting from C_3 and C_4 photosynthesis is combined in a fractional weighted average to the same set of C pools. This is not ideal as C_3 and C_4 plants have their own turnover and environmental responses. We performed test simulations where we prescribed 100% coverage of either C_3 or C_4 photosynthesis depending on the dominant plant type in each grid cell, and this showed only a small reduction ($\sim 4\%$) in the global isotopic disequilibrium flux.

To improve simulated ^{13}C dynamics we added a second storage pool to simulate sugar and starch allocation separately. This type of configuration was required to improve exchange of ^{13}C signatures and is discussed in detail in Section 3.3.3. Originally, SiBCASA was designed with a single storage pool to represent the total amount of non-structural carbohydrates (sugars and starch). Of this storage, only the sugar portion, mainly in the form of sucrose, is readily available for plant growth [*Schaefer et al.*, 2008]. Sugars can be converted into starch and back if required, but the fraction of sugars in the storage pool is typically 5 to 30% depending on the plant species and time of year [*Barbaroux et al.*, 2002, *Gaucher et al.*, 2005, *Piispanen et al.*, 2001]. Based on observations of oak trees we assume a sugar fraction of 10% for all biomes [*Schaefer et al.*, 2008]. Given that only 10% of the storage pool is available for growth, the effective pool turnover is actually 10 times larger ($\sim 70\,$days) than the reference turnover of $7\,$days as dictated by the decay rate formulation (Equation 9) in *Schaefer et al.* [2008]. This was not an error but a consequence of having a combined storage pool of sugars and starch, of which only a fraction is available for plant growth. With the new storage pool we separated the sugar from starch by defining two storage pools. Using prescribed turnover rates for the

transfer of sugar-to-starch (7 day) and the transfer of starch-to-sugar (63 day) we allow carbon to transform back and forth from one pool to the other to keep the ratio between sugar and starch close to 1:9. Carbon used for plant growth comes from the sugar storage pool, which keeps the effective turnover time close to 7 days whilst maintaining a similar amount of carbon allocation and carbon exchange. The new double storage pool configuration is displayed in Figure 3.1a-b. This configuration was required to improve the simulation of coupled ^{12}C and ^{13}C dynamics, but is not necessary if only simulating the exchange of total carbon.

3.2.2 Isotopic discrimination

The CFRAX (carbon fractionation) scheme, used to calculate the $^{13}C/^{12}C$ isotopic ratios in the terrestrial exchange fluxes of CO_2, was inherited from the SiB2.5 model [*Suits et al.*, 2005]. These ratios are the result of several discrimination effects during the photosynthetic uptake of CO_2, where plants favor the more abundant $^{12}CO_2$ molecules as opposed to the heavier $^{13}CO_2$ molecules. From atmosphere to plant interior SiBCASA identifies three transport stages, where at each stage the CO_2 concentration is altered slightly due to a resistance. These stages are also associated with discrimination against $^{13}CO_2$. Discrimination effects are expressed as Δ in per mille, and are indicative of how much the isotopic ratio will change from one location to the next. See Section 1.5 for a detailed explanation on how to interpret the notation of isotopes and discrimination used in this chapter.

Total discrimination for C_3 plants (Δ_{C3}) is given by a weighted-sum of all transfer stages associated with photosynthesis [*Farquhar*, 1983]:

$$\Delta_{C3} = \Delta_b \left(\frac{c_a - c_s}{c_a} \right) + \Delta_s \left(\frac{c_s - c_i}{c_a} \right) + (\Delta_{diss} + \Delta_{aq}) \left(\frac{c_i - c_c}{c_a} \right) + \Delta_f \left(\frac{c_c}{c_a} \right), \tag{3.1}$$

where $c_{a,s,i,c}$ represent CO_2 in canopy air space, leaf boundary layer, stomatal cavity, and chloroplasts. The separate isotope effects are constant and determined from theoretical calculations and laboratory experiments [*Craig*, 1953, *Farquhar*, 1983, *Mook et al.*, 1974, *O'Leary*, 1984]. Two are related to molecular diffusion from canopy air space to leaf boundary layer ($\Delta_b = 2.9\,‰$) and molecular diffusion through the leaf stomata ($\Delta_s = 4.4\,‰$). Subsequently, smaller isotope effects occur during the dissolution of CO_2 in mesophyll and transport to the chloroplast ($\Delta_{diss} = 1.1$ and $\Delta_{aq} = 0.7\,‰$). The largest isotope effect is associated with fixation of CO_2 by the enzyme Rubisco in the chloroplast

($\Delta_f = 28.2\,‰$). A schematic representation of Equation 3.1 in relation to the flow of carbon is given in Figure 3 in *Suits et al.* [2005].

We assume the separate isotope effects remain constant, therefore variability in Δ_{C3} depends on the concentration gradient between the canopy air space and the leaf interior, which in turn depends on the opening and closing of leaf stomata (stomatal conductance). For instance, water deficiency would generally close the leaf stomata and decreases stomatal conductance, which results in a drop of the plant interior CO_2 concentrations (c_i and c_c). Consequently, a large CO_2 gradient will exist between the ambient atmosphere and interior plant. The discrimination term associated with CO_2 fixation by Rubisco (the final term in Equation 3.1) will disappear as the ratio c_c/c_a approaches zero. At the same time, however, more weight will be assigned to discrimination associated with molecular diffusion through the leaf stomata. When there is no water stress the opposite will happen: stomata remain open, therefore a small CO_2 gradient will exist that keeps the c_c/c_a ratio large, and thus more weight is assigned to the Rubisco fixation stage.

For C_4 plants we assume that all of the available carbon is fixed by Phosphoenolpyruvate carboxylase (PEPC). Therefore, similar to *Suits et al.* [2005], we only assume an isotopic effect associated with molecular diffusion at the leaf stomata, i.e., $\Delta_{C4} = 4.4\,‰$. *Brüggemann et al.* [2011] discuss several other possible fractionation steps associated with the transport of organic matter between different plant tissues, however these processes are not included in our model since the availability of such data remains scarce. Despite lab and field evidence for fractionation effects during allocation and respiration [*Bowling et al.*, 2008], these effects are not yet included in SiBCASA. The isotopic discrimination value (denoted as Δ, which can either refer to C_3 and C_4), is used to compute the ^{13}C and ^{12}C flux ratios of total carbon assimilation (F_{al}), canopy respiration ($F_{respcan}$) and net assimilation ($F_n = F_{al} - F_{respcan}$). Fluxes are given in µmol m^{-2} s^{-1}.

The $^{13}C/^{12}C$ ratio in the current net assimilated plant material (R_n) is determined by the relationship between discrimination Δ and the isotopic ratio of the atmosphere (R_a):

$$R_n = \frac{R_a}{\left(\frac{\Delta}{1000} + 1\right)}, \tag{3.2}$$

based on Equation 1.10 in Section 1.5. Subsequently, the ^{13}C and ^{12}C net assimilation rates are calculated by:

$$^{13}F_n = \frac{R_n \cdot F_n}{1 + R_n}, \tag{3.3}$$

$$^{12}F_n = \frac{F_n}{1 + R_n}. \tag{3.4}$$

The latter two fluxes are calculated separately for physiological plant types C_3 and C_4 and, in combination with the prescribed fraction of C_3 plants (β), a grid cell averaged flux is calculated:

$$^{13}F_n = {}^{13}F_{n,c3} \cdot \beta + {}^{13}F_{n,c4} \cdot (1 - \beta), \tag{3.5}$$

$$^{12}F_n = {}^{12}F_{n,c3} \cdot \beta + {}^{12}F_{n,c4} \cdot (1 - \beta). \tag{3.6}$$

To diagnose monthly or daily averages of the total discrimination, Δ must be an assimilation-weighted average since discrimination at night when photosynthesis does not occur is biologically implausible. Therefore, over t-timesteps, we compute for each land point:

$$\Delta_{month} = \frac{\sum\limits^t \Delta_t \cdot F_{a,t}}{\sum\limits^t F_{a,t}}. \tag{3.7}$$

3.2.3 Disequilibrium flux

A so-called disequilibrium flux exists because of a long-term draw down of the atmospheric $^{13}C/^{12}C$ ratio due to fossil fuel emissions of isotopically light CO_2 [e.g., *Francey et al.*, 1999]. Older carbon that is released to the atmosphere is richer in ^{13}C compared to the carbon that is currently taken up by the oceans and land. For the terrestrial biosphere, this isotopic difference is designated as the isodisequilibrium forcing coefficient [*Alden et al.*, 2010], and can be defined separately for biological respiration $I_{la} = \delta_v - \delta_v^{eq}$ and for biomass burning $I_{fire} = \delta_{fire} - \delta_v^{eq}$ as shown in Chapter 2. These isotopic differences are scaled by large gross fluxes from land-to-atmosphere: F_{la} for biological respiration and F_{fire} for biomass burning.

The total isotopic disequilibrium flux from the terrestrial biosphere D_{bio} is defined as

$$\begin{aligned} D_{bio} &= F_{la} [\delta_v - \delta_v^{eq}] + F_{fire} [\delta_{fire} - \delta_v^{eq}] \\ &= F_{la} I_{la} + F_{fire} I_{fire}. \end{aligned} \tag{3.8}$$

where the fluxes F_{la} and F_{fire} are given in μmol m^{-2} s^{-1} for each grid cell. Monthly isotopic signatures associated with respiration (δ_{v}), biomass burning (δ_{fire}), and uptake ($\delta_{\text{v}}^{\text{eq}}$) are determined using Equation 1.2, i.e.:

$$\delta_{\text{v}} = 1000 \times \left(\frac{^{13}F_{\text{la}}/^{12}F_{\text{la}}}{R_{\text{ref}}} - 1 \right) \tag{3.9}$$

$$\delta_{\text{fire}} = 1000 \times \left(\frac{^{13}F_{\text{fire}}/^{12}F_{\text{fire}}}{R_{\text{ref}}} - 1 \right) \tag{3.10}$$

$$\delta_{\text{v}}^{\text{eq}} = 1000 \times \left(\frac{^{13}F_{\text{al}}/^{12}F_{\text{al}}}{R_{\text{ref}}} - 1 \right) \tag{3.11}$$

3.2.4   Biomass fire scheme

We introduce fire combustion of total carbon and ^{13}C in SiBCASA, based on the work of *van der Werf et al.* [2003 and 2010]. Our calculated fire emissions are driven by multiple remotely sensed burned area products combined in the Global Fire Emissions Database (GFED) [*Giglio et al.*, 2010]. The burned area is given in hectares per month and spans the time period from July 1996 through the end of 2011. Most of the burned area is estimated using Moderate Resolution Imaging Spectroradiometer (MODIS) surface reflectance imagery. The data set is extended prior to MODIS with fire observations from the Tropical Rainfall Measuring Mission (TRMM) Visible and Infrared Scanner (VIRS) and Along-Track Scanning Radiometer (ATSR). GFED burned area is aggregated from a 0.5 $\times$ 0.5 degree grid to a total of 14,538 1 $\times$ 1 degree SiBCASA landpoints to match the resolution of our model. The burned area is then transformed to a scaling factor A by dividing the burned area (BA) with the area (GA) of each grid cell and the number of seconds per month (S):

$$A = \frac{BA}{GA \cdot S}. \tag{3.12}$$

The burning rate A [s^{-1}], together with the tree mortality M (fraction that relates to the density of trees in a biome), carbon stocks C, and pool-dependent combustion completeness factors E (the fraction of biomass available for combustion for each pool

TABLE 3.1: Combustion completeness fractions for different biomes and carbon pools. The tree mortality fraction is given in the end column. Both quantities represent the biome mean values. CWD stands for coarse woody debris, and surfmet, surfstr, and surfmic stand for surface metabolic, surface structural, and surface microbial, respectively.

biomes	storage	leaf	wood	CWD	surfmet	surfstr	surfmic	mortality
tropical forests	0.9	0.9	0.5	0.2	0.9	0.9	0.9	0.9
deciduous forests	0.8	0.8	0.2	0.4	0.8	0.8	0.8	0.6
mixed deciduous forests	0.8	0.8	0.2	0.4	0.8	0.8	0.8	0.6
taiga forest, boreal forest	0.8	0.8	0.2	0.4	0.8	0.8	0.8	0.6
mixed taiga forest, boreal forest	0.8	0.8	0.2	0.4	0.8	0.8	0.8	0.6
mixed trees and grasslands	0.9	0.9	0.3	0.5	0.9	0.9	0.9	0.05
pure grasslands	0.9	0.9	0.3	0.9	0.9	0.9	0.9	0.01
dry grasslands	0.9	0.9	0.3	0.9	0.9	0.9	0.9	0.01
tundra	0.8	0.8	0.2	0.4	0.8	0.8	0.8	0.6
desert	0.9	0.9	0.3	0.9	0.9	0.9	0.9	0.01
agriculture	0.9	0.9	0.3	0.9	0.9	0.9	0.9	0.01

p) determine the combustion flux of total carbon and ^{13}C:

$$F_{\text{fire}} = A \cdot M \sum^{\text{p}} C_{\text{p}} \cdot E_{\text{p}}, \tag{3.13}$$

$$^{13}F_{\text{fire}} = A \cdot M \sum^{\text{p}} {}^{13}C_{\text{p}} \cdot E_{\text{p}}, \tag{3.14}$$

where F_{fire} and $^{13}F_{\text{fire}}$ represent the fire fluxes per grid cell per timestep (given in µmol $m^{-2} s^{-1}$) summed over the p-number of above ground and fine litter pools. Values for E and M are given in Table 3.1. The carbon flow chart for fires is given in Figure 3.1b. We assume that only above ground biomass and fine litter on the surface are directly affected by fires. Part of the carbon that is not combusted is regarded as dead biomass and is subsequently transferred from the above ground to the fine litter pools. The uncombusted carbon in fine litter pools is not transferred further. Peat burning [*Page et al.*, 2002] and organic soil carbon combustion in the boreal region are neglected and we made no distinction between ground fires and crown fires. In this study we used the burned area product from GFEDv3, but confirmed that discrepancies with newer GFEDv4 burned areas are small.

3.2.5 Experimental setup

We performed global runs of SiBCASA from 1851 to 2009. At the start of the simulation we assumed an approximate steady state in the carbon and ^{13}C pools (NEE $\approx$ 0), which

is an assumption often made for biogeochemical models as observations of biomass are not available from that era [*Schaefer et al.*, 2008]. Actual driver data (meteorology, NDVI, burned area) was used for the 1997–2009 period. Prior to 1997, SiBCASA was driven using randomly ordered input fields from our 13-year input database, to ensure that meteorology, NDVI, and burned area came from the same year and month and were thus internally consistent. That meant that any variability from long-term climate change effects, such as a rise in global temperature, were not included in these model spin-up periods. The monthly δ_a observational record spans the simulation period, therefore, SiBCASA had realistic atmospheric δ_a values, facilitating temporal simulation of the disequilibrium between biosphere and atmosphere (note that climate imposed changes are not accounted for). The monthly record is based on ice-core measurements [*Francey et al.*, 1999], and from 1989 onwards atmospheric observations are used. For historical changes in atmospheric CO_2 concentration, we fited a curve to observed global CO_2 concentrations (ice-core data) from the Taylor Dome [*Indermuhle et al.*, 1999] and the Globalview data products [*Masarie and Tans*, 1995].

Two different global simulations were performed using SiBCASA: (1) the ISOVAR simulation (we use the same designation as *Scholze et al.*, 2003 and 2008; *van der Velde et al.*, 2013) including the dynamic discrimination scheme, and (2) the ISOVAR simulation without fire fluxes (ISOVAR-NF, *No Fires*). In ISOVAR-NF the total CO_2 exchange is near equivalent to ISOVAR as the excluded fire disturbances are compensated by increased respiration. All simulations included the same prescribed records of atmospheric CO_2 and δ_a, the same C_3/C_4 distribution, and the same SiBCASA climate driver files as described above. Results from CASA-GFED3 [*van der Werf et al.*, 2010] are provided for comparative purposes. From this point forward, SiBCASA refers to SiBCASA-ISOVAR, unless specified otherwise.

In the second half of this study we used four model simulations to investigate the isotopic signal in local respiration: (1) SiBCASA with the single storage pool, (2) SiBCASA with the separate sugar and starch storage pool, (3) SiBCASA with a modified soil moisture stress function, and (4) SiBCASA with a modified humidity stress function. For our simulations we chose grid boxes in Oregon and Sweden that are similar to the locations of the two measurement experiments.

3.3 Results

3.3.1 ^{13}C signatures in atmosphere-land exchange

Large spatial differences in the global annual plant discrimination (assimilation-weighted) were determined by the C_3/C_4 plant distribution (Figure 3.2a). Regions with lower values of discrimination corresponded to the dominant presence of C_4 plants, such as the South American grasslands, African subtropical savannas, Northern Australia, and North American crop fields. Smaller differences in discrimination within C_3 dominant areas were caused by climate conditions, water availability, and relative humidity. These parameters affected the stomatal conductance, and consequently controlled Δ in Equation 3.1 through changes in the ratios of CO_2 concentration in the ambient atmosphere and intercellular space. The response in discrimination to humidity is further explored in Section 3.3.3.

The global average C_3 discrimination varied for the period 1997–2008 with 19 ± 0.15 ‰ year-to-year (Figure 3.2b). Most of this interannual variability (IAV) originated from the mid- and higher-latitudes and can be attributed to variations in precipitation and relative humidity as identified by *Suits et al.* [2005]. Over the tropical latitudes the IAV was generally very small. Larger excursions were realized in mixed C_3 and C_4 grid cells in the South American and African subtropics. Shifts in the magnitude of GPP in C_3 and C_4 dominated cells affected the annual mean discrimination values.

The global annual total discrimination and IAV (assimilation-weighted) was 15.2 ± 0.04 ‰ (linear detrended and averaged for the period 1997–2008), and is comparable to similar studies (*Lloyd and Farquhar*, 1994: 14.8‰; *Fung et al.*, 1997: 15.7‰; *Suits et al.*, 2005: 15.9‰), as shown in Table 3.2. The level of agreement is lower when compared to *Kaplan et al.* [2002] and *Scholze et al.* [2003]. They reported values of 18.1 and 17.7‰ respectively, as they assigned 15 % and 10 % of GPP to the less discriminating C_4 plants. In contrast, our model assigns around 30 % of GPP to C_4 plants. These differences depend mainly on the vegetation database used, as a large part of year-to-year changes in global discrimination are driven by shifts in C_3 and C_4 productivity. The C_3/C_4 distribution database [*Still et al.*, 2003] used in this study includes additional information on C_4 coverage from crop fraction maps [*Ramankutty and Foley*, 1998] and data on crops from the *Food and Agriculture Organization*.
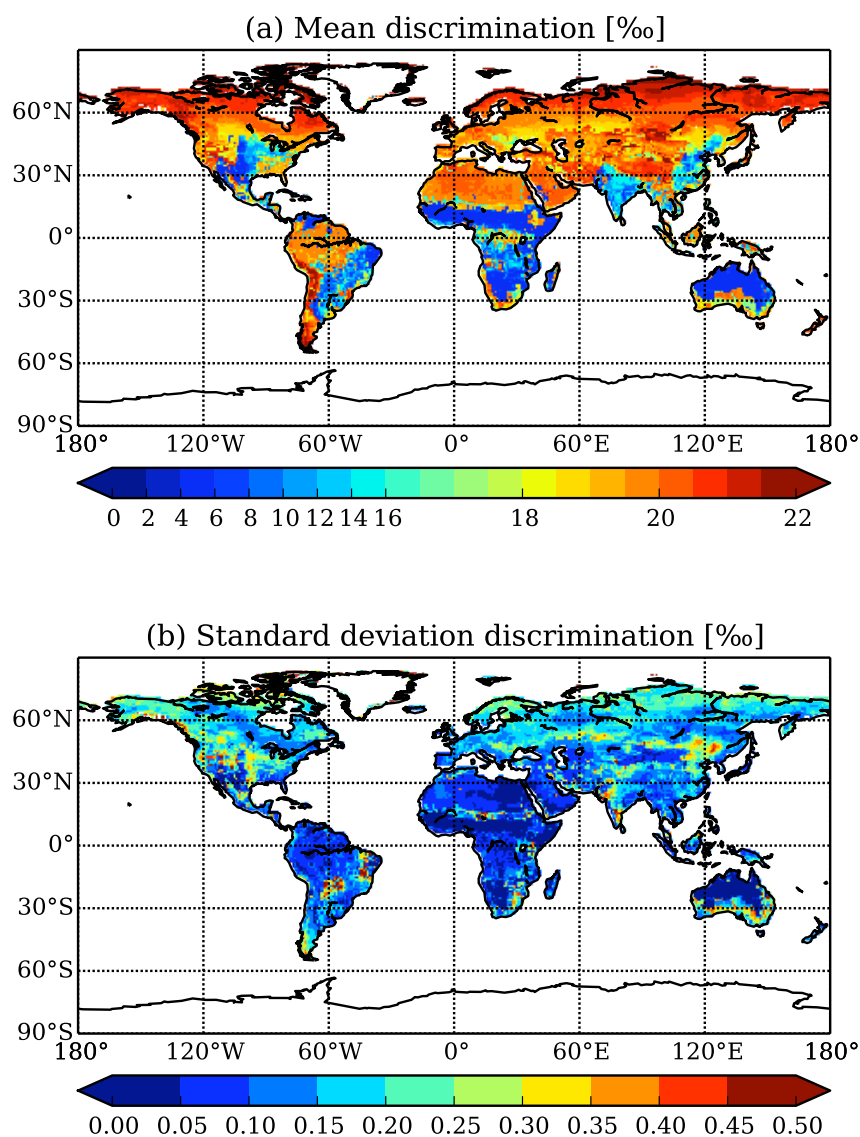
FIGURE 3.2: SiBCASA-ISOVAR assimilation-weighted annual plant discrimination
(a), from a 13 year period (1997–2009), and the year-to-year variability (1σ) of the
annual discrimination values determined from the same 13 year period (b). Differences
in C_3 and C_4 metabolic pathways produce the clear spatial contrast in the annual
mean discrimination. Variations in grid cell average discrimination are largely driven
by RH, precipitation, and soil moisture conditions. The largest standard deviations
are found in parts of South America and Africa in mixed C_3/C_4 grid cells, where
independent changes in C_3 or C_4 GPP can change the grid cell mean discrimination
value significantly. Note that the color scale in (a) is non-linear.

TABLE 3.2: Comparison of isotopic parameters between different modeling studies. The heterotrophic-weighted mean isodisequilibrium coefficient was estimated for the period 1987/88.

	fraction C_4 GPP [%]	C_3 Δ [‰]	C_4 Δ [‰]	net Δ [‰]	Isodis. coeff. (1987/1988) [‰]	D_{bio} (1987/1988) [Pg C ‰ yr^{-1}]
Lloyd and Farquhar [1994]	21	17.8	3.6	14.8	n/a	n/a
Francey et al., [1995]	n/a	n/a	n/a	18.0	0.43	25.8
Fung et al., [1997]	27	20.0	4.4	15.7	0.33	n/a
Joos and Bruno [1998]	n/a	n/a	n/a	18.7	0.43	26.4
Kaplan et al., [2002]	15	20.0	3 to 4	18.1	n/a	n/a
Scholze et al., [2003 & 2008]	less than 10	10 to 23	3 to 4	17.7	0.42–0.59	23.8–41.8
Suits et al., [2005]	24	19.2	4.4	15.9	n/a	n/a
SiBCASA (this study)	30	19-20	4.4	15.2	0.42	21.2

3.3.2 ^{13}C signatures in land-atmosphere exchange

Two aspects of land to atmosphere exchange were further analyzed: (1) biomass burning and (2) disequilibrium.

Biomass burning

Fire emissions estimates in both SiBCASA and CASA-GFED3 were based on burned area maps; thus, although there were discrepancies in predicted emissions per unit area burned, their spatial patterns were quite similar. As displayed in Figure 3.3a, most of the burned area covered Africa and North Australia in regions dominated by savanna grasses. Nonetheless, because of their relatively low fuel loads, the actual carbon emissions (Figure 3.3b) from these regions were low per unit area burned. Over the period 1997–2009 Australia accounted for 14 % of the total burned area, but only contributed 4 % to the total fire emissions. Tropical Asia (defined as a TransCom region as in *Gurney et al.* 2002) accounted for just 2 % of the total burned area but emitted 13 % of the total global fire emissions. This was mainly due to high fuel loads in the form of aboveground wood biomass. Africa was by far the largest contributor, both in terms of emissions (53 %) and burned area (70 %), and the total amounted to 2.55 million km^2 yr^{-1} of burned area (averaged over 1997 through 2009).

The annual mean and IAV of the global fire flux for the period 1997–2009 was 1.93 ± 0.40 Pg C yr^{-1}, which was only 0.07 Pg C yr^{-1} smaller than reported by CASA-GFED3 [*van der Werf et al.*, 2010]. As displayed in Figure 3.4 the global trend and significant IAV in SiBCASA fire emissions were consistent with CASA-GFED3. Both models produced the same temporal distribution of strong and weak fire emissions. For instance, large emissions occurred in 1997 and 1998, followed by smaller emissions after 1998. SiBCASA
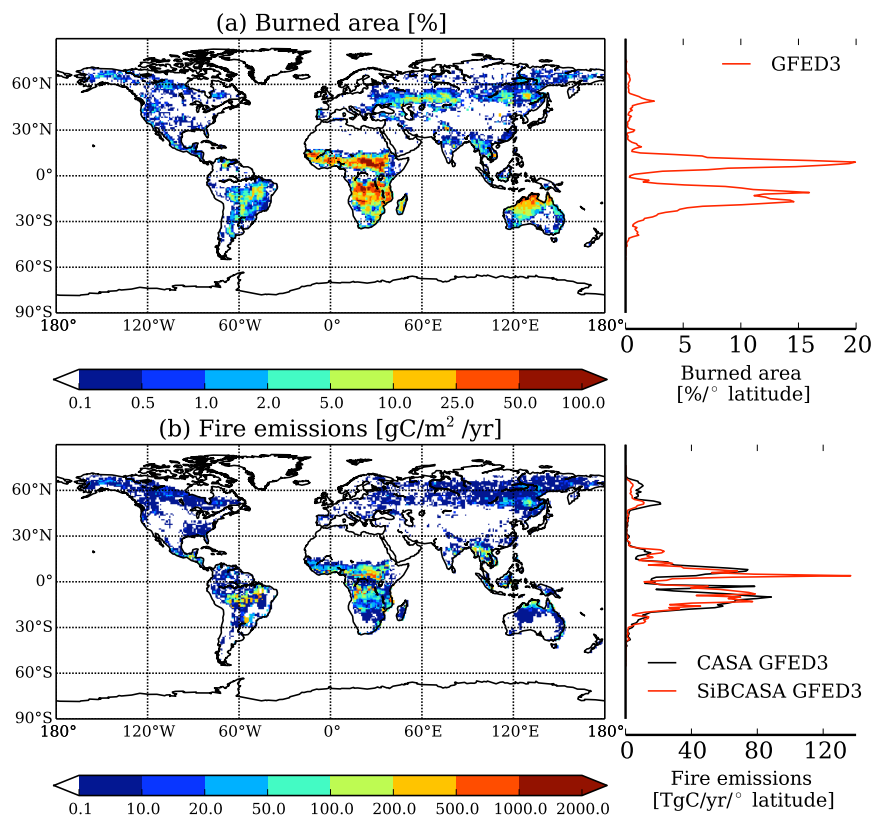
FIGURE 3.3: The (a) annual burned area [% per grid cell from GFED3] and (b) SiB-CASA's fire emissions [gC m^{-2} yr^{-1}] averaged over 1997–2009. The color scales in both panels are non-linear. The panels on the right-hand side display the zonal averages of burned area and fire emissions per degree latitude, respectively. Fire emissions are the product of burned area and amount of standing biomass (fuel consumption). SiB-CASA neglects emissions from organic soils and this explains the underestimation in the Northern Hemisphere (compared to CASA-GFED3).

also produced the same general regional characteristics and seasonal and interannual variability as CASA-GFED3. For instance, Eurasian Boreal fluxes were more than twice as large as North American Boreal fluxes as they cover a larger ground area. Globally, 2001 and 2009 were consistently the years with the lowest emissions (1.5 Pg C yr^{-1}). Some of the year-to-year differences in the annual fire emissions stemmed from the lack of specific combustion processes in SiBCASA (see the Methodology Section, primarily peat and organic soil combustion). Specifically, SiBCASA underestimated (relative to CASA-GFED3) the global emissions in 1997, 2002, and 2006 by 0.1–0.3 Pg C yr^{-1}, although there was good agreement in other years. For example, some burning events were missed in Tropical Asia in 1997, 2002, and 2006 due to the lack of peat combustion in our framework. In the North American Boreal, Eurasian Boreal, and Eurasian Temperate regions the emissions were approximately 50 % smaller than estimated by CASA-GFED3 due to lack of organic soil combustion. This is also visible in the zonal mean profile in Figure 3.3b. This does not result in a marked effect on the global flux as these regions contribute little to total emissions. In Tropical and Temperate South
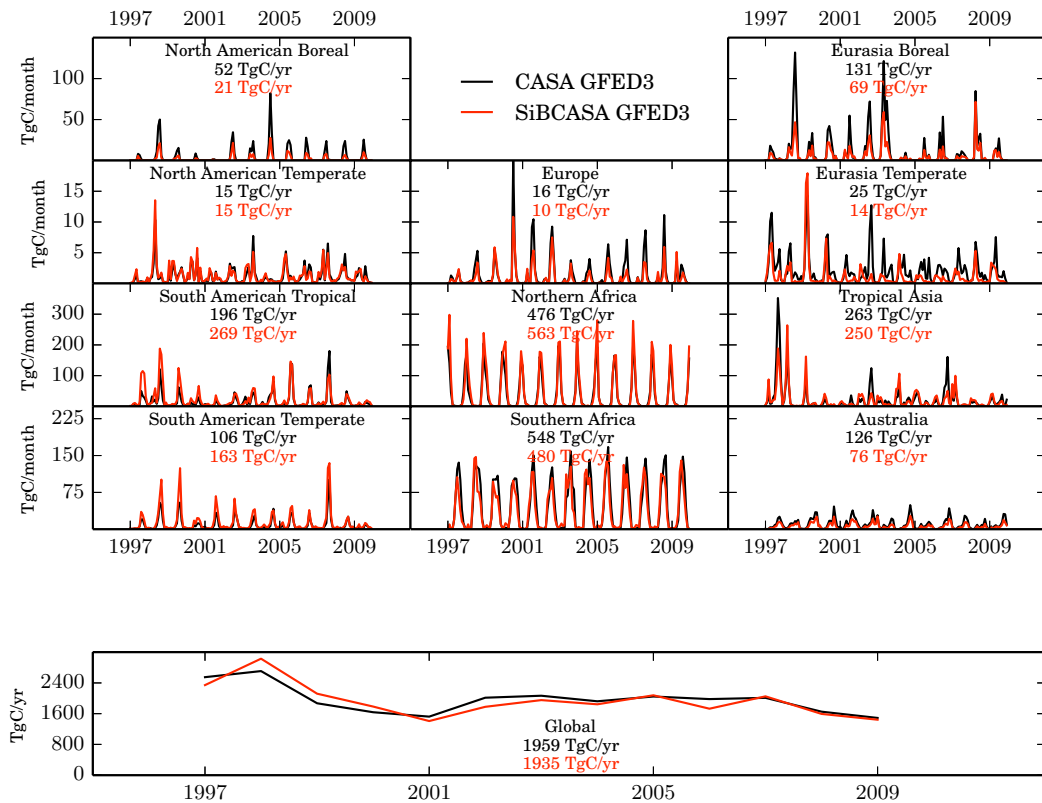
FIGURE 3.4: Monthly fire emissions [$Tg\,C\,month^{-1}$] over 1997–2009 for 11 different TransCom regions. CASA-GFED3 (black) is compared to SiBCASA-GFED3 (red) estimates. Multi-year averages for each region are given as values in $Tg\,C\,yr^{-1}$. Global annual fire emissions [$Tg\,C\,yr^{-1}$] for both simulations are displayed in the separate panel below.

America fire emissions were higher throughout the simulation relative to CASA-GFED3. This is a consequence of larger fuel loads in SiBCASA in comparison to CASA-GFED3, and differences between the coarse biome map and the remotely sensed burned area. These burned area fields are aggregated from 0.5×0.5 degree resolution to a coarser 1×1 degree resolution. At the boundaries between biome types, e.g., tropical forests (high fuel load) and savannas (low fuel loads), this can give a skewed emission because part of the burned area is wrongly assigned to another biome with different simulated biomass. This is apparent close to the equator where we observe a spike of emissions in the zonal mean profile in Figure 3.3b. Other minor differences between the flux estimates presented here and those reported in *van der Werf et al.* [2010] stem from SiBCASA's more simplified representation of the fire parameters. For instance, we used a biome specific fixed combustion completeness factor rather than a variable one [*van Leeuwen et al.*, 2013].

Disequilibrium

The isodisequilibrium coefficient I_{bio} (combined weighted mean of I_{la} and I_{fire}) was highly variable in space. Figure 3.5a displays the map of the global annual ISOVAR disequilibrium, averaged for the period 1997–2008. Generally, the values of I_{bio} were high in regions where the carbon turnover times were long, such as forests and tundra. The largest values of 0.5 ‰ corresponded to boreal regions such as those found in North America and Eurasia. The lowest values of I_{bio} were found in regions covered with herbaceous vegetation, such as in the African savanna. Differences in residence times were the result of variations in plant types, respiration, and fire disturbances. Large disequilibria were mostly found in wood, which has the longest above ground turnover time (30–50 years). There are no trees in tundra, but the soil carbon is frozen most of the year, which resulted in an effective turnover time of up to 1500 years. In our study, the total respiration carries the mean signature of old and new carbon. If we based I_{bio} solely on heterotrophic respiration, as done in other studies listed in Table 3.2, its value would roughly double. This is because the δ signature of heterotrophic respiration (half the magnitude of total respiration) represents an older biomass and is thus heavier in ^{13}C than total respiration, which also includes autotrophic respiration with a δ signature that is much closer to the current assimilation signature. In 1988 (to aid in the comparison with other studies), the global heterotrophic-weighted mean I_{bio} was estimated at 0.42 ‰. This is in good agreement with alternative studies as summarized in Table 3.2.

Next we analyze the simulated disequilibrium flux D_{bio}, which in contrast to I_{bio} directly influences the atmospheric ^{13}C budget. D_{bio} is controlled by both the respiration flux and I_{bio}, which is an integrated parameter of the carbon residence time of the different carbon stocks (see Equation 3.8). The spatial magnitude of D_{bio} (Figure 3.5b) was also clearly different from that of I_{bio} (Figure 3.5a). Tropical forests were responsible for 40 % of the total disequilibrium flux. This was a combined effect of a large respiration flux (32 % of global respiration) and a relatively long pool turnover (D_{tropics} = 10.4 Pg C ‰ yr^{-1} and I_{tropics} =0.27‰). Around 95 % of this disequilibrium flux originated from heterotrophic respiration with the remainder from biomass burning. Boreal forest soils are generally older and thus heavier in ^{13}C, but they accounted for only 11 % of the total disequilibrium flux (D_{boreal} = 2.8 Pg C ‰ yr^{-1} and I_{boreal} =0.38 ‰) as productivity, and thus respiration, were much smaller. The isotopic impact of boreal regions on the atmosphere is therefore estimated to be approximately four times smaller than the impact of tropical regions. Dry areas with a small amount of biomass, such as the American grasslands, African savannas, parts of India and Australia, contributed little to the total disequilibrium flux.

(a) Mean disequilibrium

(b) Mean disequilibrium flux
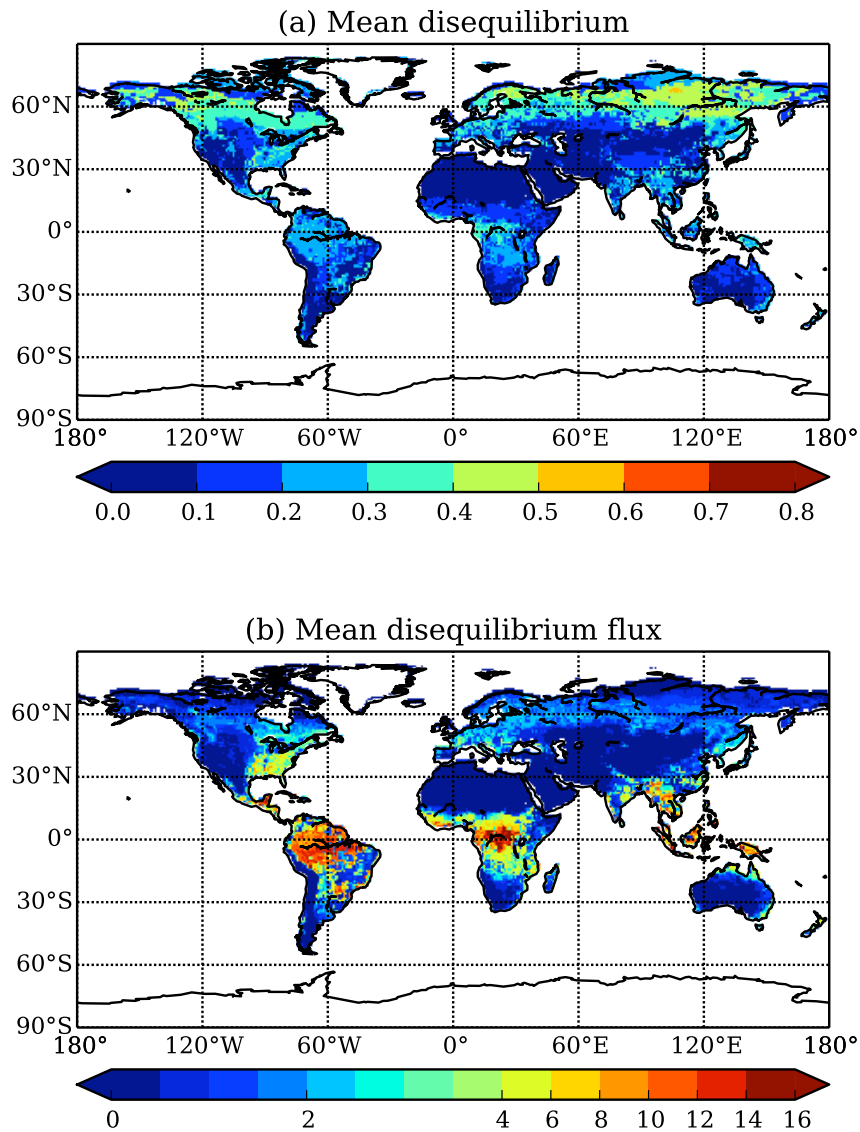
FIGURE 3.5: The (a) SiBCASA-ISOVAR isodisequilibrium coefficient [‰] and (b) disequilibrium flux [Tg C ‰ cell^{-1} yr^{-1}], averaged for a 12 year period (1997–2008). Note that the color scale in panel (b) is nonlinear.

As shown in Figure 3.6, from 1950 onwards, the atmospheric isotopic composition depleted rapidly in ^{13}C due to intensified emissions of isotopically light CO_2 from fossil fuel combustion. As a response to this depletion, the disequilibrium increased rapidly from $0\,\mathrm{Pg\,C\,‰\,yr^{-1}}$ in 1950 to $30\,\mathrm{Pg\,C\,‰\,yr^{-1}}$ at the end of the simulation. The extra variability in δ_a after 1989 is from the increase in available flask measurements. Between 1997–2008, our two SiBCASA simulations had the following mean values and IAV (from the linear trend): ISOVAR; $25.8 \pm 1.5\,\mathrm{Pg\,C\,‰\,yr^{-1}}$ and ISOVAR-NF; $27.4 \pm 1.4\,\mathrm{Pg\,C\,‰\,yr^{-1}}$. The ISOVAR-NF experiment (without fire disturbances) can generally resolve larger values for D_{bio} than the ISOVAR experiment. It confirmed that biomass burning shortens
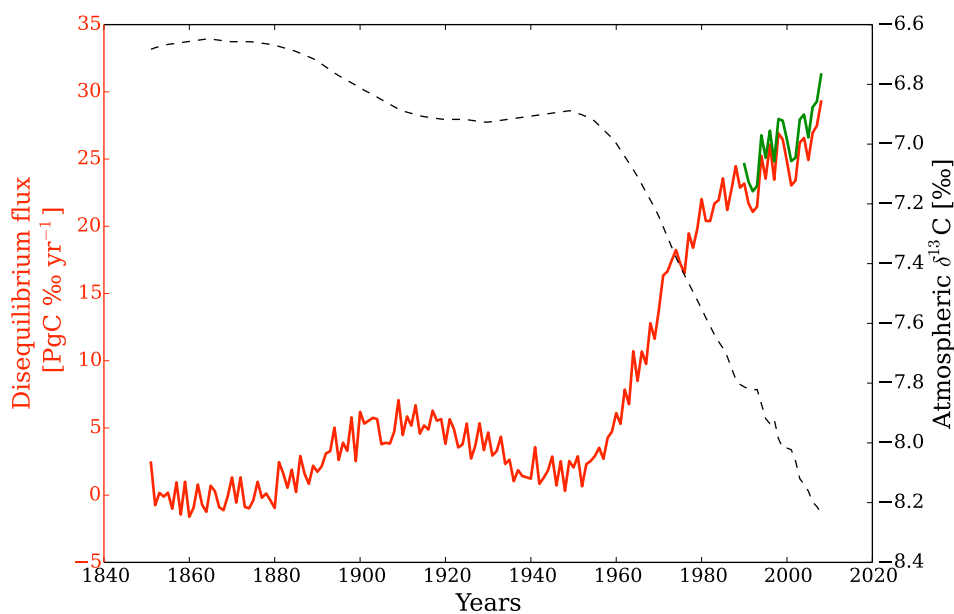
FIGURE 3.6: Time-series (1851–2008) of global annual disequilibrium flux for two differ-
ent experiments: ISOVAR (red) and ISOVAR-NF (green). The ISOVAR-NF simulation
is shown only for the period 1990–2008. Disequilibrium is strongly linked with atmo-
spheric isotopic composition, therefore, δ_a (dashed) is shown on a secondary y-axis.

the turnover times of the biogeochemical pools, which results in a smaller disequilib-
rium flux than if the turnover is determined by natural processes alone, such as decay of
biomass.

3.3.3   Model evaluation with observations

Evaluation of SiBCASA with observations is separated into two parts: (1) ^{13}C composi-
tion in respiration, (2) the role of pool turnover and humidity responses on discrimination.

^{13}C respiration signature

To evaluate our model we used the Biosphere-Atmosphere Stable Isotope Network [BASIN;
Pataki et al., 2003]. BASIN serves as an archive that uses a common framework for the
collection and interpretation of isotopic signatures in CO_2 respiration (δ_r) from Keeling
plot intercept data across sites in North and South America.

Simulated δ_r values compared well with mean observed δ_r values, as shown in Figure 3.7.
The vegetation of most of the sites presented here is C_3, resulting in a cluster of val-
ues with a respiration signature between -23 and $-28\,‰$. The vegetation at the site
in Kansas is predominately C_4 tallgrass prairie, which explains the low value of around
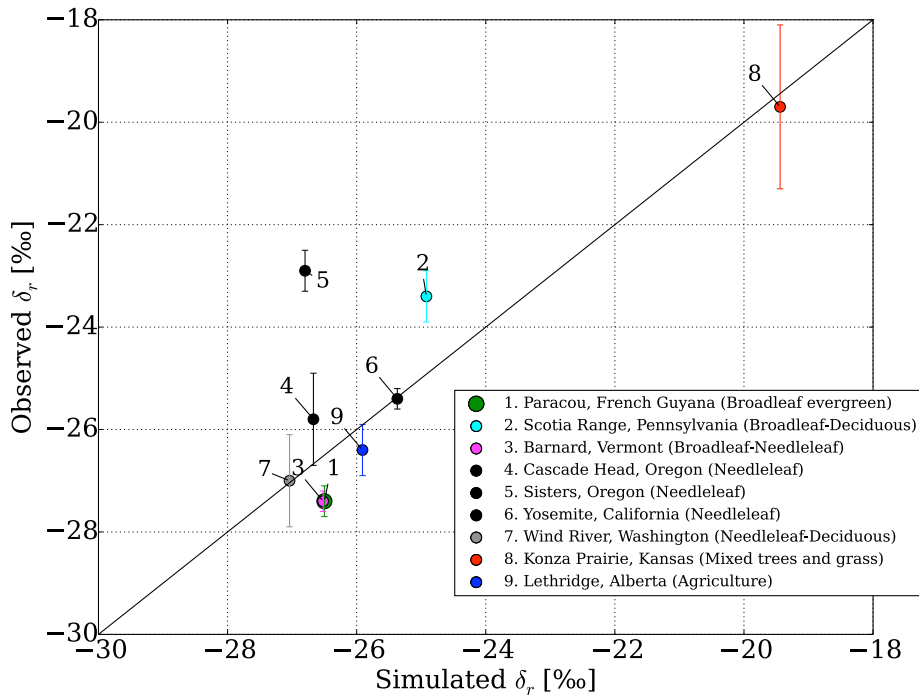
FIGURE 3.7: Measured and modeled signatures of respiration at 9 different sites in North and South America. Measurements for spring and summer months for the 1980s and 1990s were provided by the BASIN network [*Pataki et al.*, 2003]. Each reported value in the figure represents the mean ($\pm 1\sigma$ standard error) over a number of separate measurements from each particular site, and each simulated value was averaged over the same measurement period. Sites are color coded according to their biome type.

$-20\,‰$. We capture similar signatures in our model, which confirms that there is agreement between actual plant use and the C_4 distribution map from *Still et al.* [2003]. There are, however, differences between modeled and measurement values. For example, the simulated respiration signature in the tropical forest site is greater than observed. And for Sisters, Oregon, we see the opposite; the simulated respiration signature is far smaller (more negative) than observed. A possible explanation is that the carbon age or the fraction of soil respiration is misrepresented in the model. In other words, carbon respired from the soils in SiBCASA could be older or younger than what is measured, and thus substantially more enriched or depleted in ^{13}C as a consequence of the Suess effect. However, it is also possible that external variabilities were missed in our model, specifically in monthly precipitation, relative humidity, and soil moisture stress. Such environmental conditions can cause more abrupt changes in the respiration signature than currently modeled in SiBCASA. In the next section we investigate this response in more detail for two different locations with measured humidity–^{13}C relationships.

Turnover and humidity response

Several historical datasets show that C_3 plant discrimination depends strongly on short-term changes in environmental conditions [e.g., *Bowling et al.*, 2002, *Ehleringer and Cook*, 1998, *Ekblad and Högberg*, 2001, *Ometto et al.*, 2002]. Atmospheric humidity and soil water stress are considered important factors that determine stomatal induced variations in isotopic discrimination. Measurements suggest that it only takes a few days for carbon that is assimilated through photosynthesis to become available again for respiration.

We compared the modeled assimilation-weighted discrimination and the isotopic composition in respiration (δ_r) of our study with correlation fits obtained in measurements by *Ekblad and Högberg* [2001] and *Bowling et al.* [2002]. *Ekblad and Högberg* measured soil respiration in a boreal forest in northern Sweden and found a strong linear correlation between sampled humidity and the isotopic composition in CO_2 respiration measured 1 to 4 days later. Their study suggested that the majority of variation in δ_r was caused by respiration of new photosynthate transferred from the canopy by roots, and by mycorrhizal fungi, and rhizosphere heterotrophs. *Bowling et al.* calculated Keeling plot intercepts at four different locations in Oregon. They also found a strong relationship between the 5 to 10 day lagged δ_r in ecosystem respiration and vapor pressure deficit (VPD). They also suggested that variation in discrimination based on water availability is an important source for this behavior. Henceforth, when we refer to these observations we name them by their geographical location: *Sweden* and *Oregon*. *Suits et al.* [2005] compared SiB's assimilated isotopic signatures with these correlation fits and evaluated the relationship between humidity and discrimination. Given that our framework included the complete exchange of ^{13}C we were able to expand this analysis with the actual modeled δ_r.

Figure 3.8a and b show the time series of VPD and discrimination for the single storage pool simulation for a site in Oregon. Day-to-day changes in VPD (Figure 3.8a) affected the discrimination almost immediately (Figure 3.8b). Discrimination is strongly coupled to CO_2 and water diffusion gradients, which means that smaller VPD gives larger discrimination and vice versa. The relationship between VPD and discrimination is further illustrated in Figure 3.9a for simulations at Oregon (blue dots) and Sweden (red dots) in comparison to the approximate curve fits based on measurements (dashed lines). Note that the observed relationships in Figure 3.9a are an approximation for discrimination, as discrimination was not actually measured; the fitted lines were derived from the respiration signature fit functions shown in Figure 3.9b, given the current atmospheric isotopic composition δ_a. Modeled discrimination values were in between the two observed relationships, but the general pattern for both locations was more or less the same: small VPD (high RH) gives larger stomatal conductance, and thus larger discrimination. The
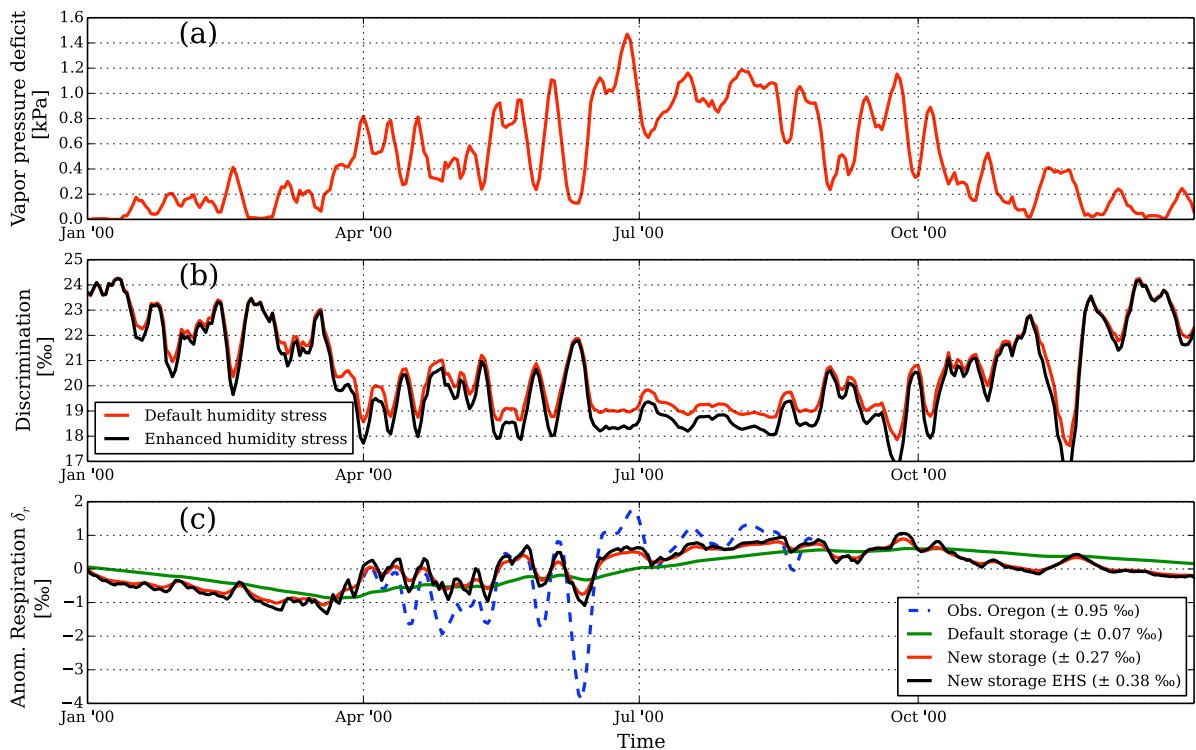
FIGURE 3.8: Daily vapor pressure deficit (a), isotopic discrimination (b), and anomalies relative to the mean in the isotopic signature in autotrophic respiration (c) for the year 2000 simulated in Oregon. Panel (c) depicts the δ_r in respiration from the single storage pool (green line) and the new storage pool structure (red line), and in addition, δ_r predicted with the curve fits estimated from observations in Oregon [*Bowling et al.*, 2002, blue dashed line]. The 1σ (detrended) variability between April and August is shown in the legend. Estimates due to enhanced humidity stress (EHS) are shown in (b) and (c) as a black line.

strong curvature with small VPD, as observed at the Oregon site, is only partially captured in our model. At the larger VPD regimes the modeled discrimination reaches a minimum where the slope becomes almost flat in comparison to the observations.

For autotrophic respiration, the fast changes in VPD are reflected in observed δ_r but are hardly visible in SiBCASA (Figure 3.8c, green line). The inability to capture fast respiring signatures is due to the design of the single storage pool in SiBCASA. Given that only 10 % of the storage is readily available for growth, the effective turnover time of the storage pool is large at approximately 70 days. This dampens any high frequency changes in the isotope ratio of respiration, in contrast to observations. The observed δ_r was derived from the VPD-respiration relationship determined from observations in Oregon [*Bowling et al.*, 2002] and predicts much greater variations (Figure 3.8c, blue dashed line). Note that the strong negative anomaly in δ_r of -4 ‰ (when VPD was smaller than 0.2 kPa) was not actually measured in Oregon.
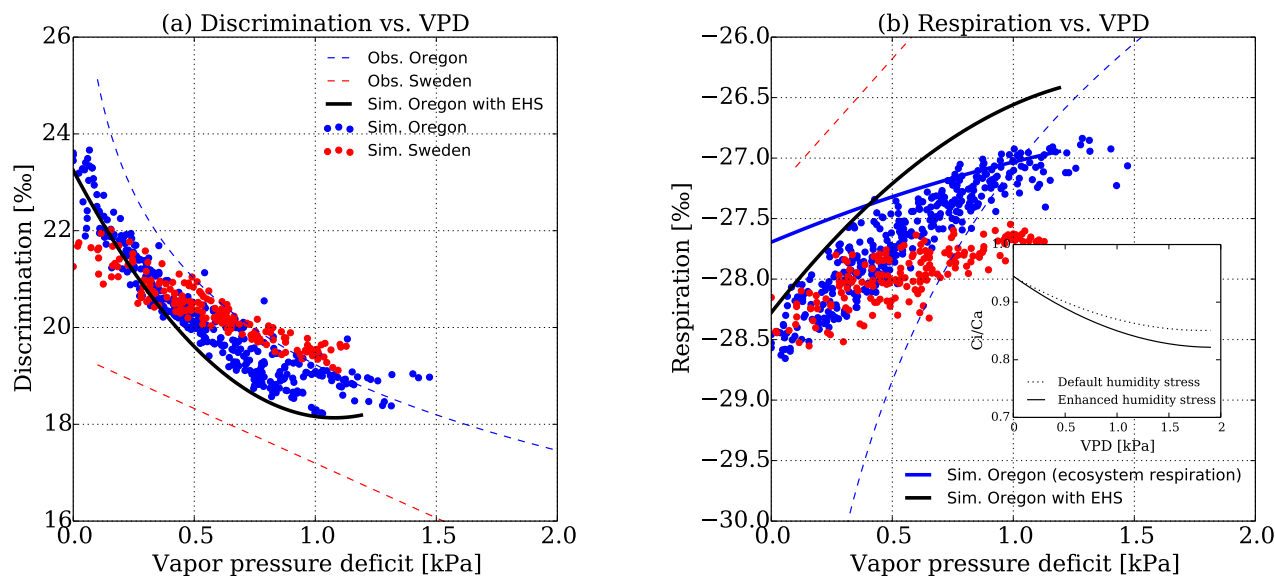
FIGURE 3.9: Modeled plant discrimination [‰] and isotopic signature in respiration [‰] as a function of vapor pressure deficit [VPD, kPa] for two locations: Oregon (blue) and Sweden (red). In (a) discrimination versus VPD. In (b) isotopic signatures in autotrophic respiration (δ_r) versus VPD. Daily mean values are from the SiBCASA-ISOVAR simulation taken during the months when carbon uptake peaked in 2000, 2001, and 2002. Daily mean VPD is derived from daylight hours. In (b) the blue dashed line represents a logarithmic fit to measured δ_r taken from sites in Oregon [*Bowling et al.*, 2002]. The red dashed line represents a linear fit to measured δ_r in a mixed coniferous boreal forest in northern Sweden [*Ekblad and Högberg*, 2001]. In (a) both lines are approximated as plant discrimination using the relationship: $\Delta = \frac{\delta_a - \delta_r}{\delta_r/1000 + 1}$. The solid lines represent curve fits through simulated values at Oregon for ecosystem respiration (blue) and for enhanced humidity stress (black). The insert shows change in the c_i/c_a ratio as a function of VPD due to this additional stress.

The double storage pool modification (see Methodology Section 3.2.1) improved the level of agreement between modeled and observed δ_r. Allowing carbon extraction from the fast sugar pool mimicked the transfer of new photosynthates to leaves, wood, and root pools and introduced variations in δ_r that better matched with the observations from Oregon (Figure 3.8c, red line). The standard deviation (1σ) increased almost 4-fold in comparison to the single storage pool simulation. Even so, the magnitude of the variations was still 3.5 times smaller than for the observed VPD-respiration relationship for Oregon. Nevertheless, a better match is attained using a fit function based on measurements in Sweden (simulated variations would be twice as small; not shown).

The difference between these two measurement-based VPD-respiration relationships is further illustrated Figure 3.9b. If we look at Oregon and Sweden, we found that the fast sugar pool improved the δ_r relationship for both sites (7x slope increase in Sweden and 3x slope increase in Oregon). Despite the improvements, over the whole VPD range,

variations in δ_r were still limited. The new storage pool framework helped to improve the response of δ_r to VPD, however, the amplitude of variations was underestimated.

Changing the soil moisture response curve to increase variability in discrimination had a small effect on the respiration signal. Soil water stress is one of the different components (alongside irradiation, salinity, and temperature) that affects mesophyll conductance and CO_2 diffusion inside the plant. In SiBCASA the soil water stress follows a parabolic function of plant available water. There is no stress near field capacity, but near wilting point there is a steep drop-off. Use of a linear relationship where stress already occurs close to field capacity had only a negligible effect on the discrimination at the sites investigated (not shown).

In a final experiment we enhanced the stomatal resistance of molecular diffusion from the leaf surface towards the stomatal cavity as a function of humidity. This was to mimic a stronger response in discrimination to changes in c_i/c_a (the ratio of CO_2 concentrations in the leaf intercellular spaces to that in the atmosphere) under drier conditions. The c_i/c_a ratio is determined by the balance between photosynthetic demand and the stomatal conductance to limit water loss, i.e., a trade-off quantified as the intrinsic water use efficiency (iWUE). In SiBCASA these mechanisms are strongly constrained by the stomatal conductance model and the generalized coefficients for C_3 and C_4 photosynthetic pathways determined in leaf gas-exchange experiments. In reality c_i/c_a differs more strongly among different plant species, whereas this ratio only differs at the biome-level in SiBCASA. Furthermore, the responses in c_i/c_a will differ among different stomatal conductance formulations. Additional responses in c_i/c_a translate into enhanced changes in discrimination and δ_r. For drier regimes, the outcome of this modification is 3-fold: extra reduction in c_i/c_a, extra reduction in discrimination, and heavier signatures in δ_r as function of VPD (see Figure 3.8b and c, black lines). Moreover, due to these modifications, the VPD-discrimination and respiration relationships as shown in Figure 3.9a and b as black lines have a steeper slope (20 %), improving the agreement with observations in Oregon.

3.4 Discussion and conclusions

In this study we introduced a modified version of SiBCASA to simulate ^{12}C and ^{13}C exchange. The modifications included realistic fire emissions based on remotely sensed burned area, and the exchange of ^{13}C isotopes between atmosphere and plants. A comprehensive set of observations and other model studies were used to assess model performance.

Global isotope discrimination was generally consistent with observations and comparable with similar studies; SiBCASA calculated a global annual discrimination of 15.2‰ between 1997–2008. This value depended strongly on the amount of C_4 photosynthesis prescribed in the model.

Global fire emissions compared well with estimates from the CASA-GFED3 study described in *van der Werf et al.* [2010]. From 1997–2009 we predicted an average flux of 1.93 Pg C yr^{-1}, which is 3.5 % less than reported in the CASA-GFED3 study. On both global and regional scales the trend, the seasonal, and the interannual variability in fire emissions were consistent. The underestimation of fire emissions in Tropical Asia and Boreal regions are expected since our simplified approach does not include specific processes like peat combustion and organic soil combustion. Other smaller discrepancies between SiBCASA and CASA-GFED3 are the result of differences in the amount of biomass and mismatches between the biome type map and the remotely sensed burned area. We anticipate that the addition of processes like peat and organic soil combustion, and the inclusion of time- and space-dependent combustion parameters will improve model performance further.

The global disequilibrium signal is consistent with similar studies. There are some notable differences between our disequilibrium flux and the LPJ simulations presented by *Scholze et al.* [2008]. Firstly, the discrepancy in the disequilibrium flux between their ISOVAR and ISOVAR-NF simulations was much larger (25 %) than in the current study. This is because their estimates of biomass burning are four times larger than ours, which explains the large impact on the disequilibrium flux in their study. They do acknowledge that their global mean value of biomass burning (8 Pg C yr^{-1}) is much larger compared to many other studies [e.g., *van der Werf et al.*, 2003]. The differences in the mean ISOVAR disequilibrium isofluxes between *Scholze et al.* (34.8 Pg C ‰ yr^{-1}) and this study (25.8 Pg C ‰ yr^{-1}) at the end of the simulation period is a consequence of differences in the amount of C_4 plant growth (less than 10 % compared to 30 % in our study) and differences in the resolved heterotrophic respiration fluxes between the two studies (69.4 Pg C yr^{-1} compared to 52.3 Pg C yr^{-1} in our study). With a reasonable estimate of ocean disequilibrium, the magnitude of our terrestrial disequilibrium flux remains too small (approximately 30 %) to close the atmospheric δ_a budget (also see *Langenfels et al.*, 1999), and this remains an outstanding issue in the global carbon balance. To increase the estimates of the global disequilibrium flux we would need a simultaneous decrease in turnover times and increase in carbon pool sizes to enhance respiration, but this needs to be investigated more thoroughly in the future. This is a good example of how ^{13}C in atmospheric CO_2 can eventually help us to constrain multiple processes within a biogeochemical model like SiBCASA.

Another source of uncertainty that is currently not included in the model is land use change, which can have a large impact on the disequilibrium flux [*Scholze et al.*, 2008]. For instance, the gradual increase of low discriminating C_4 plant activity (pastures and crops) caused a reduction of 40 % in the disequilibrium flux compared to their ISOVAR simulation (without cultivation). Our simulations assumed a static C_4 fraction map from *Still et al.* [2003], which is representative of the situation in the 1980s and 1990s. Because of its gradual nature, land use change is not expected to be a large source for variability in disequilibrium. Instead most of the variability comes from year-to-year changes in discrimination and changes in C_3 and C_4 productivity as shown in Chapter 2. We also omitted the mobilization and decay of harvested wood biomass (e.g., furniture). These influences deserve more attention in SiBCASA and will be the subject of future improvements.

Atmospheric humidity appears as an important contributor to the stomatal induced variations in isotopic discrimination and these findings are in agreement with various published measurements [e.g., *Bowling et al.*, 2002, 2014, *Ekblad and Högberg*, 2001]. Humidity affects stomatal conductance, which is reflected in discrimination, and ultimately alters the isotopic content of CO_2 respired back to the atmosphere. In the model we observe the following: (1) a generally weak response in discrimination to changes in VPD, (2) latency in recently assimilated carbon becoming available for respiration, (3) the absence of additional processes that contribute to additional stomatal stress, and (4) the absence of additional isotope effects that contribute to variability in respired CO_2 isotopic composition. We made an important model improvement by separating sugars and starch in the SiBCASA pool configuration. The gradient between the isotopic signature in respiration and humidity as shown in the observational data increased and amplified the variability in δ_r 3 to 7-fold. Nevertheless, variations in respiration were dampened compared to variations in discrimination as a function of humidity. This dampening effect in isotopic response is a consequence of the carbon in the storage pools being transferred back and forth between usable sugars ($\sim$ 7-day turnover) and starch ($\sim$ 60-day turnover) in order to keep the ratio between both pools close to 1:9. It dilutes the isotopic signal from photosynthetic discrimination and this process may in reality be less dominant than currently modeled in SiBCASA. It is likely that the 1:9 constraint is too extreme for the growing season as the ratio of sugar to starch varies strongly over this period. The ratio will be higher at the start of the growing season when plants convert a lot of starch to sugar to grow new leaves. The observed ^{13}C relationships therefore suggest the need for a bigger pool of fast respiring carbon.

Exchanging the simulated autotrophic respiration for ecosystem respiration (autotrophic + heterotrophic) in Figure 3.9b increased the isotope ratios (solid blue slope), as CO_2 of decomposing soil organic matter (SOM) is generally more enriched due to the Suess

effect. Furthermore, we see additional dampening in variability because the decomposing SOM in SiBCASA exhibited very little variability compared to recently fixed photosynthates. This is interesting because the measured relationships in Oregon, which show very strong response to humidity, were determined with Keeling plot intercepts that reflect the ecosystem respiration (thus including SOM decomposition). We assume that important dynamic changes in heterotrophic substrates influencing the isotopic composition of soil respiration are missing. It is also possible that the contribution from SOM decomposition (heterotrophic respiration) was larger in the model than the contribution from SOM respiration during the measurements presented in the literature. Further, the chosen sampling strategies for the Keeling plot method can influence the footprint. Sampling δ_a at different heights can reflect different mixtures of atmospheric CO_2 dominated by either plant respiration or soil respiration [*Pataki et al.*, 2003].

Other discrimination effects after photosynthesis are not implemented in SiBCASA, i.e., when carbon is allocated to the different carbon pools or respired back to the atmosphere. In reality, however, there are numerous additional isotope effects after photosynthetic uptake that affect the isotopic composition of different carbon compounds inside the plant. These are often very complex to model and their response to changes in environmental conditions are not fully understood [*Brüggemann et al.*, 2011]. In addition, no significant discrimination effects were found in respiratory processes [*Lin and Ehleringer*, 1997]. Any other isotope effects will cause variations in the isotopic composition of carbon that is converted into different compounds. These discrimination effects are likely an additional source of variation in the isotope ratios of respiration, but are currently not accounted for in the model.

A steeper gradient (20 %) in the isotopic composition of respiration towards humidity can be achieved with a slightly modified c_i/c_a ratio and iWUE to acquire more variability in discrimination. This modification is not to invalidate the stomatal conductance formulation using isotope measurements. Instead, it investigates what δ_r in respiration would look like if the model responds more strongly to changes in VPD, and explores the possibilities that the response to humidity in stomatal conductance and discrimination might not be strong enough, especially when VPD may become large. It must be pointed out that these changes were only tested for two specific locations. To scale these changes in stomatal conductance and iWUE to a global domain is probably not justified as it is likely that they are only applicable for certain biomes under certain conditions.

This study shows that the isotopic composition of plants can change under the influence of environmental conditions and discrimination processes. To simulate ^{13}C exchange more accurately on shorter time scales, a double storage pool with a fast turnover component is

an important addition to a biogeochemical model. Our results also highlight the importance of ^{13}C to help assess and improve the simulation of biogeochemical processes, such as allocation and turnover of carbon and responses to drought. Measurements suggest that responses to climate anomalies will likely invoke more variability in the assimilation and respiration signatures than we currently model, but indirectly it can also invoke more variability in isotopic disequilibrium. This is important because discrimination and disequilibrium flux play a critical role in the total atmospheric ^{13}C budget and its variability. Our next step focuses on the implementation of the SiBCASA framework (with biomass burning and ^{13}C exchange) with a data-assimilation system to interpret observed signals in atmospheric CO_2 and δ_a to changes in terrestrial exchange and drought response.

Chapter 4

Estimating regional isotope discrimination using CO_2 and $\delta^{13}C$ measurements

Abstract

We developed a multi-tracer inversion system to interpret signals in atmospheric CO_2 and $\delta^{13}C$ observations. As plants experience drought stress, they respond by closing their stomata to prevent loss of water. This process also inhibits uptake of CO_2 and reduces isotope discrimination against $^{13}CO_2$ molecules. As this reduction induces detectable variations in the atmospheric ratio of $^{13}CO_2/^{12}CO_2$ ($\delta^{13}C$), we were able to use inverse modeling to estimate and analyze the discrimination parameter for plants. We found that predicted isotope discrimination values decreased by as much as $2\,\text{\textperthousand}$ under drought conditions in the Northern Hemisphere, and were consistently smaller than estimates from prior estimates. The decrease in discrimination suggested an increase of up to $25\,\%$ in regional intrinsic water-use efficiency. We found that interannual variability in net ecosystem exchange was relatively insensitive to variation in the discrimination parameter, which was allowed to increase more than 8-fold relative to the prior discrimination variability. This study suggests a larger effect of droughts on discrimination than previously thought, and indicates that improvements in the treatment of drought response in biosphere models are required.

4.1   Introduction

Over the last 20 years considerable progress has been made in understanding the global carbon cycle. In particular, measurements of atmospheric CO_2 have been used to infer carbon fluxes at the Earth's surface using a variety of inversion techniques [see e.g., *Alden et al.*, 2010, *Ciais et al.*, 1995, *Rayner et al.*, 2008, *Tans et al.*, 1993]. Unfortunately, a lack of CO_2 observations, errors in atmospheric transport modeling, and the realism of bottom-up carbon flux estimates are limiting the utility of these techniques. These methods often suffer from 'flux leakage', a misallocation of CO_2 uptake from the land biosphere to the oceans, and are often not well suited to study specific processes underlying the carbon exchange. This is mostly because atmospheric CO_2 reflects net ecosystem exchange (NEE), which is a small residual of two much large gross fluxes: gross primary production (GPP) and terrestrial ecosystem respiration (TER). Inference of only the net exchange fluxes therefore results in loss of specific information on variation in photosynthesis and respiration (e.g., due to drought stress). In addition, the uncertainty on estimates of the inferred carbon fluxes is still large. To better understand these specific processes in carbon exchange and reduce estimated carbon flux uncertainties, there is a need to introduce additional observational constraints on the carbon cycle.

In this study, we investigate the use of the rare isotope ^{13}C (in atmospheric CO_2) as an extra tracer to estimate carbon sources and sinks and their variability. On a global scale, ^{13}C can help us distinguish oceanic from terrestrial exchange, as oceans take up $^{13}CO_2$ more efficiently than land surfaces. In so-called double-deconvolution methods this particular property is used to distinguish land carbon uptake from ocean carbon uptake [*Ciais et al.*, 1995, *Keeling et al.*, 1989]. On regional scales variations in the ratio of $^{13}CO_2/^{12}CO_2$ (typically reported as $\delta^{13}C$ relative to a reference ratio) also reflect changes in discrimination processes associated with terrestrial carbon exchange [e.g., *Ciais et al.*, 1995, *Farquhar et al.*, 1989, *Fung et al.*, 1997, *Rayner et al.*, 2008, *Scholze et al.*, 2003]. Plants generally take up the heavier $^{13}CO_2$ molecules less efficiently than $^{12}CO_2$ molecules causing a change in the $^{13}CO_2/^{12}CO_2$ composition in atmosphere. This discrimination against ^{13}C is stronger for C_3 plants than for C_4, but also varies as function of moisture conditions in the atmosphere and soil [*Ekblad and Högberg*, 2001, *Farquhar et al.*, 1980, 1989, *Ometto et al.*, 2002, *Suits et al.*, 2005]. This means that under the right circumstances, measured atmospheric $^{13}CO_2/^{12}CO_2$ ratios can be used to recognize changes in photosynthetic activity resulting from droughts stress [*Ballantyne et al.*, 2010].

Water-use efficiency (WUE) is a measure of the trade-off that plants make to optimize regulation of evaporative water losses and photosynthetic carbon gains. By actively regulating stomatal opening, plants have been able to photosynthesize at a lower transpiration rate during the atmospheric CO_2 increase of the past decades, leading to an

increased WUE. The opening of the leaf stomata is generally sensitive to CO_2 concentration, light, temperature, and humidity [*Mansfield et al.*, 1981, *Meidner and Mansfield*, 1968, *Schulze et al.*, 1987, *Turner*, 1991]. Strong increasing trends in WUE have already been observed in previous studies [*Hietz et al.*, 2005, *Keenan et al.*, 2013, *Saurer et al.*, 2004]. Significant interannual variability (IAV) and regional differences in WUE are evident due to variations in temperature and relative humidity [*Farquhar et al.*, 1989, *Seibt et al.*, 2008]. For instance, the North American summer heat wave of 2002 and the European summer heat wave of 2003 have received considerable attention regarding their effects on ecosystems. These studies reported overall reductions in carbon uptake, in evapotranspiration and different controlling factors on NEE, either from vapor pressure deficit or soil moisture [e.g., *Ciais et al.*, 2005, *Dong et al.*, 2011, *Kwon et al.*, 2008, *Zhang et al.*, 2012].

The WUE, which refers to changes in GPP and stomatal conductance (intrinsic; iWUE), changes $\delta^{13}C$ as photosynthesis discriminates against the heavier $^{13}CO_2$ molecule [*Farquhar et al.*, 1989]. A simplified relation between iWUE and C_3 plant discrimination can be written as follows [based on *Beer et al.*, 2009, *Seibt et al.*, 2008]:

$$\text{iWUE} = \frac{\text{GPP}}{g_s} = \frac{\text{GPP} \cdot \text{VPD}}{\text{ET}} = \frac{c_a - c_i}{1.6}, \tag{4.1a}$$

$$\Delta_{C3} = \Delta_d + (\Delta_p - \Delta_d)\left(\frac{c_i}{c_a}\right) \approx (\delta_a - \delta_v), \tag{4.1b}$$

Substitution of 4.1b in 4.1a gives iWUE as a function of Δ_{C3}:

$$\text{iWUE} = \frac{c_a}{1.6}\frac{(\Delta_p - \Delta_{C3})}{(\Delta_p - \Delta_d)}, \tag{4.1c}$$

where c_a and c_i are the CO_2 partial pressures in the atmosphere and inside the leaf, respectively, VPD is the vapor pressure deficit, g_s is the stomatal conductance to water, ET the transpiration, and Δ_p ($\sim 28\,‰$) and Δ_d ($\sim 4\,‰$) are the isotopic discrimination parameters due to the Rubisco enzyme reaction in C_3 photosynthesis and molecular diffusion of CO_2, respectively. All else remain unchanged, stomatal closure will reduce g_s, GPP, and ET. It also increases the gradient between c_a and c_i leading to a larger iWUE and a smaller discrimination, which determines the ^{13}C composition (in ‰) in vegetation (δ_v) and atmosphere (δ_a). This relationship is also highlighted in Section 1.5 in Equation 1.13.

Different vegetation types employ different strategies over different time scales, therefore there is a wide diversity of observed local WUE responses. An advantage of studying changes in δ_a rather than δ_v is that the atmosphere integrates changes in WUE over large areas, because air masses are transported and mixed rapidly in the turbulent lower

atmosphere. In contrast, measured changes in δ_v in tree rings or eddy-covariance sites reflect local WUE changes.

In this study we used measurements of two atmospheric tracers (CO_2 and $\delta^{13}C$) to explore the use of atmospheric inversion techniques as tools to explain carbon exchange processes at Earth's surface. Scaling (optimization) of net ocean and terrestrial carbon fluxes is relatively common in traditional data-assimilation systems [e.g., *Peters et al.*, 2007, 2010]. To improve the level of agreement between modeled and measured atmospheric $\delta^{13}C$, we also scaled the isotope discrimination parameter Δ_{C3} in the terrestrial biosphere to provide a separate estimation of terrestrial exchange of $^{13}CO_2$ between plant and atmosphere. Our aim was to explore in more detail the regional and daily variations in atmospheric $^{13}CO_2/^{12}CO_2$ ratio resulting from specific plant physiological processes integrated over a larger region. The ability to capture large-scale drought dynamics in fluxes and isotopic discrimination could provide useful information on drought stress in plants and the corresponding changes in stomatal conductance and WUE.

4.2 Methodology

We first present the general understanding of the atmospheric $\delta^{13}C$ budget (Section 4.2.1), before proceeding to describe integration of $\delta^{13}C$ within our new joint inversion framework (Section 4.2.2). We then briefly describe the prior flux and discrimination estimates used, and the observational network (Section 4.2.3). Finally, we give a brief description of the different inversion experiments (Section 4.2.4). Table 4.1 provides a summary of symbol definitions and dimensions.

4.2.1 The atmospheric $\delta^{13}C$ budget

Use of $\delta^{13}C$ observations alongside CO_2 observations could constitute a potentially useful change to the traditional CO_2-only CarbonTracker, as it would provide an additional constraint on carbon surface fluxes and isotope exchange processes in plants. The rationale behind this is that the $^{13}CO_2$ and $^{12}CO_2$ contents in the atmosphere are affected through the same CO_2 pathways from land and ocean surfaces. There are, however, specific processes that change the $^{13}CO_2$ exchange fluxes independently from $^{12}CO_2$ fluxes. We can rewrite the global mass balance for $\delta^{13}C$ (see Equation 1.9) so that the different isotopic processes are explicitly defined and dependent on total CO_2 fluxes [*Tans*

et al., 1993]. We can then identify the (1) emission forcing terms, (2) net exchange discrimination forcing terms, and (3) gross-flux disequilibrium forcing terms:

$$
\begin{aligned}
C_\mathrm{a} \tfrac{\mathrm{d}}{\mathrm{dt}} \delta_\mathrm{a} \;=\; & F_\mathrm{ff}\,(\delta_\mathrm{ff} - \delta_\mathrm{a}) & + \;\; & F_\mathrm{fire}\epsilon_\mathrm{ph} & & \text{[emission forcing terms]} \\
+ \;\; & N_\mathrm{bio}\epsilon_\mathrm{ph} & + \;\; & N_\mathrm{oce}\epsilon_\mathrm{ao} & & \text{[net exchange forcing terms]} \\
+ \;\; & F_\mathrm{la}\,(\delta_\mathrm{v} - \delta_\mathrm{v}^\mathrm{eq}) & + \;\; & F_\mathrm{fire}\,(\delta_\mathrm{fire} - \delta_\mathrm{v}^\mathrm{eq}) & & \text{[terrestrial isodisequilibrium forcing terms]} \\
+ \;\; & F_\mathrm{oa}\,(\delta_\mathrm{a}^\mathrm{eq} - \delta_\mathrm{a}) & & & & \text{[ocean isodisequilibrium forcing term],}
\end{aligned}
$$

$$(4.2)$$

where C_a is the total carbon content in the atmosphere (in the form of CO_2). The subscripts la and oa denote the direction of the one-way gross fluxes, e.g., F_la refers to the respiratory release of CO_2 from land to atmosphere. The isotopic ratios of $^{13}C/^{12}C$ are expressed as δ_xx, where the subscripts refer to the signature in land vegetation and soils (v), in biomass burning flux (fire), or in the fossil fuel emission flux (ff). The signature $\delta_\mathrm{a}^\mathrm{eq}$ depicts the isotopic ratio of CO_2 that is in equilibrium with the ocean surface and $\delta_\mathrm{v}^\mathrm{eq}$ depicts the ratio in the terrestrial biosphere that is in equilibrium with the current atmosphere. N_bio and N_oce refer to net exchange fluxes (gross uptake minus gross release) of CO_2, and F_ff and F_fire are the fossil fuel and biomass burning CO_2 emissions, respectively.

The terrestrial isotopic discrimination effect in Equation 4.2 is expressed as ϵ_ph, and is closely approximated as the signature difference between recent assimilated carbon $\delta_\mathrm{v}^\mathrm{eq}$ and the signature in the atmosphere, δ_a. During photosynthetic uptake plants prefer the uptake of lighter $^{12}CO_2$ molecules associated with kinetic and chemical fractionation effects, leaving the atmosphere relatively heavy in $^{13}CO_2$ molecules. As a result, C_3 plants are depleted in ^{13}C by approximately $-20\,‰$ (relative to the atmosphere) and C_4 to a lesser degree at approximately $-4\,‰$ as they can assimilate $^{13}CO_2$ more efficiently. Given the dominance of C_3 plant growth we estimated a global mean discrimination value of $\epsilon_\mathrm{ph} = -15\,‰$ as shown in Chapter 3. In addition to discrimination effects during photosynthetic uptake, we also need to account for isotopic enrichment of the atmosphere through respiratory release of carbon that has been locked up in both plant and soil organic matter. This carbon reflects the heavier atmospheric ^{13}C content of a few decades ago. This respiratory part will still enrich the atmosphere with $^{13}CO_2$ even if net CO_2 uptake is close to zero [*Ciais et al.*, 1995], and we refer to these processes as the isodisequilibrium fluxes in Equation 4.2.

Discrimination associated with the dissolution of CO_2 in ocean water is much smaller and more spatially homogeneous ($\epsilon_\mathrm{ao} \approx -2\,‰$) than in the terrestrial biosphere. The

δ_{a} in the atmosphere therefore contains additional information on CO_2 fluxes and the global partitioning between ocean and land sinks. This additional constraint on the net fluxes has already been demonstrated in previous studies [e.g., *Ciais et al.*, 1995, *Fung et al.*, 1997, *Keeling et al.*, 1989, *Rayner et al.*, 2008, *Tans et al.*, 1993]. We also have to account for isotopic disequilibrium that exists between the atmosphere and oceans. This disequilibrium flux is associated with the out-gassing of CO_2 from the ocean waters, and increases the $\delta^{13}C$ signatures in the atmosphere.

Besides the land and ocean discrimination, and terrestrial disequilibrium forcing terms, we have three additional terms in Equation 4.2. Firstly, we have CO_2 emissions due to combustion of fossil fuels, which have a distinct isotopic signature (δ_{ff}) depending on the fuel type. Then there are CO_2 emissions due to biomass burning, which we split into two separate terms: $F_{\mathrm{fire}} \cdot \epsilon_{\mathrm{ph}}$ and $F_{\mathrm{fire}} \cdot (\delta_{\mathrm{fire}} - \delta_{\mathrm{v}}^{\mathrm{eq}})$. The latter term quantifies the influence of biomass burning on the terrestrial disequilibrium flux, whereas the former term includes biomass burning as part of the terrestrial net flux, which scales with terrestrial discrimination. The main advantage of writing the isotopic ratio of the fire flux in this manner is that it facilitates calculation of δ_{fire} directly from the ratio of the $^{13}CO_2$ and $^{12}CO_2$ fluxes of F_{fire}, negating the need for an approximation of δ_{v} as discussed in Chapter 2. The separation of fire emissions from N_{bio} is also necessary because the inversion system requires it.

4.2.2   Inversion model with $\delta^{13}C$

We followed the method presented by *Peters et al.* [2005] for the joint CO_2 and $\delta^{13}C$ inversions. Similar to a CO_2-only inversion, we aim to close the CO_2 budget through fluxes from fossil fuel combustion, biomass burning, and net exchange fluxes from the terrestrial biosphere and oceans. In addition, we also intend to simultaneously close the $^{13}CO_2$ ($^{13}C_{\mathrm{a}}$) budget using the same set of CO_2 fluxes. As introduced in Section 1.6, the combined set of equations used in our framework takes the following form:

$$\frac{\mathrm{d}}{\mathrm{dt}} C_{\mathrm{a}} \;\; = \;\; F_{\mathrm{ff}} + F_{\mathrm{fire}} + \lambda_{\mathrm{bio}} N_{\mathrm{bio}} + \lambda_{\mathrm{oce}} N_{\mathrm{oce}}, \tag{4.3}$$

$$\begin{aligned}
\frac{\mathrm{d}}{\mathrm{dt}}\,^{13}C_{\mathrm{a}} \;\; = \;\; & F_{\mathrm{ff}} R_{\mathrm{ff}} + F_{\mathrm{fire}} \lambda_{\mathrm{frac}} \alpha_{\mathrm{ph}} R_{\mathrm{a}} + \lambda_{\mathrm{bio}} N_{\mathrm{bio}} \lambda_{\mathrm{frac}} \alpha_{\mathrm{ph}} R_{\mathrm{a}} + \lambda_{\mathrm{oce}} N_{\mathrm{oce}} \alpha_{\mathrm{ao}} R_{\mathrm{a}} \\
& + \;\; D_{\mathrm{bio}} + D_{\mathrm{oce}}.
\end{aligned} \tag{4.4}$$

Given that we must calculate the absolute mass fluxes of $^{13}CO_2$ in our transport model we cannot use fluxes of isotopic signatures as in Equation 4.2. As discussed in more detail in Section 1.3, the α values represent isotopic discrimination and the R values depict the isotopic ratios in the atmosphere (R_a) or in the different fluxes (and are approximately 0.011). λ_{bio} and λ_{oce} represent the linear scaling factors for each week and region to adjust the net exchange from land and ocean surfaces, respectively. For land, the scaling factor is associated with one scalar per ecoregion based on *Olson* [1985]. The terrestrial biosphere is further divided into 11 larger geographical areas also known as TransCom regions [*Gurney et al.*, 2002]. Each of the 11 TransCom land regions contains a maximum of 19 ecosystem types. The ocean is divided into 30 large basins encompassing large-scale ocean circulation features. This gives a total of 239 ($=11 \cdot 19 + 30$) different scaling factors each week [*Peters et al.*, 2007]. The new parameter in Equation 4.4 is λ_{frac}, which is used to scale a total of 209 terrestrial discrimination parameters per week. They are associated with the same 1×1 degree ecoregions as the terrestrial fluxes. The terrestrial net exchange term in Equation 4.4 ($\lambda_{bio} N_{bio} \lambda_{frac} \alpha_{ph} R_a$) includes two multiplicative scaling factors, making the required solution nonlinear. This poses a potential problem where variations in net exchange and discrimination are cancelling each other out to such a degree that it leads to low signal-to-noise, especially in discrimination. This is further investigated in Section 4.3.1

The fossil fuel combustion, biomass burning, terrestrial and ocean isodisequilibrium fluxes (D_{bio} and D_{oce}), and the ocean and fossil isotopic signatures all remain fixed bottom-up estimates. The fire disequilibrium term is incorporated in the total terrestrial disequilibrium flux D_{bio}.

The scaling factors λ_{bio}, λ_{oce}, and λ_{frac} are the unknowns that are combined in state vector $\mathbf{x}$ [with dimension s], which provides a solution to minimize the quadratic cost function. In this function there is a balance between information drawn from the observation vector $\mathbf{y}$ [with dimension m] with a covariance $\mathbf{R}$ [m x m] and prior knowledge from the state vector $\mathbf{x}_p$ [s] with a covariance $\mathbf{P}$ [s x s]:

$$J(x) = (\mathbf{y} - H(\mathbf{x}))^T \mathbf{R}^{-1} (\mathbf{y} - H(\mathbf{x})) + (\mathbf{x} - \mathbf{x}_p)^T \mathbf{P}^{-1} (\mathbf{x} - \mathbf{x}_p). \qquad (4.5)$$

The observation operator in linearized form $\mathbf{H}$ [m] represents the atmospheric transport model that propagates the surface fluxes from Equation 4.3 and Equation 4.4 and samples accordingly the mole fractions of CO_2 and $^{13}CO_2$ at the same location and moment as the observations $\mathbf{y}$.

The solution for $\mathbf{x}$ that minimizes J is [*Tarantola*, 2004]:

$$\mathbf{x} = \mathbf{x}_p + \mathbf{K} \cdot [\mathbf{y} - H(\mathbf{x}_p)], \tag{4.6}$$

where $\mathbf{K}$ represents the Kalman gain matrix [see *Peters et al.*, 2005]. Equation 4.6 can be expressed in terms of λ (posterior scaling factor), λ_p (prior scaling factor) and separate measurements of CO_2 (c) and $\delta^{13}C$ (δ) with dimensions [j] and [k] respectively:

$$
\begin{pmatrix} \lambda_{\text{bio1}} \\ \vdots \\ \lambda_{\text{bio209}} \\ \lambda_{\text{oce210}} \\ \vdots \\ \lambda_{\text{oce239}} \\ \lambda_{\text{frac240}} \\ \vdots \\ \lambda_{\text{frac448}} \end{pmatrix}
=
\begin{pmatrix} \lambda_{p\text{bio1}} \\ \vdots \\ \lambda_{p\text{bio209}} \\ \lambda_{p\text{oce210}} \\ \vdots \\ \lambda_{p\text{oce239}} \\ \lambda_{p\text{frac240}} \\ \vdots \\ \lambda_{p\text{frac448}} \end{pmatrix}
+ \mathbf{K} \cdot
\left[
\begin{pmatrix} c_1 \\ c_2 \\ c_3 \\ c_4 \\ \vdots \\ c_j \\ \delta_1 \\ \delta_2 \\ \delta_3 \\ \delta_4 \\ \vdots \\ \delta_k \end{pmatrix}
- H
\begin{pmatrix} \lambda_{p\text{bio1}} \\ \vdots \\ \lambda_{p\text{bio209}} \\ \lambda_{p\text{oce210}} \\ \vdots \\ \lambda_{p\text{oce239}} \\ \lambda_{p\text{frac240}} \\ \vdots \\ \lambda_{p\text{frac448}} \end{pmatrix}
\right]. \tag{4.7}
$$

In state vectors $\mathbf{x}$ and $\mathbf{x}_p$ we appended the scaling factors for terrestrial discrimination. Similarly, in the observation vectors $\mathbf{y}$ and $H(\mathbf{x}_p)$ we appended the $\delta^{13}C$ observations immediately after the CO_2 observations. The $\mathbf{K}$ matrix tells us how much a scaling factor needs to change given a set of measurements. The matrices $\mathbf{R}$ and $\mathbf{P}$ determine whether observations or bottom-up estimates are given more weight.

The total size of the $\mathbf{P}$ matrix is 448×448 elements. The first 239×239 element block contains the land and ocean flux uncertainties per region and their spatial correlation. We assign an uncertainty of 80% on the land scalar and 40% on the ocean scalar as in [*Peters et al.*, 2010]. The next 209×209 element block along the diagonal contains terrestrial discrimination uncertainties of 20% with an identical spatial correlation structure as applied to the terrestrial uncertainty scalars. Correlations between ecoregions within a TransCom region decrease exponentially with distance and allow similar flux and discrimination behavior between ecosystems. Furthermore, we allow coupling of ecosystems between nearby TransCom regions, e.g., North America boreal and temperate zones, and Europe and Eurasian zones. We do not allow covariances between net exchange and discrimination in order to give the parameters enough freedom in the solution.

The covariance structure of $\mathbf{R}$ is similar to CO_2-only CarbonTracker, but is extended with additional uncertainties in $\delta^{13}C$ observations. These uncertainties quantify our

ability to simulate observations given the expected uncertainty in atmospheric transport modeling and measurement errors.

With this inversion framework in place the data-assimilation system progresses in a similar manner to the traditional CO_2-only CarbonTracker inversion system. First there is a forecast step, which is driven by our fixed fluxes and current background statevector $\mathbf{x}_p$ to forecast CO_2 and $\delta^{13}C$ 5 weeks ahead in time. This is followed by an analysis step, where we use Equation 4.7 to determine the new state of the system such that it is consistent with the observations for a single week. The analyzed state is propagated to the next cycle using the same model as *Peters et al.* [2007, Equation 1 of Supp. Material], and with this new state a new cycle begins with another forecast step (ahead in time) to determine a new background state with an additional set of observations. For CO_2 and $\delta^{13}C$ ensemble statistics are created from 300 ensemble members to provide a Gaussian probability density function (PDF) of the statevector of net exchange and Δ.

The core of CarbonTracker is the two-way nested global transport model TM5 [*Krol et al.*, 2005]. This application simulates the atmospheric transport of CO_2 and $^{13}CO_2$ at global 6×4 degree resolution. It is driven by 3-hourly meteorological output from ECMWF ERA-interim reanalysis. All the CO_2 flux fields provided to the model are in units of $\mathrm{kg\,CO_2\,m^{-2}\,s^{-1}}$. The isotope flux terms of Equation 4.4 are in $\mathrm{kg\,^{13}CO_2\,m^{-2}\,s^{-1}}$. Atmospheric concentrations of CO_2 and $^{13}CO_2$ are calculated as mole fractions in mol $\mathrm{mol^{-1}}$. Signatures of $\delta^{13}C$ are computed to the relative per mille value using the following conversion formulation in order to facilitate comparison with observations:

$$\delta^{13}C = \left(\frac{R}{R_{\text{ref}}} - 1 \right) \cdot 1000,\tag{4.8}$$

where R_{ref} is the reference ratio adopted for $^{13}C/(^{12}C+^{13}C)$, which is 0.011112 [*Tans et al.*, 1993]. R is the ratio of $^{13}C/C$.

4.2.3 Prior estimates and observations

(1) Terrestrial biosphere fluxes

The terrestrial first-guess net CO_2 exchange and fire estimates come from the Simple-Biosphere Carnegie-Ames Stanford Approach model (SiBCASA). It is a biogeochemical model that calculates carbon, isotope, water, and energy exchange fluxes. It uses driver data such as 3-hourly ECMWF ERA-interim meteorology, remotely sensed Normalized Difference Vegetation Index (NDVI) to track plant phenology, and GFED4 daily burned

area disturbances to calculate fire fluxes at a fine temporal resolution [*Schaefer et al.*, 2008, *van der Velde et al.*, 2013, 2014]. The model incorporates C_3 and C_4 plant types with their own photosynthesis calculations and 12 different ecosystems according to *Olson* [1985]. Respiratory CO_2 release from the plant and soil is calculated in the CASA part of the modeling system using 13 biogeochemical pools with realistic prescribed turnover rates [*Schaefer et al.*, 2008]. The fluxes are calculated on a 1×1 degree grid on a 10 minute time resolution and are further processed into 3-hourly mean fluxes that serve as input for CarbonTracker.

(2) Ocean fluxes

The ocean first-guess net CO_2 flux estimates are calculated with the use of partial pressure differences between atmosphere and ocean [*Takahashi et al.*, 2002]. These are subsequently combined with the quadratic gas-transfer velocity from 3-hourly ECMWF ERA-interim wind fields [*Wanninkhof*, 1992]. An additional trend was applied to the fluxes in accordance with *Jacobson et al.* [2007] to ensure that increases in anthropogenic uptake are proportional to atmospheric CO_2 levels. The final product of these fluxes is provided on 1×1 degree grid at a 3-hourly temporal resolution (see also: `http://www.esrl.noaa.gov/gmd/ccgg/carbontracker/CT2013B_doc.php#tth_sEc2`).

(3) Fossil fuel emissions

In CarbonTracker we include fossil fuel CO_2 emissions, but they are not optimized in the assimilation framework. We used a consistent emission product derived from EDGAR4.2 database, CDIAC, and BP statistics (see also: `http://www.esrl.noaa.gov/gmd/ccgg/carbontracker/CT2013B_doc.php#tth_sEc5`).

(4) Isotope and disequilibrium fluxes

To calculate the fluxes of $^{13}CO_2$ from land surfaces we use the photosynthetic discrimination parameter that is calculated in the SiBCASA model (see Chapters 2 and 3). Note that the discrimination values from SiBCASA are expressed as Δ and are positive. To comply with Equation 4.2, we convert them to negative values (i.e., $\epsilon_{ph} = -\Delta$). The parameterization of Δ consists of several different discrimination processes associated with molecular diffusion, fixation to Rubisco, and mesophyll conductance. The weighted leaf level value for C_3 discrimination is typically 19 ‰, but can vary as it depends strongly on the CO_2 gradient between the atmosphere and leaf interior, which itself depends on the opening and closing of the leaf stomata [see e.g., *Suits et al.*, 2005, *van der Velde*

et al., 2014]. Drier conditions would close the leaf stomata and decrease the stomatal conductance, which increases the CO_2 atmosphere-to-plant gradient. The fractionation inside the plant that is associated with CO_2 fixation by Rubisco and mesophyll conductance becomes less important, and more weight is assigned to fractionation associated with molecular diffusion through the leaf stomata. When there is no water stress the opposite will happen. Given that no substantial fractionation occurs in C_4 plants we assume a constant value of $\Delta_{C4} = 4.4\,‰$ [*Suits et al.*, 2005].

As shown in Equation 4.2 and Equation 4.4, the terrestrial isotopic exchange is separated into three terms. The first two terms are associated with terrestrial natural net CO_2 exchange and biomass burning, and are both in equilibrium with the isotopic signature in the atmosphere. In SiBCASA we produced weekly mean 1×1 degree fields for Δ which are used to transform the regular 3-hourly net CO_2 flux fields to net $^{13}CO_2$ flux fields:

$$^{13}N_{\mathrm{bio}} = N_{\mathrm{bio}} \cdot \alpha_{\mathrm{ph}} \cdot R_{\mathrm{a}}, \tag{4.9}$$

where α_{ph} is the notation for the photosynthetic discrimination parameter in ratio space and R_{a} is the atmospheric $^{13}CO_2/CO_2$ ratio. The former is calculated from its ϵ_{ph} analog [see e.g., *Tans et al.*, 1993]:

$$\alpha_{\mathrm{ph}} = \frac{\epsilon_{\mathrm{ph}}}{1000} + 1. \tag{4.10}$$

The biomass burning flux is calculated in the same manner:

$$^{13}F_{\mathrm{fire}} = F_{\mathrm{fire}} \cdot \alpha_{\mathrm{ph}} \cdot R_{\mathrm{a}}. \tag{4.11}$$

The third terrestrial isotopic term in Equation 4.4 represents the part of the gross natural respiratory and fire fluxes that are in isotopic disequilibrium (D_{bio}). Carbon originating from different SiBCASA carbon pools is older and more enriched in ^{13}C than the isotopic signature of recently fixed photosynthates. The SiBCASA pool configuration is described in detail in Chapter 3.

TABLE 4.1: List of all the main state and flux variables, and their units and resolution. The units given here are used for the general understanding of the equations but some have been converted for use in TM5 model.

Symbol	name	units	dimensions
C_a	CO_2 carbon content in atmosphere	Pg C	1
$^{13}C_\mathrm{a}$	$^{13}CO_2$ carbon content in atmosphere	Pg C	1
δ_a	$\delta^{13}C$ signature in atmosphere	‰	1
δ_ff	$\delta^{13}C$ signature in fossil fuels	‰	1
δ_v	$\delta^{13}C$ signature in land vegetation	‰	land grid
δ_fire	$\delta^{13}C$ signature in fire fluxes	‰	land grid
δ_v^{eq}	$\delta^{13}C$ signature in vegetation in equilibrium with atmosphere	‰	land grid
δ_a^{eq}	$\delta^{13}C$ signature in equilibrium with ocean surface	‰	ocean grid
F_ff	Fossil fuel carbon flux	Pg C yr^{-1}	land grid
F_fire	Biomass burning carbon flux	Pg C yr^{-1}	land grid
F_la	Respiratory carbon flux	Pg C yr^{-1}	land grid
F_oa	Ocean carbon outgassing flux	Pg C yr^{-1}	ocean grid
N_bio	Net land carbon flux	Pg C yr^{-1}	land grid
N_oce	Net ocean carbon flux	Pg C yr^{-1}	land grid
D_bio	Land disequilibrium flux	Pg C ‰ yr^{-1}	land grid
D_oce	Ocean disequilibrium flux	Pg C ‰ yr^{-1}	ocean grid
Δ	Photosynthetic discrimination calculated in SiBCASA	‰	land grid
ϵ_ph	Photosynthetic discrimination in Equation 4.2 ($=-\Delta$)	‰	land grid
ϵ_ao	Ocean discrimination	‰	1
α_ph	Photosynthetic discrimination in ratio space	-	land grid
α_ao	Ocean discrimination in ratio space	-	1
c_x	measured CO_2 mole fractions at location x	µmole mole^{-1}	1
δ_x	measured $\delta^{13}C$ at location x	‰	1
$\mathbf{x}$	state vector	-	448
$\mathbf{x}_\mathrm{p}$	prior state vector	-	448
$\mathbf{y}$	observations vector	µmole mole^{-1} and ‰	s
$H(\mathbf{x}_\mathrm{p})$	observation operator	µmole mole^{-1} and ‰	s
$\mathbf{R}$	Covariance matrix observations	(µmole mole^{-1})^2 and (‰)^2	s × s
$\mathbf{P}$	Covariance matrix state vector	-	448 × 448

The ocean discrimination parameter ϵ_ao is fixed at $-2\,‰$, as in many comparable studies. Fluxes of $^{13}N_\mathrm{oce}$ are calculated in the same manner as for $^{13}N_\mathrm{bio}$. The ocean isodisequilibrium flux D_oce is determined from the out-gassing flux of CO_2 scaled with the disequilibrium of the ocean surface and atmosphere, i.e., $F_\mathrm{oa} \cdot (\delta_\mathrm{a}^\mathrm{eq} - \delta_\mathrm{a})$. The $\delta_\mathrm{a}^\mathrm{eq}$ is determined from a global network of ^{13}C measurements in dissolved inorganic carbon. F_oa is parameterized as a function of surface ocean partial pressure of CO_2 and windspeed after *Takahashi et al.* [2009]. Windspeed and solubility are assumed to remain constant year-to-year. The disequilibrium fluxes are positive from the equator to approximately 60 degrees of latitude in both directions and are negative beyond that.

We produced monthly 1×1 degree fields of D_bio and D_oce (derived in kg $^{13}CO_2$ m^{-2} s^{-1}) for use in CarbonTracker. As explained further in Section 4.3.1 these fluxes require additional scaling to close the long-term mean budget.

TABLE 4.2: Summary of assigned δ^{13}C observation uncertainty (derived from a previous joint inversion experiment), the category-average uncertainty $\pm$ standard deviation of the innovation χ^2, and number of sites per category.

Site category	r [‰]	χ^2	# sites
land	0.13	0.97±0.52	10
mixed	0.080	0.80±0.34	11
marine boundary layer	0.03	1.29±0.70	15
deep Southern Hemisphere	0.03	1.22±0.44	7
problem	0.4	0.63±0.48	10

(5) Observations

Observations from a wide range of research laboratories are bundled in Observation Package (ObsPack) version 1.0.3 for CO_2 and version 0.9.0 for isotope ratios δ^{13}C. These are experimental data products, but include the provider's original data and metadata reformatted into the ObsPack framework.

From the available CO_2 observations, approximately 24,000 weekly air-filled flask measurements were used in the assimilation from a fixed network of 58 surface sites. Another large set of 174,000 measurements came from 23 semi-continuous in-situ sites. These CO_2 measurements were obtained using a non-dispersive infrared (NDIR) analyzer with a precision of ± 0.1 ppm. The remainder of sites and measurements (including from aircraft or shipboard) were not used because of double records, and some data was kept for independent checks. A small fraction was omitted as our model could not resolve certain locations at a coarse resolution.

For the joint inversions we also used 22,000 flask measurements of δ^{13}C from 53 different surface sites. A further 5,600 measurements from five different sites were obtained using programmable flask packages (PFP), which measure δ^{13}C at a much higher resolution (daily). δ^{13}C is measured by dual inlet mass-spectrometry with a precision of ± 0.012 ‰.

We determined observation uncertainties r for each of the δ^{13}C measurement sites empirically from earlier test inversions. These values are bundled together with the uncertainty values for CO_2 in the covariance $\mathbf{R}$ (in the diagonal). If the error is too small we would give an unrealistic amount of confidence to the measurements whereas if the error is too large we would give very little credence to the measurements.

We divided the δ^{13}C measurement sites into different categories each with their own observation uncertainty value. These categories are: land, mixed conditions, marine boundary layer (mbl), deep Southern Hemisphere, and a special category for problem sites where forecast performance is poor. For each site we determined the innovation statistic χ^2, which is a measure for how appropriate our applied uncertainty level is. Ideally χ^2 is around 1.0, implying that the actual simulated model-data mismatch and the

TABLE 4.3: Summary of the four different inversion experiments, the observations used, and their linearity. The prefix *Common* means that similar experiments have been performed in previous studies. The prefix *New* means that this type of inversion has not been done before.

Experiment	observations	linearity
Common-CO2	CO_2	yes
Common-d13C	CO_2 and $\delta^{13}C$	yes
New-d13C	CO_2 and $\delta^{13}C$	no
New-2step	CO_2 and then $\delta^{13}C$	yes

expected model-data mismatch are about equal. Values below 1.0 indicate the expected uncertainty is overestimated and values above 1.0 mean that the expected uncertainty is underestimated. Table 4.2 gives a summary of the site categories used, together with the assigned uncertainty r for $\delta^{13}C$ and the category-average innovation χ^2 determined from a joint inversion experiment. For the majority of sites the innovation value ranges between 0.7 and 1.3, i.e., around the ideal value of 1.0.

4.2.4   Experiments

We performed four different inversion experiments, as summarized in Table 4.3. The simulation period covered the years 2000 through 2011, but our analyses focused on the period 2001-2011, i.e., we omitted the spinup year. As a benchmark we performed a traditional inversion to estimate the net carbon exchange fluxes of the ocean and land using only CO_2 observations. The setup of this experiment, which we call Common-CO2, was similar to the CarbonTracker releases for North America [*Peters et al.*, 2007] and Europe [*Peters et al.*, 2010], except for the absence of zoom regions. For the second inversion we added $\delta^{13}C$ observations alongside CO_2 to constrain only the exchange fluxes. Similar inversions were performed in previous studies, therefore we call this experiment Common-d13C. The experiment in which we estimated discrimination and fluxes simultaneously is called New-d13C. This inversion was nonlinear because the discrimination term was multiplied by the net carbon exchange flux. To test the robustness of this inversion we performed a final linear inversion experiment where we estimated only the land discrimination parameter. We call this experiment New-2step because discrimination was solved in a second step after optimization of the net exchange fluxes. That meant that ocean and land fluxes were derived from the optimized statevector and its covariance from the Common-CO2 inversion.
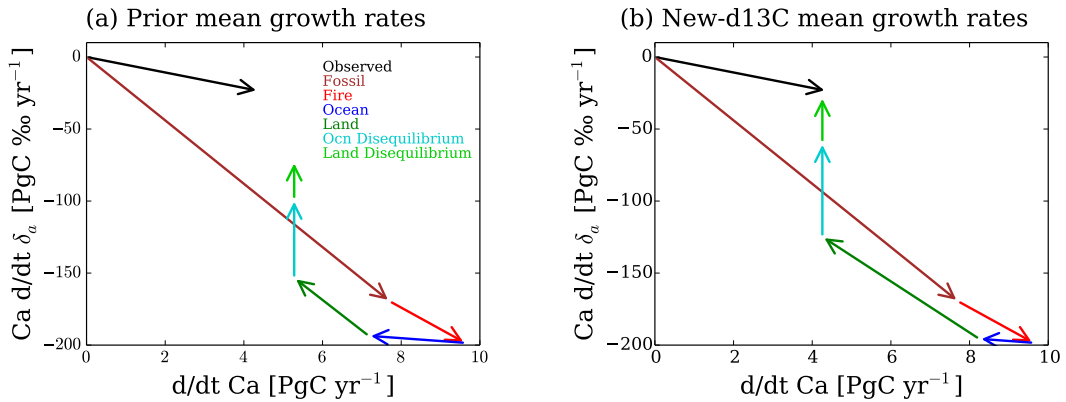
FIGURE 4.1: Annual mean carbon (x-axis) and δ^{13}C (y-axis) growth rates for (a) the prior estimates and for (b) the New-d13C experiment. Colored arrows represent the different sources and sinks of the carbon cycle. A closed budget for both tracers was accomplished in the New-d13C experiment, as indicated by the resultant vector (sum of all colored arrows) returning to the black arrow (observed growth rate in atmosphere). To close the long-term trend we increased the disequilibrium fluxes by 20 %.

4.3 Results

4.3.1 Joint inversion approach

δ^{13}C long term trend fit

As shown in Figure 4.1a, the prior flux estimates and unscaled disequilibrium fluxes were not large enough to close the gap with the observed tracers. The sum of the flux arrows overestimated the annual CO_2 growth rate along the x-axis and overestimated δ^{13}C depletion along the y-axis. In a traditional Common-CO2 inversion the newly estimated ocean and land fluxes are appropriately scaled in order to close the CO_2 budget along the x-axis. The leverage in the net exchange fluxes is however not large enough to close the δ^{13}C budget along the y-axis as well. In an inversion that includes δ^{13}C observations, the gap in δ^{13}C would adjust the CO_2 flux magnitudes and ocean/land partitioning quite dramatically to unrealistic magnitudes in an effort to overcome the large biases in the simulated δ^{13}C growth rate. Thus, we instead chose to use scaled disequilibrium fluxes in the Common-d13C, New-d13C, and New-2step inversions, in order to estimate land and ocean CO_2 flux magnitudes that remained close to the results of other traditional carbon cycle budgeting studies. The disequilibrium fluxes were used to adjust the budget because (1) the exact magnitudes of these terms were still unknown due to uncertainties in the carbon pool turnover and gross carbon fluxes, and (2) these terms do not affect the CO_2 mass balance. With these scaled fluxes we could close the mean δ^{13}C budget of our inversions relatively easy without creating unrealistic carbon sinks over land and oceans (Figure 4.1b). The assumption of a closed long-term budget was necessary because we

focused our study on interannual changes in the fluxes and land discrimination parameter, and not on changes in multiyear trends.

We obtained the best fit with δ^{13}C data when the land and ocean disequilibrium flux was scaled by a factor of 1.2. This is consistent with recent double deconvolution studies where the global δ^{13}C balance was closed with a factor of 1.3 in land and ocean disequilibrium [*Alden et al.*, 2010, *van der Velde et al.*, 2013]. This value was the result of an ensemble of different sets of scaling factors (ranging from 1.1 to 1.5) in a forward TM5 simulation, which was driven by the optimized net land and ocean flux estimates from the Common-CO2 experiment. This assured a closed δ^{13}C budget together with a closed CO_2 budget. As selection criteria we used (1) the 12-year mean RMSE of a large selection of δ^{13}C sites and (2) the average bias between simulated and observed values. In the non-scaled disequilibrium simulation we obtained a RMSE of 0.165 ‰ and a bias of -0.110 ‰. The optimal result was obtained with a scaling factor of 1.2, which reduced the RMSE to 0.079 ‰ and the mean bias to -0.010‰. This set up (with a closed long-term mean budget) was used to study IAV and seasonal variations. Note that these scaling factors cannot be applied to other inversion studies because the disequilibrium scaling factors are tuned for this particular system. A slightly different ocean and land uptake partitioning changes the δ_a budget and thus requires different disequilibrium fluxes.

Robustness of nonlinear estimates

We tested the assumption that the New-d13C inversion (where we scale the land carbon exchange and isotopic discrimination simultaneously) was appropriate. We hypothesized that a region's uptake and discrimination would change in a similar fashion in the nonlinear New-d13C as it would for the linear Common-CO2 and New-2step inversions. As displayed in Figure 4.2, the 11-year mean carbon land uptake for the 11 TransCom land regions were very similar in the New-d13C and Common-CO2 inversions. Deviations were in the order of teragrams, and thus within 1σ standard deviation of the flux IAV. The 11-year mean discrimination values of New-d13C and New-2step were also in close agreement. Figure 4.2 also shows the impact of C_4 photosynthesis on the mean TransCom discrimination value. In the boreal regions where there is no C_4 plant growth, the discrimination was at its maximum (approximately 20 ‰, 5 ‰ above the global average), but in regions where there is C_4 plant growth (e.g., due to agriculture in United States or savannas in Africa) the mean discrimination values were lower (approximately 12–15 ‰). These regional patterns imposed by SiBCASA were not affected in the New-d13C inversion framework. Given that we were looking to retrieve robust temporal patterns of IAV, the real indicators for the robustness of our nonlinear inversion approach were given by the correlation coefficients (r) between the two inversions. We calculated r of uptake
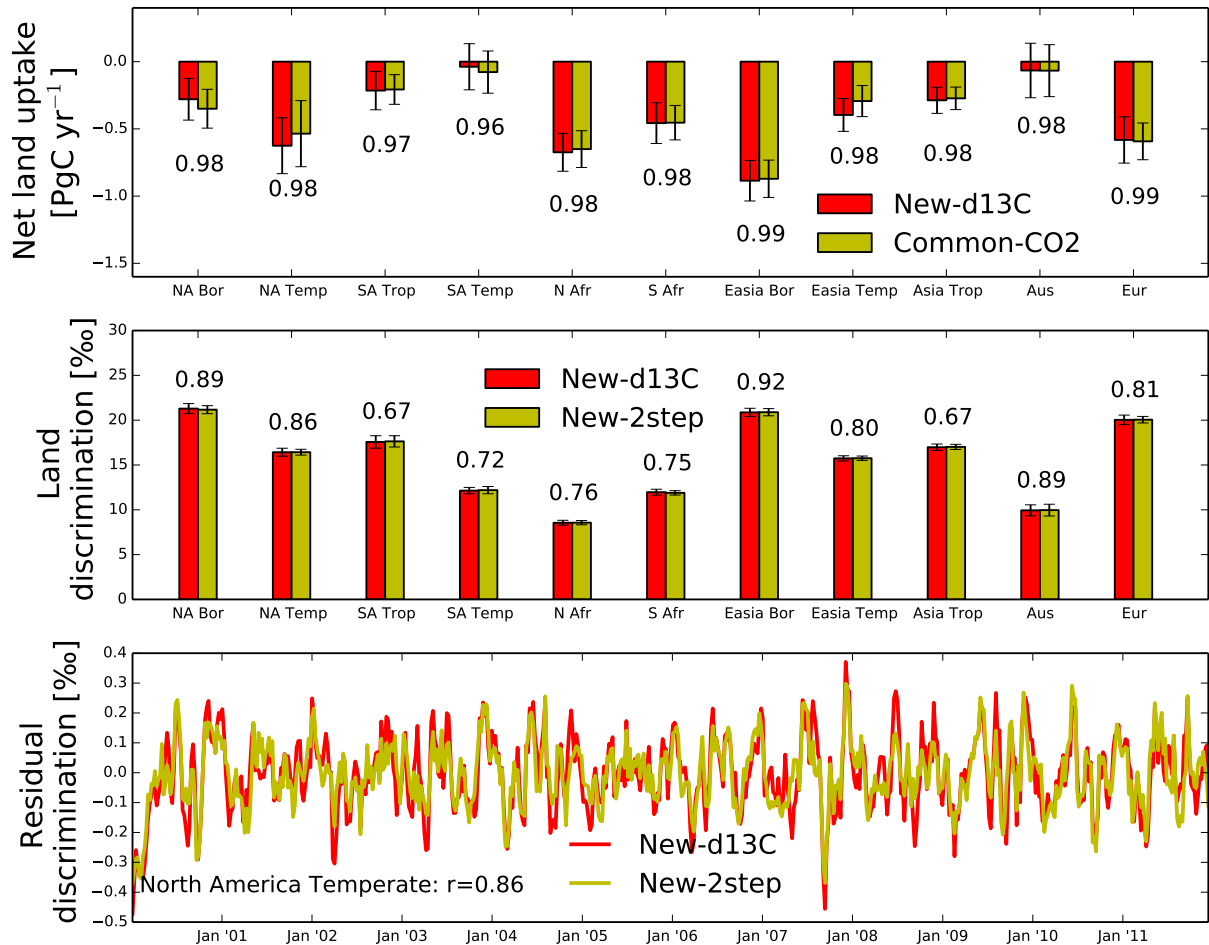
FIGURE 4.2: In the top panel the 11-year mean land uptake flux $[\mathrm{Pg\,C\,yr^{-1}}]$ for each TransCom region. The estimates from the New-d13C inversion are in red and estimates from the Common-CO2 inversion are in yellow. Error bars depict 1σ standard deviation of the flux IAV. The 11-year correlation coefficients r between the two inversion methods are given underneath the bars. These correlations are based on the 3-month boxcar mean anomalies after subtracting the seasonal cycle. In the middle panel we compare the discrimination parameter between the New-d13C inversion and the New-2step inversion. We again provide IAV error bars and correlation coefficients between inversion methods. The lower panel displays the 3-month box car mean anomalies in discrimination for the North America Temperate TransCom region to illustrate the high degree of similarity between both inversion methods ($r = 0.86$).

between Common-CO2 and New-d13C inversions and r of discrimination between New-2step and New-d13C inversions. As the seasonal cycles in uptake and discrimination were largely dictated by the prior estimates, we removed them using a 3-month boxcar mean smooth curve fitting to obtain the anomalies relative to the seasonal cycle. The residuals of the land uptake in New-d13C were very similar to the residuals from the Common-CO2 inversion, as indicated by the high r-values (> 0.96) for all TransCom regions. The r values were lower for discrimination, but still exceeding 0.75 in the Northern Hemisphere. The degree of correlation was particularly high over North America Boreal, North America Temperate, and European regions (as shown in Figure 4.2). Smaller correlations were realized in Tropical and Temperate South America and Tropical Asia. This is expected, however, as these regions typically suffer from a lack of observational constraints.

Additional analyses compounded the high degree of similarity between the New-d13C and New-2step inversions. Both inversion systems estimated large carbon sinks in the extra-tropical regions in the Northern ($-3.16\,\mathrm{Pg\,C\,yr^{-1}}$) and Southern Hemispheres ($-1.28\,\mathrm{Pg\,C\,yr^{-1}}$), and estimated the tropical oceans as the only net source of carbon ($0.84\,\mathrm{Pg\,C\,yr^{-1}}$). Tropical land carbon exchange was close to neutral in both inversions because the fire emissions almost fully compensated the uptake by vegetation. In addition, in both inversions the carbon uptake was dominated by land in the Northern Hemisphere ($-2.33\,\mathrm{Pg\,C\,yr^{-1}}$), and the ocean flux was responsible for the calculated net sink in the Southern Hemisphere ($-1.29\,\mathrm{Pg\,C\,yr^{-1}}$).

The distributions of atmospheric CO_2 and $\delta^{13}C$ residuals (observed minus simulated) were very similar between the different inversion methods. Notwithstanding, the level of agreement with $\delta^{13}C$ observations was higher for the New-d13C inversion in comparison to the Common-CO2 and New-2step (Figure 4.3a-b). This is because the Common-CO2 inversion was not constrained by $\delta^{13}C$ data and the fit with $\delta^{13}C$ observations, and therefore relied solely on the disequilibrium fluxes. Conversely, the New-2step inversion was constrained by $\delta^{13}C$, but lacked leverage on the atmosphere because it could only adjust land discrimination. As a result, the ratio of the RMSD of New-d13C to the RMSD of the Common-CO2 and New-2step inversions was less than 0.95 (indicating a higher accuracy of New-d13C) in most locations (Figure 4.3a-b). Furthermore, there was notable geographic variability in the relative performance of inversion techniques, indicating the utility of New-d13C in the Northern Hemisphere due to the large availability of measurements and scalable discrimination parameters. There are only two sites where New-d13C performed markedly better than Common-d13C: Mauna Loa, Hawaii and Assekrem, Algeria (Figure 4.3c). This means that a large proportion of the $\delta^{13}C$ improvements were made with the net exchange fluxes and the remainder with the land discrimination parameter. The New-d13C inversion also led to small improvements in
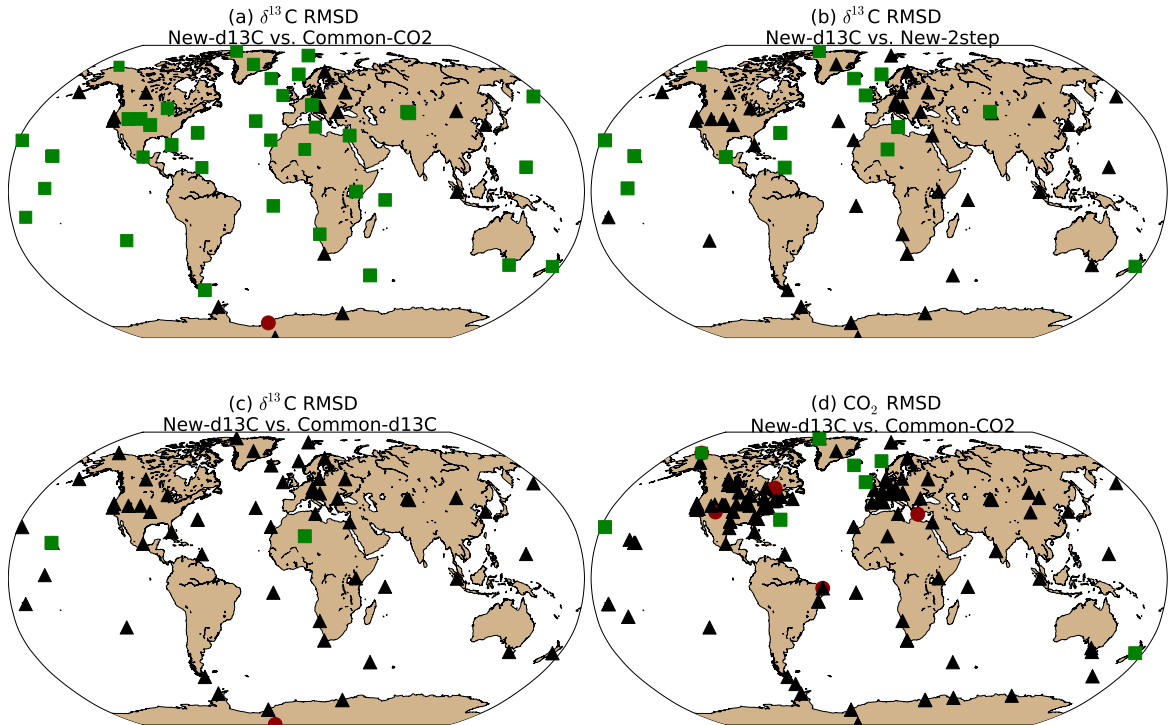
FIGURE 4.3: A comparison of the relative performance of inversion techniques based on the ratio of the δ^{13}C root mean square difference (RMSD) of New-d13C to the RMSD of the (a) Common-CO2, (b) New-2step, and (c) Common-d13C inversions. Panel (d) shows the ratio of CO_2 RMSD of New-d13C to the RMSD of the Common-CO2 inversion. A ratio lower than one indicates a higher accuracy of the New-d13C inversion technique: green sites indicate a ratio ≤ 0.95, red sites indicate a ratio ≥ 1.05, and sites where the difference in respective RMSD's is less than 0.05 are given in black.

simulated CO_2 mole fractions across seven observational sites (Figure 4.3d). Globally, however, the changes in CO_2 mole fractions remained small and there were no indications that information from δ^{13}C observations on net exchange is inconsistent with what we learned from CO_2 observations.

At specific sites like Alert (Canada) or Ulaan Uul (Mongolia), the New-d13C inversion performed slightly better than the Common-d13C and New-2step inversions (Figure 4.4). The New-d13C residuals tended to be closer to zero than the other inversions and the standard deviation of the probability density function was typically smaller. On shorter weekly times scales the differences in δ^{13}C residuals between the different inversions were not easily perceptible. Weekly fluctuations in modeled δ^{13}C were very noisy and very similar for the Common-d13C, New-d13C and New-2step inversions. To pinpoint certain signals by eye in a single δ^{13}C time series and attribute them to a certain process is therefore an almost impossible task. In the coming sections we focus instead on interpreting the data from the large observational network to infer the signals in net exchange and discrimination over larger regions.
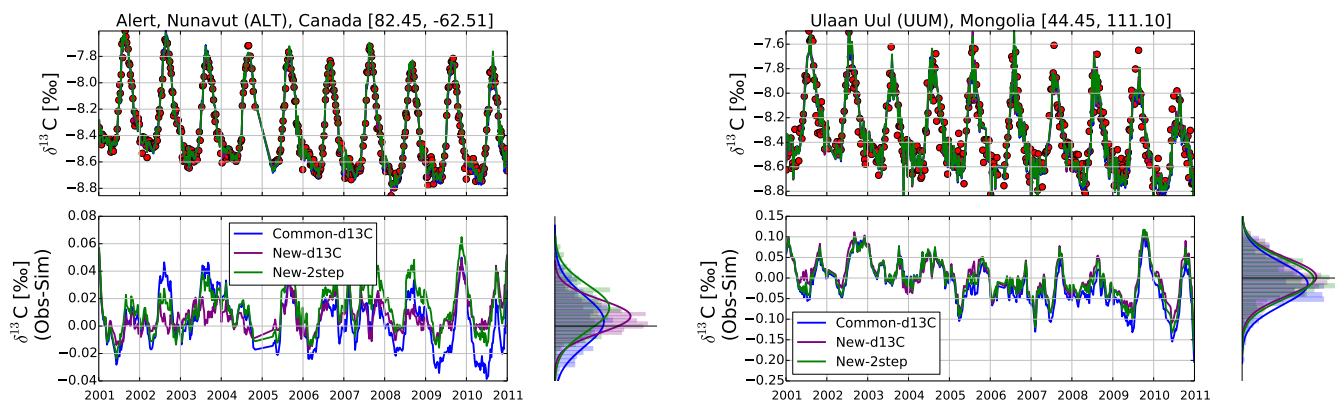
FIGURE 4.4: Comparison of three different inversion experiments at two sites: Alert (ALT, Canada) and Ulaan Uul (UUM, Mongolia). The top panel of each site displays $\delta^{13}C$ observations (red markers) together with simulated $\delta^{13}C$ from Common-d13C (blue), New-d13C (purple), and New-2step (green). The differences between simulations are small and are therefore more readily distinguished in the bottom panel, which shows the residuals of observation minus simulation. The residual probability density function (PDF) of each simulation is displayed to the right of the lower panels. At most sites the New-d13C residuals tend to be closer to zero and with a smaller standard deviation.

An aspect worth mentioning is the slight declining trend in the residuals of Figure 4.4. In all inversions we scaled the disequilibrium fluxes globally by 20 %, however, given that we used a single scaling parameter for the whole globe, a precise fit can never be attained. This is especially apparent, for example, from 2009 onwards, at Alert, where the Common-d13C residuals notably increased in magnitude. The New-d13C and New-2step inversions compensated this offset by adjusting the discrimination estimates accordingly to obtain a better fit with the data. That implies an increasing problem with the long-term trend as it will be aliased into the mean discrimination signals in New-d13C. Interpretation of the more recent data is therefore difficult until we employ a more sophisticated method to account for the regional trend in $\delta^{13}C$.

4.3.2 Northern Hemisphere flux and discrimination interannual variability

Table 4.4 reports the net exchange flux and discrimination (mean $\pm$ IAV (1σ)) in the Northern Hemisphere for all four experiments. Differences in the 11-year mean fluxes were small. In Common-d13C there was a shift of 210 $\mathrm{Tg\,C\,yr}^{-1}$ more land uptake and 120 $\mathrm{Tg\,C\,yr}^{-1}$ less ocean uptake than in Common-CO2, but the global carbon uptake remained unchanged. The relatively small realignment in flux partitioning between the four inversions in this study suggests that the previously mentioned 'flux-leakage' was never an issue in CarbonTracker, mainly because of its relatively short inversion window of one week.
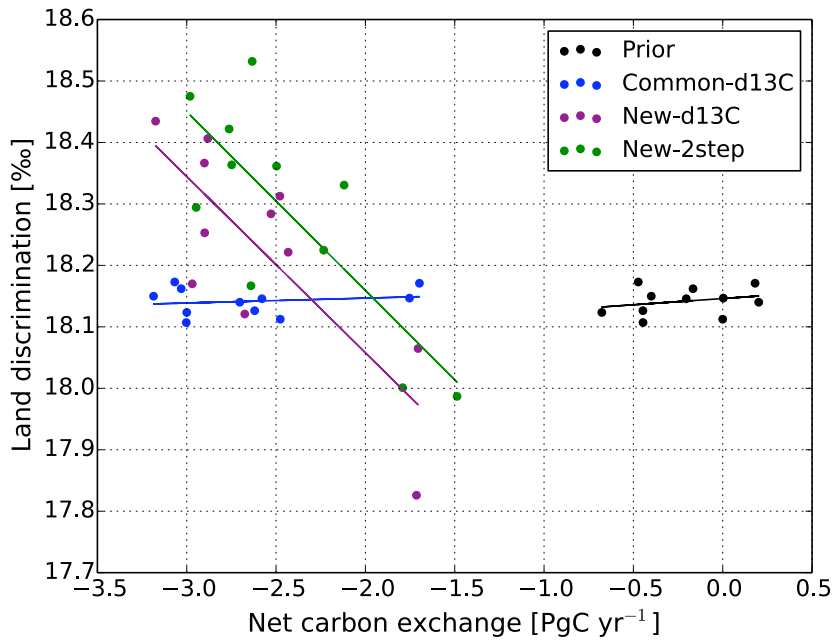
FIGURE 4.5: Scatter diagram of the annual net carbon exchange (NEE) and land discrimination for the Northern Hemisphere for different simulations: prior (black), Common-d13C (blue), New-d13C (purple), and New-2step (green). The correlation coefficient between NEE and discrimination increases significantly (for New-d13C and New-2step) when discrimination is allowed to vary freely in the optimization.

The Common-d13C inversion led to slightly more IAV in the net exchange fluxes than the Common-CO2 inversion. We speculated about this behavior in our budgeting experiment in Chapter 2. Ocean and land flux IAV had to increase simultaneously to close the CO_2 and $\delta^{13}C$ budgets.

The New-d13C inversion estimated a smaller IAV in land net ecosystem exchange (NEE) than in the Common-d13C inversion, while the IAV in discrimination increased 8-fold (standard deviation) compared to the first-guess estimate of SiBCASA-GFED4. In addition to this increase in discrimination IAV, we also found a stronger negative correlation between land discrimination and NEE on annual scales (r = −0.79). It means that reduced carbon uptake during a drought was accompanied by reduced discrimination as we would expect. These changes in discrimination and the correlation with NEE were driven by $\delta^{13}C$ observations. The correlation of NEE and discrimination led to a larger range in isofluxes of $^{13}CO_2$, which was necessary for closing the budget (Equation 4.4). The increased covariations were not just a symptom of the systems inability to separately estimate NEE and discrimination variations, as was evidenced by the New-2step inversion where the same correlations were made when separately using CO_2 and $\delta^{13}C$ observations as constraints. This suggests that the estimated IAV of discrimination was truly a signal retrieved from $\delta^{13}C$ that was not interpreted in previous inversions.
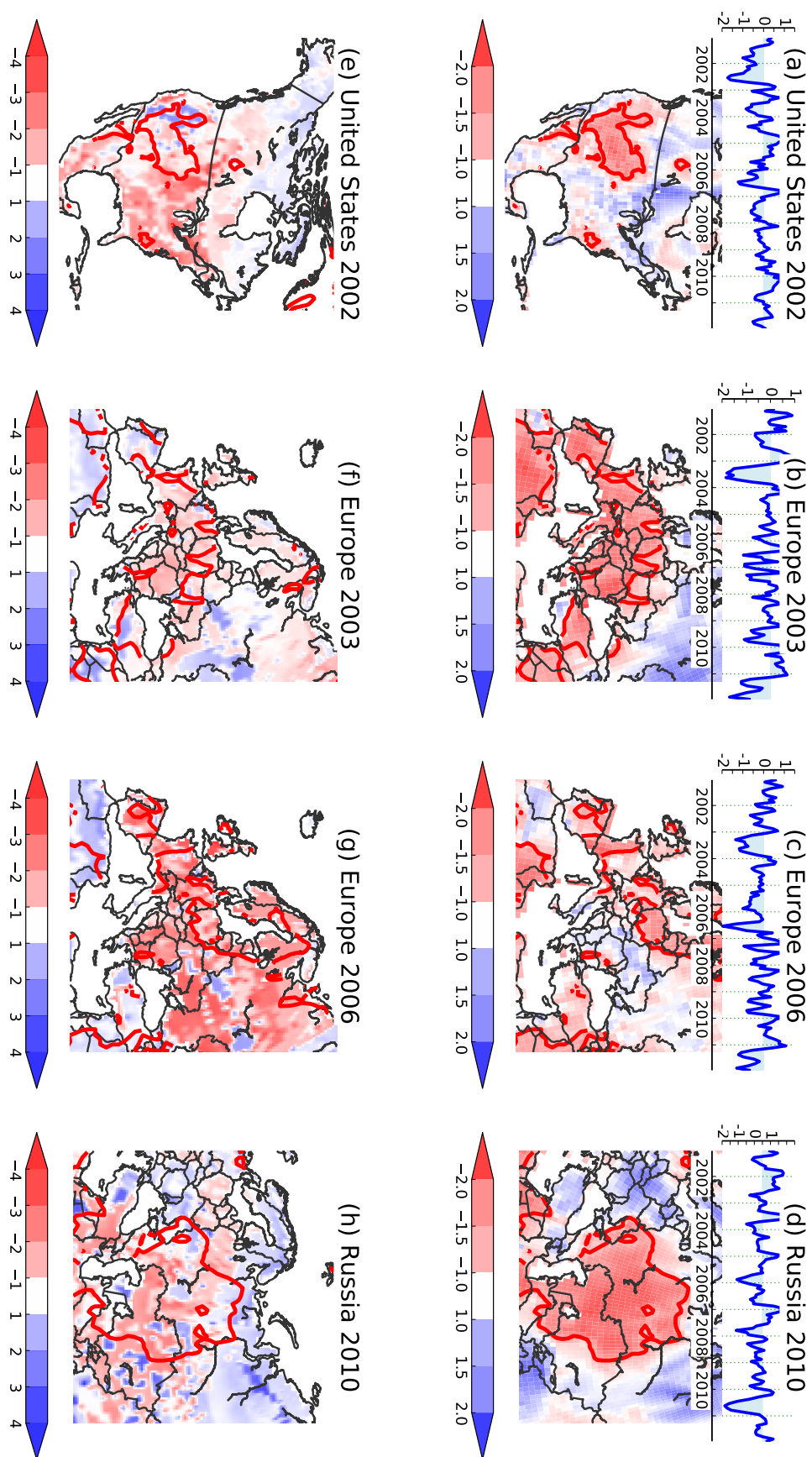
FIGURE 4.6: Top four panels show the SPEI index for: (a) United States in 2002, (b) Europe in 2003, (c) Europe in 2006, and (d) Russia in 2010. The lower panels (e) to (h) show the corresponding optimized discrimination anomalies in ‰ (New-d13C) in comparison to the surrounding years around 2002, 2003, 2006 and 2010, respectively. Red contours show where SPEI < -1.2 (severe drought).
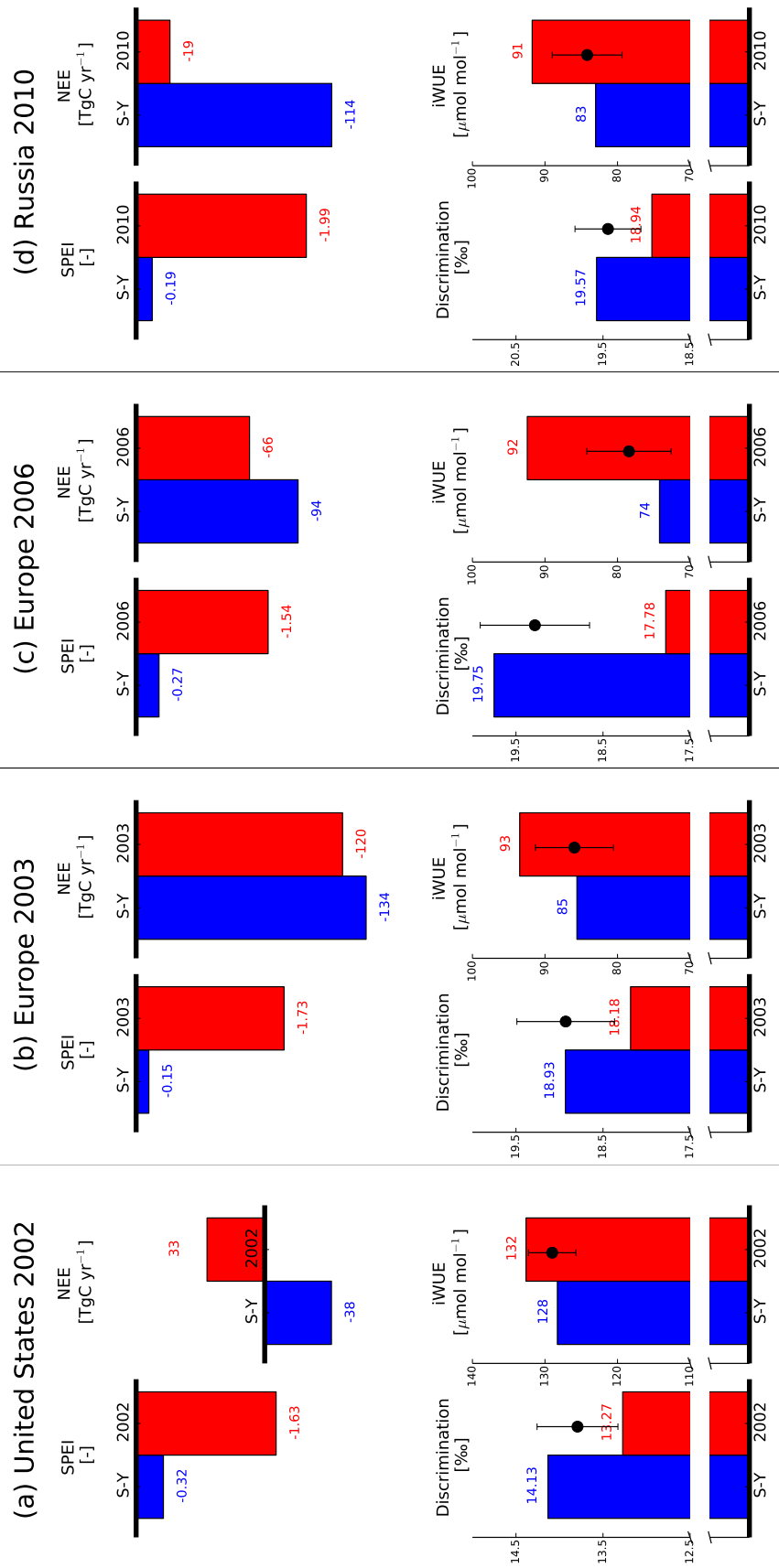
FIGURE 4.7: Mean estimates for SPEI and NEE (upper row), and discrimination and iWUE (lower row), for the following regions: (a) United States in 2002, (b) Europe in 2003, (c) Europe in 2006, and (d) Russia in 2010. Red bars represent the specific drought year, and blue bars represent the mean of the surrounding years (S-Y). Values are labelled above and below each bar for clarity. Discrimination and iWUE bars are discontinuous and include the 11-year mean ± IAV (1σ) indicator.

TABLE 4.4: Northern Hemisphere net land and ocean exchange [Pg C yr^{-1}], land discrimination [‰] 11-year mean estimates, and IAV ($\pm 1\sigma$ standard deviation) from the four experiments. The last line gives the correlation coefficient r between 11 annual mean NEE and discrimination values.

	Prior	Common-CO2	Common-d13C	New-d13C	New-2step
net land	−0.22±0.28	−2.44±0.46	−2.65±0.49	−2.58±0.46	−2.44±0.46
net ocean	−1.23±0.06	−0.86±0.05	−0.74±0.11	−0.78±0.09	−0.86±0.05
land discrimination	18.1±0.02	18.1±0.02	18.1±0.02	18.2±0.17	18.3±0.17
land and discr. corr. coef.	0.26	0.14	0.18	−0.79	−0.78

The correlation between NEE and discrimination is visualized in Figure 4.5. Prior NEE from SiBCASA was small, approximately $-0.22\,\text{Pg C yr}^{-1}$ and correlated weakly with discrimination (r = 0.26, Table 4.4). In Common-d13C, the posterior NEE sink increased to approximately $-2.65\,\text{Pg C yr}^{-1}$ with more IAV, but yet again the correlation was weak with SiBCASA's discrimination (r = 0.18). The correlation increased in New-d13C and New-2step (r = −0.79 and −0.78, respectively), which was physically more consistent with isotope fractionation effects in plant leaves. A smaller carbon sink is often caused by reduced GPP (and increased TER), which should also result in reduced isotope discrimination.

The New-2step inversion was in many respects similar to New-d13C inversion as shown in the previous section. Although the posterior IAV in ocean and land uptake was identical to the Common-CO2 inversion, it absorbed much more IAV in discrimination. This increased IAV also resulted in a strong negative correlation between NEE and discrimination, as in New-d13C. The disadvantage of the New-2step inversion was that CO_2 and $\delta^{13}C$ observations were fully separated in estimating the net exchange fluxes and discrimination. Only CO_2 observations were used to estimate the net exchange fluxes in the first step, and subsequently only $\delta^{13}C$ observations were used to estimate the discrimination parameter in the second step. Any covariability in the $\delta^{13}C$ and CO_2 observations was omitted in the solution, whereas in the New-d13C inversion information from both tracers were projected simultaneously on the net exchange flux and land discrimination.

We focused here on increased IAV in land discrimination because it forms the key to improving prediction of carbon exchange processes in biosphere models. Droughts in particular have been shown to impact this exchange strongly. We already identified in Chapter 3 a lack of response in isotope exchange at higher VPD regimes in the SiBCASA model. In the following section we investigate further where this additional IAV in discrimination is projected onto, and what the covariations of NEE and discrimination mean in terms of the parameterized drought response in SiBCASA.

4.3.3 Optimized anomalies in discrimination and WUE

We selected four different occurrences of continent-wide severe drought events. As a metric we used the Standardized Precipitation-Evapotranspiration Index (SPEI) based on climatic data [*Vicente-Serrano et al.*, 2010]. It is used to estimate the magnitude of drought conditions with respect to normal conditions in a variety of natural and agricultural ecosystems. The four summer drought instances where $SPEI < -1.2$ (classified as severe drought or worse) are shown in Figure 4.6a-b-c-d. The droughts were: United States (2002), Europe (2003 and 2006), and Western Russia (2010). As shown by the time series inserts, SPEI anomalies were largest over the last decade in their respective region.

The four summer droughts correlated with negative anomalies in discrimination (Figure 4.6e-f-g-h). However, there were discrepancies between the locations of SPEI and discrimination anomalies. In the US, the drought region with index < -1.2 covered states like Utah, Nevada and Colorado, i.e., regions where estimated GPP and NEE are already small. The isoflux $N_{bio} \cdot \epsilon_{ph}$ in Equation 4.2 was likewise small and therefore it had little impact on the atmospheric $\delta^{13}C$ composition. Instead, the largest discrimination anomalies were realized outside the severe drought region in the eastern part of the US where photosynthetic activity is generally higher and where the isoflux has more leverage on the atmosphere. These discrimination anomalies were placed in the same region as the net exchange anomalies estimated by *Peters et al.* [2007, Figure 3]. Similarly, the discrimination anomalies over Europe and Russia were not confined within the SPEI boundaries. The inability of our system to precisely place discrimination anomalies within the driest regions is potentially due to the limited number of available observations and scalable parameters.

Figure 4.7 shows the mean values of SPEI, NEE, discrimination, and iWUE. Each was calculated in the region where $SPEI < -1.2$ for the drought year and for the surrounding years. Mean SPEI indices were not only more negative during the drought year, droughts also reduced uptake of CO_2, and reduced discrimination, leading to an increased area mean iWUE. The reduction in discrimination was larger than the 11-year discrimination IAV (1σ) for the US and Europe. In the US in 2002, the discrimination decreased by 0.86 ‰ relative to the surrounding years. This anomaly was well outside the 1σ standard deviation of the year-to-year variations (± 0.51 ‰), but within 2σ. In Europe, the reduced discrimination value exceeded 1σ IAV by 30 % in 2003 and 270 % in 2006. Note that the SPEI drought area for 2006 was 44 % smaller than in 2003 (1.1 million km^2 vs. 2.0 million km^2), but the estimated discrimination anomalies were stronger. In Russia in 2010, the discrimination value dropped to 18.94 ‰; a change that was 30 % larger than the 11-year mean annual variations (± 0.50 ‰). Although these results act
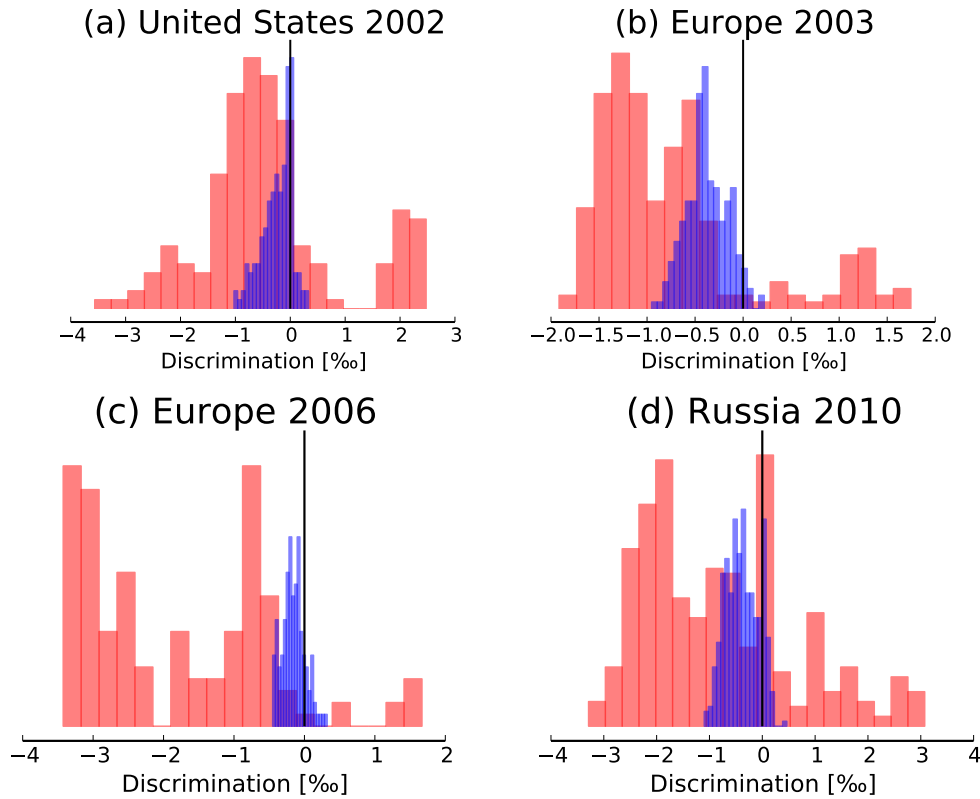
FIGURE 4.8: Histograms of discrimination anomaly frequencies for: (a) United States in 2002, (b) Europe in 2003, (c) Europe in 2006, and (d) Russia in 2010. Optimized anomalies are shown in red and prior anomalies in blue.

as convincing evidence that observational information can be used to infer changes in land discrimination during extreme events, we are aware that SPEI anomalies are not precisely located at the sites of NEE and discrimination adjustment. By defining a larger region over the US, European, and Eurasian continents we also included other relevant gridcells outside the drought area, which made the results more significant. For instance, including the eastern part of the US in the analysis reduced the discrimination by 1.5 ‰, which is almost four times larger than the 11-year IAV. A wider selection of the European region reduced the mean discrimination anomaly by 0.7 ‰ relative to the surrounding years. As outlined in Section 4.1, there is a negative correlation between plant isotopic exchange and the intrinsic water-use efficiency (iWUE). As shown in Figure 4.7, our new estimates of reduced discrimination during the drought years also resulted in significant increased values of iWUE using Equation 4.1c.

Within the SPEI region, a large number of grid cells showed a reduction in discrimination values of 1 ‰ in comparison to the other years (Figure 4.8). All distributions were skewed towards negative anomalies, as large as −3.5 ‰. Our prior estimates did predict a shift during the droughts, which indicates a drought response was present in the SiBCASA model, but to a lesser extent than the optimized solutions.
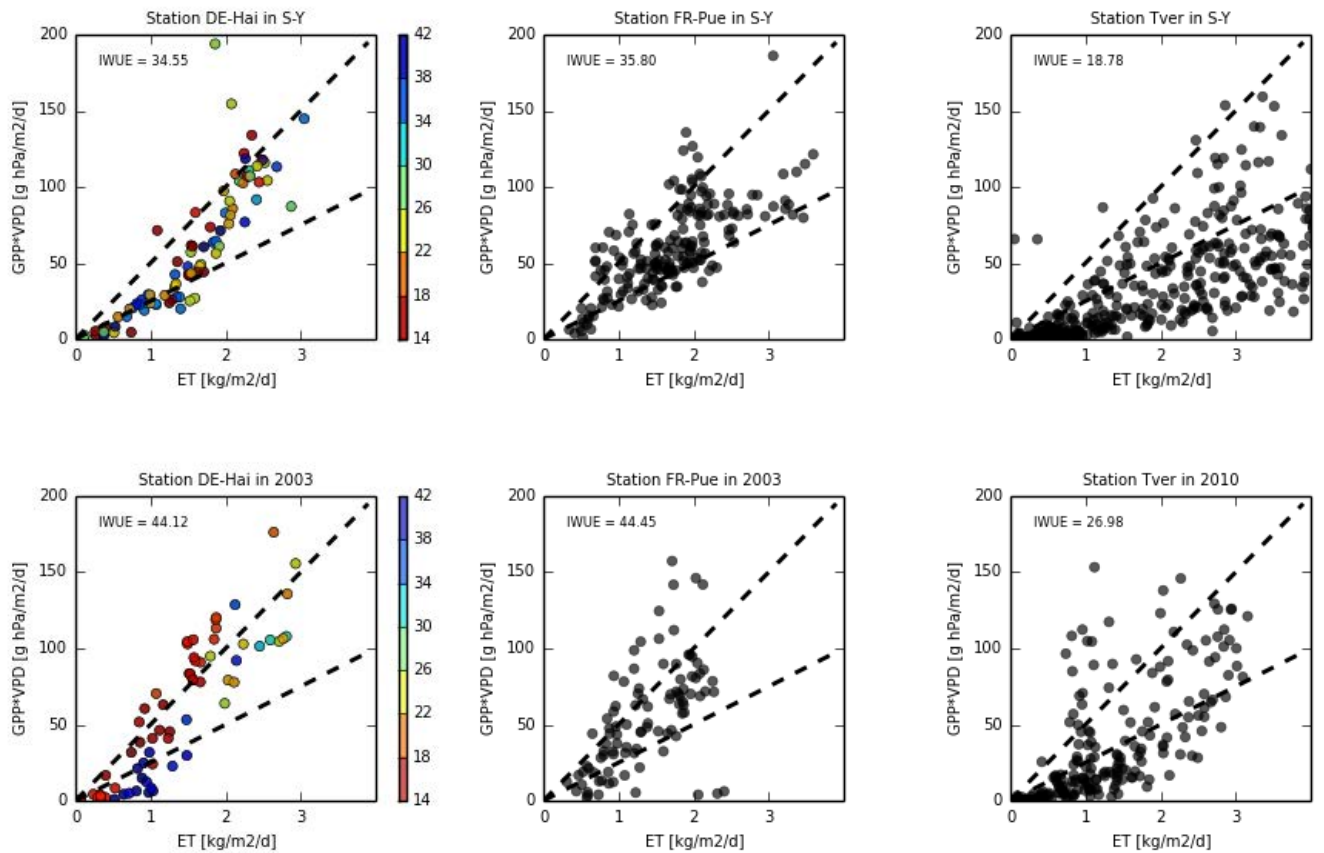
FIGURE 4.9: Relationship between daily mean GPP·VPD and ET measured for Hainich, Germany (left panels), Puechebon, France (center panels), and Tver, Russia (right panels) for surrounding years, S-Y (top) and drought year (bottom), respectively. Dashed reference slopes predict GPP·VPD by 25·ET and by 50·ET. The colored markers indicate the volumetric soil water content [%] for the Hainich site. (Figure was inspired by the ones presented by *Beer et al.* [2009])

Measurements from eddy-covariance sites in Europe and North America (Fluxnet and Ameriflux) confirmed that intrinsic water use efficiency (iWUE = GPP·VPD/ET) increased during severe droughts. Due to lack of direct isotope and discrimination measurements, iWUE is the only widely available metric to investigate changes in isotope discrimination. As shown in the Section 4.1, in the iWUE formulation the ratio VPD/ET is an approximate measure for surface resistance ($1/g_s$). During severe droughts the VPD is generally high and leaf stomata will close, resulting in a smaller stomatal conductance value and a larger VPD/ET ratio. Subsequently, this leads to increases in the CO_2 gradient between atmosphere and leaf interior, a larger iWUE and a smaller leaf level discrimination value, as predicted by Equations 4.1a-b-c. We used intrinsic WUE because it is more informative on describing biochemical functions in plants than the more general GPP/ET relationship. *Beer et al.* [2009] found at a large number of sites that the relationship between GPP and ET is not as strong as the relationship between GPP·VPD

and ET due to the nonlinear effect of VPD on ET. As consequence, the correlation co-efficients of GPP·VPD and ET were generally better than for GPP and ET.

During the European drought of 2003 and the Russian drought of 2010 we found consid-erable increases in iWUE in comparison to the two surrounding years for a selection of sites (Table 4.5). This behavior was not confined within a small region or country, but was measured across western Europe. It confirms the large extent of the drought event, as was indicated by the SPEI index. For three of these sites we plotted in Figure 4.9 the relationships of GPP·VPD and ET: Hainich, Germany (DE-Hai), Puechabon, France (FR-Pue) and Tver, Russia. Generally, higher GPP·VPD values at a given ET value were observed at these locations in comparison to the preceding and following years. At all three sites the annual mean iWUE increased with around $10\,\mathrm{g\,C\,hPa\,kg^{-1}\,H_2O}$ during the drought year, representing an increase of roughly 30 to 40 %. Similar increases were observed at other European sites. The drought also lowered the volumetric soil water content as indicated by the colored markers for the Hainich site. For instance, in 2002 the soil water content was 6 % higher in comparison to 2003 and 2004.

For the United States in 2002, we found similar increases in iWUE: Indiana (US-MMS), Howland (US-Ho1), and rainfed land in Nebraska (US-Ne). However, for most of the other available sites the differences between 2002 and the surrounding years were small. The US anomalies in iWUE were not as widespread and unequivocal as in Europe, partly because some of the US sites listed contained irrigated crops that would be protected from severe drought conditions. In addition, most of the sites were located outside the SPEI drought region, which made it difficult to assess the drought response in a similar way to Europe.

4.4 Discussion and conclusions

We developed a new version of the CarbonTracker data assimilation system that simu-lates two atmospheric tracers simultaneously: CO_2 and the $\delta^{13}C$ isotope ratio in CO_2. We used measurements of both trace gases to optimize year-to-year changes in the land discrimination parameter. The signal-to-noise in the optimized fluxes and discrimination improved with an increasing number of observations from the different research groups around the world. One important improvement would be to increase the number of measurement sites (for both CO_2 and $\delta^{13}C$), particularly in sparsely sampled areas in the tropics. Fortunately, new efforts are currently underway to improve our atmospheric measurement capacity in these areas. New vertical profiles of CO_2 were recently mea-sured at four different sites in the Amazon that provided new insights on the carbon cycle under drought conditions [*Gatti et al.*, 2014]. Simulations to incorporate these new

TABLE 4.5: Mean iWUE for the drought year (D-Y) and surrounding years (S-Y) derived for a selection of European Fluxnet sites for 2003, United States Ameriflux sites for 2002, and a Russian site for 2010.

Country	Site name	Site ID	iWUE D-Y	iWUE S-Y	relative change iWUE [%]	SPEI
Belgium	Viesalm	BE-Vie	42	27	55	-1.2
Finland	Sodankyla	FI-Sod	21	19	10	-0.8
France	Hesse Forest	FR-Hes	48	37	29	-1.6
France	Puechebon	FR-Pue	44	36	22	-2.0
Germany	Hainich	DE-Hai	44	35	26	-1.5
Germany	Tharandt	DE-Tha	45	35	29	-1.7
Germany	Wetzstein	DE-Wet	34	24	42	-1.7
Hungary	Bugacpuszta	HU-Bug	23	19	21	-2.2
Italy	Island of Pianosa	IT-Pia	22	12	83	
Netherlands	Loobos	NL-Loo	41	31	32	-1.2
Spain	El Saler	ES-Es1	20	15	33	-2.0
Russia (Tver oblast)*	Tver		27	19	42	-1.5
US, Arizona	Audubon Research Ranch	US-Aud	26	27	-4	-0.8
US, California	Blodgett Forest	US-Blo	19	23	-17	0.2
US, California	Tonzi Ranch	US-Ton	43	39	10	0.2
US, California	Vaira Ranch	US-Var	23	22	5	0.2
US, Florida	Mize	US-SP2	22	22	0.7	
US, Illinois	Bondville	US-Bo1	26	27	-4	1.1
US, Indiana	Morgan Monroe State Forest	US-MMS	35	21	67	0.8
US, Maine	Howland	US-Ho1	42	35	20	0.3
US, Montana	Fort Peck	US-FPe	8	25	-68	0.4
US, Nebraska	Mead Irrigated	US-Ne1	21	22	4	0.4
US, Nebraska	Mead Rainfed	US-Ne3	24	16	50	0.4
US, Wisconsin	Willow Creek	US-WCr	18	18	0	1.2

*Data was gratefully received from from J. Kurbatova en A. Varlagin, from Severtsov Institute of Ecology and Evolution, Russia.

measurements are currently underway in CarbonTracker [van der Laan-Luijkx et al., 2014, submitted to GBC]. Our results show that, in addition to new CO_2 measurements, an increase of the number of $\delta^{13}C$ flask samples and in-situ measurements would be of great value. New in-situ measurement techniques developed for $\delta^{13}C$, such as a tunable diode laser absorption spectrometer [Schaeffer et al., 2008], could further improve our estimates of carbon and isotope exchange.

An important aspect of this study is that we detected signals in atmospheric $\delta^{13}C$ that were not interpretable from a single measurement site. Currently, the only way to infer patterns in NEE and discrimination from $\delta^{13}C$ over large regions is to use a system like CarbonTracker to simultaneously interpret data from a large observational network. Given that NEE and discrimination form a multiplicative term, the estimation approach is nonlinear. This makes it difficult to disentangle NEE and discrimination signals, leading to a low signal-to-noise ratio, particularly in discrimination. Drought conditions had to be severe and extend over an area with a relatively dense $\delta^{13}C$ network, in order that the signals in discrimination observed from our background network exceeded the noise. We highlighted several such instances from 2000 through 2011 in the Northern

Hemisphere in the Results section. For other cases, however, the signals were still weak because the drought was not intense enough or the measurement network was insufficient. For instance, we could not find robust drought signals in China or Brazil because of poor observational coverage in those areas. Future work will focus more on the recent events such as the 2012 United States drought.

The current study provides a novel approach to estimating regional isotope discrimination. It is standard practice in inverse modeling to improve simulated atmospheric CO_2 by optimizing net carbon exchange fluxes. Here, we additionally targeted the terrestrial discrimination against ^{13}C to improve the simulated atmospheric $\delta^{13}C$. This raises the question whether the extra variability in discrimination that arises is a reliable proxy for environmental stress affecting stomatal conductance and photosynthesis. The inversion system predicted larger negative anomalies in land discrimination during periods of intense droughts. The projection of additional variability onto the simulated discrimination in our New-d13C inversion is an independent indication that the simulated drought response is underestimated. This suggests that the vegetation drought stress response, and thus also the isotope discrimination in our prior biosphere model, are inadequate. In Chapter 3 we showed that SiBCASA generally has a weak response in discrimination to changes in humidity, as well as a latency in recently assimilated $^{13}CO_2$ to become available for respiration. With field measurements of the isotopic composition of respired CO_2 as a benchmark, we improved the isotopic discrimination by an additional reduction of the stomatal conductance under very dry conditions (high VPD). This reduced the c_i/c_a ratio but kept it within a reasonable range, and was large enough to locally improve the discrimination signature by a marked amount. Additional model experiments suggested that on a larger scale regional droughts could increase variability in the discrimination and respiration signatures beyond what we currently simulate. Preliminary results focusing on Eurasia suggest that at least some role is played by the simulation of too high soil moisture in late summer in SiBCASA (van der Molen, personal communication, 2014), but more work is needed to confirm this due to the paucity of local measurements.

The suggested lack of drought response is unlikely to be a trait exclusively affecting our terrestrial biosphere model. Other types of biosphere models could respond similarly to droughts. A recent carbon model comparison study (GEOCARBON) showed strong agreement between our SIBCASA-GFED4 model, Cardamom and MTE [*Jung*, 2009] simulations of GPP. All models estimated a mean GPP around $120\,Pg\,C\,yr^{-1}$, with a very similar seasonal cycle and latitudinal gradient in GPP. This suggests the models depend strongly on the satellite derived fPAR and NDVI data that is driving them, combined with the use of similar photosynthesis and stomatal conductance models to calculate GPP. This is particularly important because a number of models in the climate model intercomparison project (CMIP5) use similar parameterizations for photosynthetic

uptake and stomatal conductance to simulate future climate [*Dai et al.*, 2012]. The coupling between the carbon cycle and climate is one of the most uncertain factors in these models [*Cox et al.*, 2013, *Piao et al.*, 2013], leading to an unknown loss of carbon sequestration capacity of (mostly tropical) vegetation under an increased drought frequency and intensity. The use of trace gasses like $\delta^{13}C$ are possible avenues of research that could provide more insights on land ecosystem behavior during such extreme events.

A final notable aspect of this study is that the interannual variability in NEE increases in the inversion where $\delta^{13}C$ is included to estimate net exchange fluxes (Common-d13C). This behavior was hypothesized in Chapter 2 and *Alden et al.* [2010] in the double deconvolution model using global growth rates of CO_2 and $\delta^{13}C$. We expected changes in NEE to simultaneously close the observed growth rates of CO_2 and $\delta^{13}C$, particularly under the assumption of low ocean exchange variability and low disequilibrium variability. In the current study, the extent of variability increase between a traditional Common-CO2 inversion and the Common-d13C inversion is, however, small in the Northern Hemisphere (from ± 0.46 to ± 0.49 PgC yr^{-1} in 1σ standard deviation). It confirms the findings of *Rayner et al.* [2008] who found that with additional $\delta^{13}C$ observations the land IAV and its anti-correlation with the ocean IAV increased slightly at some latitudes. The additional variability projected onto NEE in our Common-d13C inversion was not unrealistic. The possibility, therefore, that part of the variability in NEE originated from IAV in the land discrimination parameter is unlikely to have posed a problem in previous studies. Nevertheless, our New-d13C approach is better able to close the CO_2 and $\delta^{13}C$ budgets simultaneously, and results in similar variability in NEE to a traditional CO_2-only inversion (Common-CO2), but also leads to more variability in the discrimination parameter (8-fold in the Northern Hemisphere). The latter would have remained undetected in traditional Common-CO2 and Common-d13C inversion calculations.

To summarize, we performed a series of inversions using two chemical tracers measured in the atmosphere: CO_2 and $\delta^{13}C$. We found using both tracers in an inversion gives consistent results with the traditional inversion using only CO_2 as a tracer. The use of $\delta^{13}C$ in our system confirms that previous CarbonTracker inversions were not suffering from a large misallocation of carbon between the land and ocean reservoirs. In addition, we performed a set of inversions where we projected part of the $\delta^{13}C$ variability onto the land discrimination parameter. This parameter changes under environmental stress and forms a nonlinear multiplicative term with the net carbon exchange flux in the $\delta^{13}C$ budget equation. We found that the nonlinearity does not pose a problem and that our approach is robust: the outcome of the inversion where we estimated NEE and discrimination either simultaneously or sequentially was very similar. Both approaches gave consistent estimates for NEE and discrimination, both in the multi-year mean as well as in the interannual and seasonal variations. The main outcome of this study was

that the posterior discrimination anomalies became consistently more negative during large severe droughts in the Northern Hemisphere, exceeding the prior estimates. Since isotope discrimination is strongly linked to stomatal conductance at the leaf surface, this study highlights how $\delta^{13}C$ measurements in the atmosphere can be used to recognize a lack of drought response in terrestrial biosphere models.

Chapter 5

General discussion and outlook

5.1 Introduction

The primary goal of this thesis was to study a new observational constraint on the global CO_2 exchange. This work was required because uncertainties in fluxes over natural carbon sinks are still large and this hinders our ability to estimate future climate forcing and the response of the global carbon cycle to climate. We used observations of isotopic ratios in CO_2 to improve our understanding of the specific processes of carbon exchange, as this has provided insight in previous studies of the global carbon cycle. For example, *Levin et al.* [2003] and *Bozhinova et al.* [2014] were able to quantify regional fossil fuel combustion using ^{14}C. The other rare carbon isotope, ^{13}C, can help distinguish oceanic from terrestrial CO_2 exchange [*Ciais et al.*, 1995]. This is because terrestrial uptake of the heavier $^{13}CO_2$ molecule is reduced by $2\,\%$ in comparison to oceanic uptake. In addition, changes in discrimination against ^{13}C in the terrestrial biosphere reflect reduced photosynthesis resulting from droughts. Efforts to use both tracers (^{14}C and ^{13}C) in carbon cycle studies have been limited thus far because important questions remain regarding their use, such as: on what scales can they constrain the global carbon budget, and in which ecosystems do these methods work best? With the availability of observations increasing each year, it is important that models are continuously improved to interpret these data.

In this thesis we focused on improving and understanding the modeling of ^{13}C in CO_2 on different scales and from different perspectives; either top-down or bottom-up. Chapter 2 dealt with closing the global budget of atmospheric CO_2 and $\delta^{13}C$ using global mean estimates of ^{13}C discrimination for ocean and land, and prescribed surface exchange fluxes from different models. Special attention was paid to identifying key flux

parameters responsible for interannual variability. Given that we anticipated more variability from the terrestrial isotope fluxes, we improved the accuracy of modeled $^{13}CO_2$ exchange in Chapter 3. We found a limited response in the terrestrial discrimination to changes in environmental conditions such as humidity and soil moisture. Following on this improvement, we developed novel inverse discrimination calculations within a data-assimilation framework to analyze the effects of droughts on ^{13}C exchange around the world. In Chapter 4 we combined atmospheric transport modeling with detailed bottom-up process modeling within our integrated data-assimilation framework to optimize key parameters of the CO_2 and $^{13}CO_2$ budget.

In this chapter we continue with a review of the main insights obtained on the combined CO_2 and $\delta^{13}C$ budget using different methods of varying complexity. This is followed by an analysis of the important terrestrial $^{13}CO_2$ flux parameters, disequilibrium and discrimination, and their uncertainty, and we investigate the role that droughts play in $^{13}CO_2$ exchange. We also provide a review of our multi-tracer inversion framework and the lessons learned. In the final section we give an outlook for future research.

5.2   The carbon budget and its flux variability

This thesis described two different methods that use atmospheric observations of CO_2 and $\delta^{13}C$ to explain net carbon exchange fluxes and the behavior of specific ^{13}C exchange processes (discrimination and disequilibrium). In Chapter 2 we used a simple budgeting approach to close the budgets between the global observed atmospheric growth rates in CO_2 and $\delta^{13}C$ and bottom-up flux estimates. We made the assumption of a well-mixed atmosphere where the global growth rates of CO_2 and $\delta^{13}C$ represent the sum of all surface fluxes of CO_2 and $^{13}CO_2$; net exchange and disequilibrium fluxes from the ocean and land, biomass burning, and fossil fuel combustion. Special emphasis was placed on closing the budget of interannual variability (IAV) assuming low variability in ocean exchange and a closed budget in CO_2. We posed the following research question in the Main Introduction, Section 1.4 on page 12:

RQ1: How can we close the IAV budget in $\delta^{13}C$ given a closed budget in CO_2 and low IAV in ocean uptake?

The main outcome of RQ1 is that annual $^{13}CO_2$ exchange was less variable than needed to close the variability budget in $\delta^{13}C$. The variability gap could be closed by either projecting excessive variability in the net exchange fluxes using double deconvolution,

resulting in an unrealistically large anticorrelation between ocean and land, or by projecting variability in other terms. Additional variability could come from the disequilibrium, as discussed in Section 5.3, or from terrestrial discrimination as discussed in Section 5.4. Biomass burning and fossil fuel combustion were not likely candidates to explain the variability gap, although the IAV of these two fluxes deserves more rigorous treatment in the future as their isotopic signatures might be more intermittent year-to-year. Misrepresentation of the year-to-year variability in the global growth rates of CO_2 and $\delta^{13}C$ was another possible cause for the variability gap, as discussed in Chapter 2, Section 2.3.3 on page 38.

To overcome limitations in the budgeting study, in Chapter 4 we developed a more detailed inversion approach that used actual measured atmospheric mole fractions of CO_2 and $\delta^{13}C$ to estimate the net exchange fluxes on refined spatial and temporal scales. The inversion that used two tracers simultaneously (called Common-d13C) led to more IAV in the net exchange fluxes than in the traditional CO_2-only inversion (Common-CO2), and confirmed the outcome of the simple budgeting approach in Chapter 2. The main difference was that the amount of projected variability in the land flux remained within reasonable levels, as opposed to the double deconvolution estimate. This demonstrated that simple budgeting techniques are useful to differentiate between terrestrial and oceanic mean CO_2 uptake over a period of several years [confirmed by, e.g., *Ciais et al.*, 1995, *Tans et al.*, 1993]. Nevertheless, the method has been found unreliable to reconcile the IAV budget between global averaged growth rates derived from measurements and bottom-up flux estimates. This underlines the need for a more sophisticated inversion framework, such as CarbonTracker, that takes actual measurements from a global network as input. A gap filled and time smoothed representation of observed atmospheric concentrations lacks the spatial detail to study carbon exchange processes [*Peters et al.*, 2005]. In particular, interpreting small changes in measured $\delta^{13}C$ are critical for identifying changes due to drought stress.

Observational coverage over the tropics and other scarcely populated areas is still problematic. We expect, however, that inversion estimates will improve with a greater number of measurements in those regions. Recent measurement campaigns of vertical CO_2 profiles in the Amazon [*Gatti et al.*, 2014] will likely improve our understanding of the regional carbon budget. New studies are currently underway to include such measurements in Carbontracker and the initial results suggest that carbon uptake in the Amazon was reduced in 2010 due to large scale droughts [Van der Laan-Luijkx et al., 2014, submitted to GBC]. Inversions with additional surface CO_2 measurements from China and aircraft CO_2 measurements from the CONTRAIL (Comprehensive Observation Network for Trace gases by Airline) program improved carbon uptake estimates over Asia [*Zhang et al.*, 2014]. The increase of the number of $\delta^{13}C$ sites and high frequency measurements

are just as important as additional CO_2 measurements, especially to understand specific ^{13}C exchange processes in more detail, as explained in the following sections.

5.3   Terrestrial disequilibrium

An important aspect of using $\delta^{13}C$ in an inverse modeling study are the disequilibrium fluxes from the ocean and the terrestrial biosphere. These fluxes arise because $\delta^{13}C$ of atmospheric CO_2 is continuously depleted through the burning of fossil fuels, which are light in ^{13}C [Suess Effect, *Keeling*, 1979]. Thus, an isotopic disequilibrium exist between CO_2 moving in and out of ocean and land reservoirs. In Chapter 2 we showed that this term cannot be neglected in the $\delta^{13}C$ budget, and that underestimated disequilibrium fluxes could easily reduce the accuracy of net land and ocean carbon flux estimates in a double deconvolution. A 30 % increase in the disequilibrium fluxes closed the observed mean $\delta^{13}C$ budget and produced realistic land and ocean CO_2 fluxes in the double deconvolution, which is also demonstrated by *Alden et al.* [2010]. The need for enlarging was also confirmed in the more explicit spatial and temporal inversions in Chapter 4, which showed that an increase in disequilibrium of at least 20 % was required to improve the simulated decline in $\delta^{13}C$ at all measurement sites around the world. The large underestimation of our bottom-up disequilibrium estimates is not a unique feature of SiBCASA, as it also observed in other models. *Thompson and Randerson* [1999] found uncertainties in calculated terrestrial disequilibrium of up to 30 % in different simulations and models. The disequilibrium fluxes require: (1) information on atmospheric $\delta^{13}C$ depletion (due to the Suess Effect) over long periods of time, (2) the residence time and $\delta^{13}C$ signature of carbon in the ocean and land reservoir, (3) isotopic discrimination during carbon uptake, and (4) the gross carbon flux from the reservoirs to the atmosphere. A general underestimation of global GPP and TER in terrestrial biosphere models could explain a large fraction of the underestimation in terrestrial disequilibrium. This will be further discussed in Section 5.6.

In Chapter 2 we focussed on the terrestrial contributors of IAV in the CO_2 and $\delta^{13}C$ budgets. It has been hypothesized that the the terrestrial disequilibrium flux holds a large part of the IAV because of the relatively short residence times of carbon in the terrestrial biosphere, and due to its greater response to environmental changes [*Alden et al.*, 2010]. We therefore posed a second research question in Section 1.4 on page 12:

RQ2: What are the main drivers responsible for terrestrial disequilibrium IAV?

More specifically, we wanted to know if these drivers had enough leverage to provide extra variability. In Chapter 2 we studied the drivers of year-to-year changes in the terrestrial disequilibrium flux: $F_{la}(\delta_v - \delta_v^{eq})$ and $F_{fire}(\delta_{fire} - \delta_v^{eq})$. Firstly, variations are caused by changes in the δ_v^{eq} signature (i.e. the signature in newly formed plant matter) due to changes in atmospheric δ_a and terrestrial discrimination ϵ_{ph}. Discrimination can change either by the opening and closing of leaf stomata in response to environmental conditions or due to annual shifts in the proportion of GPP between C_3 and C_4 plants, thus affecting the mean ϵ_{ph} [*Scholze et al.*, 2003]. Another source for variability is natural respiration F_{la}, although variations in respiration from live biomass and soil carbon pools are expected to dampen out due to the large size of the terrestrial reservoir [*Alden et al.*, 2010]. Fire disturbances and their intermittent nature can impact the atmospheric $\delta^{13}C$ budget, but most of the variability originates from the burning of forested areas and peatlands (mostly C_3 vegetation), which is also suggested by *Randerson et al.* [2005]. In comparison to the atmospheric signature, C_3 vegetation is more depleted in ^{13}C than C_4 vegetation [*O'Leary*, 1988]. C_4 dominated ecosystems generally have a short carbon residence time, giving them an isotopic signature that lies closer to the atmospheric value.

Another source of variability in the terrestrial disequilibrium flux is the residence time of carbon [*Carvalhais et al.*, 2014], which is expressed by variations in signatures of δ_v that carry through the series of carbon reservoirs (i.e., leaves, stems, roots, soils). Reservoirs with long residence times, e.g., carbon locked up in permafrost, have an isotopic signature that is much older and richer in ^{13}C than carbon locked up in leaves from the previous growing season. Oxidation of thawed permafrost under rising temperatures could affect the atmospheric signature of $\delta^{13}C$, but those changes will likely progress slowly from one year to the other. Given the large surface area of permafrost in the Northern Hemisphere, together with the current rising temperatures, the proportion of disequilibrium from these areas might increase in the coming decades.

Land use change (LUC) or natural disturbances impact the disequilibrium fluxes when the dominant vegetation switches between C_3 and C_4 discrimination, e.g., conversion of forests into maize fields, or destruction of forests due to wildfires. After such a land cover conversion there is still an isotopic lag in carbon stored in soils that will respire over many years and influence the atmospheric signature. Those LUC effects were studied in detail by *Scholze et al.* [2008]; they quantified the effects of temporal and spatial variability in land use and land cover, with the inclusion of C_4 croplands and pastures. Although LUC had an impact on the global averaged discrimination it was not found to be a large driver of year-to-year changes in disequilibrium; it affected the disequilibrium more gradually.

Contemporary understanding suggests that the terrestrial disequilibrium is primarily driven by the Suess effect, i.e., land-atmosphere respiration is isotopically heavier than photosynthetic uptake. There is recent observational evidence, however, that the disequilibrium can vary seasonally to a point where the disequilibrium flux becomes negative [*Bowling et al.*, 2014]. Although we did not see such variations in SiBCASA, they are likely driven by a strong response in photosynthetic discrimination to environmental conditions and/or additional fractionation processes leading to additional isotopic depletion in the carbon pools. This evidence is interesting as all our budgeting studies clearly show that the global disequilibrium should be at least 20 to 30 % larger in order to close the observed mean δ^{13}C budget, not smaller as the observations of *Bowling et al.* [2014] suggest. This poses a number of interesting questions, and whether or not the negative disequilibrium is unique to some vegetation type, or geographic location, or moisture regime, requires further attention in the future. The issue of a potential lack of variability in discrimination is discussed in the following section.

5.4   Terrestrial discrimination

Terrestrial isotopic discrimination has been a focal point throughout this thesis. In Chapter 2 we used global annual estimates of terrestrial discrimination to explain the combined budget of CO_2 and δ^{13}C. The discrimination is calculated in SiBCASA as a function of stomatal conductance that varies under environmental influence [*Suits et al.*, 2005]. This formulation also accounts for two major metabolic pathways for carbon fixation: C_3 and C_4, according to satellite derived land cover data [*Still et al.*, 2003]. Discrimination influences the atmospheric δ^{13}C values in two ways: (1) it scales directly with the net carbon exchange flux, including fires, and (2) it affects the terrestrial disequilibrium, as outlined in the previous section. We therefore hypothesized in Chapter 2, as in *Alden et al.* [2010], that discrimination could potentially be the primary driver of isotope variability, and thus partially explain the gap in our IAV budget. We considered that variability in respiration and disturbances can affect atmospheric δ^{13}C values but not to the extent that is required to explain all the observed IAV. We therefore investigated the possibility that terrestrial discrimination is more variable than modeled in SiBCASA.

In many earlier double deconvolution studies, discrimination was often considered a constant parameter to facilitate estimation of the net carbon sinks over oceans and land [e.g. *Ciais et al.*, 1995, *Francey et al.*, 1995, *Keeling et al.*, 1989, *Tans et al.*, 1993]. In their double deconvolution, *Randerson et al.* [2002] allowed the terrestrial C_3 discrimination to co-vary with GPP, i.e., an El Niño induced drought anomaly induced reduction in global GPP and discrimination, simultaneously. This required smaller variations in net

ocean and land exchange fluxes to explain changes in atmospheric δ^{13}C. In our budgeting study in Chapter 2, the responses of GPP, net exchange, discrimination and disequilibrium to changing environmental conditions were all solved in one consistent framework (SiBCASA). We confirmed that the global GPP and C$_3$ do co-vary in SiBCASA; i.e., reduced GPP did indeed resulted in reduced discrimination, but to a lesser extent than originally prescribed in the double deconvolution study of *Randerson et al.* [2002].

It has been shown in observations and models that terrestrial discrimination can vary widely in response to environmental influence [*Bowling et al.*, 2002, 2014, *Ehleringer and Cook*, 1998, *Ekblad and Högberg*, 2001, *Ometto et al.*, 2002], as plants open and close their stomata to minimize evaporative water loss [*Farquhar et al.*, 1982]. We showed that varying discrimination resulted in 30 % more IAV in the global disequilibrium flux than in the simulation with fixed C$_3$ discrimination. The absolute increase of the standard deviation in the disequilibrium flux was very limited though; about $0.3\,\mathrm{Pg\,C\,\permil\,yr^{-1}}$, as most of the variability in discrimination originated from annual shifts in the proportion of C$_3$ and C$_4$ productivity. C$_3$ plants discriminate more against ^{13}C because CO$_2$ is fixed by the fractionating enzyme Rubisco, whereas C$_4$ plants mainly fractionate during CO$_2$ diffusion through the leaf stomata. For example, a shift towards more C$_4$ photosynthesis ($\Delta_{\mathrm{C4}} \approx 4\,\permil$) at the expense of C$_3$ photosynthesis ($\Delta_{\mathrm{C3}} \approx 19\,\permil$) leads to smaller global average discrimination. These shifts can be large as the carbon cycle is sensitive to precipitation and temperature in C$_4$ dominated ecosystems [*Knapp and Smith*, 2001]. *Scholze et al.* [2008] observed larger variations in simulations of disequilibrium due to discrimination, but a direct comparison between both studies is difficult. Their baseline simulation contained less than 10 % C$_4$ photosynthesis, whereas we assigned 30 % C$_4$ photosynthesis from additional pastures and crops [*Still et al.*, 2003], which suppressed variability in C$_3$ discrimination estimates. Other differences arose from different amounts of heterotrophic respiration and prescribed turnover times of the carbon pools, which resulted in different isotopic isofluxes.

The simulated discrimination response to climate variability was studied in more detail in Chapter 3. We used, among others, Keeling plot isotope measurements in CO$_2$ respiration from the Biosphere-Atmosphere Stable Isotope Network, BASIN [*Pataki et al.*, 2003]. We tested the response in SiBCASA to answer the following research question, formulated in Section 1.5 on page 16:

RQ3: Does modeled discrimination in photosynthesis respond sufficiently to changes in environmental conditions?

We found that discrimination and the cycle of ^{13}C into and out of vegetation is generally not responsive enough to changes in vapor pressure deficit (VPD) and soil moisture, in comparison to measurements by *Ekblad and Högberg* [2001] and *Bowling et al.* [2002]. Both of these studies found strong correlations between measured humidity and the isotopic composition in CO_2 respiration that follows several days later. SiBCASA's stomatal conductance does respond correctly to variations in humidity, which is reflected in discrimination and consequently in changes to the isotopic composition of CO_2 respiration. The range of these changes (maximum and minimum) is small, however. We observed (1) a generally weak response in discrimination to changes in VPD, (2) latency in recently assimilated carbon to become available for respiration, (3) a possible shortage of environmental stress, and (4) the absence of additional isotope effects that contribute to extra isotopic depletion in the respired CO_2. A stronger response was established after introducing a simple modification to the stomatal conductance formula, i.e., a slight extra decrease in conductance under higher VPD conditions. This steepened the slope of the c_i/c_a ratio to VPD slightly (Figure 3.9b of Chapter 3), but remained reasonable in comparison to tree data [e.g. shown in *Lloyd and Farquhar*, 1994]. The role of stomatal conductance in affecting the terrestrial ^{13}C cycle was also highlighted by *Ballantyne et al.* [2010]. They improved the seasonality of modeled δ_v in comparison to isotope tree-ring observations using a revised stomatal conductance model that was allowed to vary in response to VPD rather than RH [*Leuning*, 1995]. We repeated this experiment in SiBCASA and found that a local covariation between VPD and RH resulted in opposing responses in stomatal conductance and in isotopic signatures of vegetation, δ_v. In some instances the Leuning stomatal conductance model was in better agreement with the isotope tree-ring measurements.

Our study also showed that improvements can be made to SiBCASA's carbon pool configuration. Variation in the isotopic composition of respired CO_2 was strongly dampened due to a relatively long storage pool turnover time from where autotrophic respiration originates. The separation of sugars, with a typical short turnover of around 7 days, from starch improved the variability in respired $\delta^{13}C$ to changes in humidity 3 to 7-fold. Such a configuration was particularly useful in improving the simulation of short-term ^{13}C dynamics, but this is overlooked in terrestrial modeling as it is not necessarily needed when simulating the exchange of total carbon alone.

We also investigated the apparent absence of variability in discrimination from a top-down perspective using CarbonTracker in Chapter 4. Previous studies have sought to improve the simulation of atmospheric CO_2 and $\delta^{13}C$ by adjusting only the net carbon exchange fluxes. We took the novel approach of using measured variations in CO_2 and $\delta^{13}C$ to infer additional drought responses in land discrimination. We formulated the following research question in Section 1.6 on page 19:

RQ4: Are regional droughts detectable by assimilating both CO_2 and $\delta^{13}C$ in an atmospheric inversion?

Over the period 2001 to 2011, we found several occurrences of strong continental-scale droughts causing a larger reduction in land discrimination than originally modeled in SiBCASA. It is an independent indication that variability in land discrimination and carbon uptake is underestimated during extreme droughts, and thus suggests that the vegetation drought response and the isotope discrimination in our biosphere model are inadequate. Besides responses in stomatal conductance, other preliminary results focusing on Eurasia suggest that at least some role is played by the simulation of excessive soil moisture in late summer in SiBCASA, but more work is needed to confirm this with observational data.

The use of atmospheric isotope tracers like $\delta^{13}C$ provided insight into land ecosystem behavior during extreme events. Future modeling efforts of the terrestrial biosphere should therefore focus on the dynamics caused by climate variations. This is particularly important in regard to understanding the coupling between the carbon cycle and climate variability [*Cox et al.*, 2013].

5.5   Inverse modeling

The multi-tracer inversion framework discussed in Chapter 4 is a first attempt to include additional observations of atmospheric $\delta^{13}C$ alongside observations of CO_2 in Carbon-Tracker. One of the main advantages of the CarbonTracker system is that it can handle nonlinear systems using the sequential ensemble Kalman filter approach. It allowed us to optimize discrimination and net terrestrial carbon exchange simultaneously, but not without risks, as the inversion system may lose its ability to track true dynamics under strong nonlinearity. No such failures were fortunately present as the nonlinear inversion resulted in a net exchange and discrimination that was very similar to the sequential linear inversion.

During the development we faced many technical obstacles, and the optimal solutions were formulated in a heuristic manner. We had to negotiate two separate 'atmospheres' in our transport model, and independently calculate a large ensemble of different mole fractions of CO_2 and $^{13}CO_2$ in each. This implementation increased the computational burden, as it required additional processors to handle the increased number of tracers. The correct sampling of $^{13}CO_2$ mole fractions separately from CO_2 and subsequent conversion to $\delta^{13}C$ also necessitated additional changes to the data-assimilation framework.

The working prototype we built can now be used as a testbed for future improvements and additional developments, and can serve as an example for other multi-tracer applications of CarbonTracker, for instance, with CO, CH_4, $\Delta^{14}O$, and $\Delta^{17}O$.

Inside the transport model TM5, we solved for the absolute mass fluxes of $^{13}CO_2$ in units of $kg\,^{13}CO_2\,m^{-2}\,s^{-1}$, rather than the isotopic isofluxes in units of $kg\,CO_2\,‰\,m^{-2}\,s^{-1}$, as done in the more straightforward budgeting study of Chapter 2. This design choice has the advantage that isotopologues of CO_2 are separately emitted, transported, and exchanged, as is the case with any other trace gases simulated in TM5. Total CO_2 and $^{13}CO_2$ mole fractions therefore remain fully consistent and are separately sampled at the designated location and time to estimate $\delta^{13}C$ signatures. This way we avoid the complexity of propagating and transporting $\delta^{13}C$ signatures through the atmosphere, as $\delta^{13}C$ alone is not a conserved quantity in the atmosphere.

In the multi-tracer inversions, we increased the total number of observations with approximately 27,000 additional $\delta^{13}C$ measurements from 53 different sites around the world. It doubled the amount of the weekly CO_2 flask measurements. As a consequence, for the Northern Hemisphere, the terrestrial carbon uptake 1σ uncertainty was lowered by approximately $\pm100\,Tg\,C\,yr^{-1}$ in the multi-tracer inversion, on top of the approximately $\pm900\,Tg\,C\,yr^{-1}$ 1σ uncertainty reduction in the CO_2-only inversion. It seems that the extra uncertainty reduction between prior flux estimates and posterior flux estimates as a result of additional $\delta^{13}C$ measurements was small, however, these values are dependent on the chosen covariance matrices $\mathbf{R}$ and $\mathbf{P}$. Covariance $\mathbf{R}$ specifies how well we 'trust' our measurements, but as this 'trust' is currently higher for CO_2 measurements, the inversion solution is more constrained by CO_2 than $\delta^{13}C$ observations.

As argued for the net exchange fluxes [*Peters et al.*, 2005], there is also need for a better specification of the covariance matrix $\mathbf{P}$ to improve our current discrimination estimates. We made a rudimentary assumption that the structure of $\mathbf{P}$ for discrimination is the same as for CO_2 fluxes, as both parameters are largely driven by the same climate variability influencing the leaf stomata. $\mathbf{P}$ allows correlation structures to constrain indirectly the discrimination of one biome by discrimination of another biome that is directly constrained by measurements. The problem is that the exact nature and magnitude of these correlations are unknown, as discrimination signals might occur across a different range of spatial scales than currently assumed. Regions with sparse or no observational coverage are too dependent upon the prior correlation constraint specified, and their estimates are therefore more uncertain. We focused our analysis thus on the Northern Hemisphere, where the observational coverage was relatively high. Nevertheless, it is important that the number of observations must increase in all regions.

From the bottom-up perspective, there is additional room for improvements and new developments. Currently, the optimization in $^{13}CO_2$ exchange was made purely offline by adjusting existing discrimination fields that scale with terrestrial net exchange. One aspect we did not include in the inversions described in Chapter 4 was the propagation of extra variability in discrimination through the terrestrial disequilibrium term. We therefore forced all additional variability onto the terrestrial net exchange term, whereas in reality extra variability could also originate partly from the disequilibrium flux. To improve our framework we will extend CarbonTracker such that net terrestrial exchange fluxes and discrimination are scaled more dynamically by optimizing parameters inside the photosynthesis parameterization. This would make SiBCASA an active component of the data-assimilation system, and optimally consistent with all constraints at once. Parameters targeted for optimization should be determined via a sensitivity analysis of SiBCASA to find a good signal-to-noise ratio for a possible inversion in the next stage. Potential parameter are, e.g., the slope and intercept of the stomatal conductance formulation that largely determines the gradient of c_i/c_a with increasing VPD. Such changes will affect both the uptake of total CO_2 and the cycling of $^{13}CO_2$ through the coupling with discrimination. As demonstrated in Chapter 3, this gradient might in reality be larger than currently modeled in SiBCASA, especially during droughts. Inversions of this kind can reveal with greater detail the processes inside a biogeochemical model that require improvement.

An important component of data-assimilation is the accurate representation of atmospheric transport of CO_2 and $^{13}CO_2$. It relies on transport in our TM5 model and reanalyzed meteorological data, which represents the meteorological fields on 3-hourly intervals. In addition, the grid resolution, time step, and parameterizations of vertical transport affect our ability to simulate CO_2 and $^{13}CO_2$ accurately. In particular, the inferred discrimination parameter was sensitive to different inversion set ups, more so than the CO_2 fluxes. We had difficulty for instance, in reproducing the same signals in discrimination, particularly during the Europe 2003 drought, using other convective fields in combination with refined zoom resolutions. It indicates that the signal-to-noise found in Chapter 4 is not sufficiently strong. Given the increase in observational data, including the high-frequency tower sampling, combined with advances in terrestrial ^{13}C modeling, we are confident that further improvements can be made to our ability to optimize discrimination. The framework described in this thesis represents a first step towards further integration of new observations in carbon cycle data-assimilation.

5.6   Outlook

This thesis presented new modeling efforts of ^{13}C isotopes of CO_2 to improve our understanding of terrestrial carbon exchange. As argued by *Friedlingstein et al.* [2006] and others, the future fate of the terrestrial carbon cycle is still largely uncertain and this prevents us from making better projections of climate change. Among the uncertainties are the carbon turnover times in land ecosystems. *Welp et al.* [2011] suggested that the current estimates of global GPP, approximately $120\,\mathrm{Pg\,C\,yr^{-1}}$, which are also predicted by SiBCASA, might be too low and could in reality be as large as $175\,\mathrm{Pg\,C\,yr^{-1}}$ to reflect faster turnover of carbon in the pools. Uncertainties in carbon turnover were also underlined by *Carvalhais et al.* [2014] who found that higher precipitation is associated with shorter carbon turnover times, but that global modeled turnover is in fact underestimated. We make a cautious conjecture that if terrestrial respiration (TER) is in fact as large as claimed by *Welp et al.* [2011], it will partly explain the current underestimation in the modeled disequilibrium fluxes, which are a function of TER and ocean CO_2 outgassing. Throughout the thesis we closed the gap by simply scaling the disequilibrium fluxes for oceans and land by 20 to 30 % without taking any physical processes into consideration. We therefore propose that future research efforts should focus more on the modeling of carbon turnover, as it is a crucial component in the terrestrial carbon cycle and δ^{13}C budget.

There is also an urgent requirement for more measurements to quantify GPP and TER, and their drought responses on larger scales. We suggest that particular attention should be paid to the Amazonian carbon balance, as it is an important but poorly understood driver of the global carbon balance. Taking new measurements of CO_2 and their isotopes can help to improve the carbon balance estimation in Amazonia. As discussed in detail in this thesis, variations in GPP due to drought stress are recorded in atmospheric δ^{13}C and can subsequently be interpreted using inverse modeling. Other measurements, such as oxygen isotopes in CO_2 and carbonyl sulfide (COS), could prove to be of great benefit in studying carbon exchange processes like GPP.

The apparent lack of drought response in biosphere models is also a research topic that deserves ongoing attention. Many biosphere models are based on similar parameterizations to estimate exchange of carbon between atmosphere and plant vegetation. The phenology, turnover in predetermined carbon pools, GPP, and climate stress conditions are all driven by similar assumptions, formulations, and data sets. Therefore, the underestimated drought response is not just a feature in our framework, but possibly also present in many other models. It hampers our ability to make better predictions of future climate, as uncertainties in the carbon cycle and its coupling to climate are large. New

innovations in carbon cycle modeling and measuring techniques are thus vital, as they can help us to better constrain the global carbon budget.

Bibliography

Alden, C. B., J. B. Miller, and J. W. C. White (2010), Can bottom-up ocean CO_2 fluxes be reconciled with atmospheric ^{13}C observations?, *Tellus B*, *62*(5), 369–388, doi:10.1111/j.1600-0889.2010.00481.x.

Andres, R. J., G. Marland, T. A. Boden, and S. Bischof (2000), Carbon dioxide emissions from fossil fuel consumption and cement manufacture, 1751-1991, and an estimate of their isotopic composition and latitudinal distribution, in *The Carbon Cycle*, edited by T. Wigley and D. Schimel, pp. 53–62, Cambridge University Press.

Ball, J. T. (1988), An analysis of stomatal conductance, Ph.D. thesis, Stanford University, Stanford, CA, US.

Ballantyne, A. P., J. B. Miller, and P. P. Tans (2010), Apparent seasonal cycle in isotopic discrimination of carbon in the atmosphere and biosphere due to vapor pressure deficit, *Global Biogeochemical Cycles*, *24*(GB3018), doi:10.1029/2009GB003623.

Barbaroux, C., and N. Breda (2002), Contrasting distribution and seasonal dynamics of carbohydrate reserves in stem wood of adult ring-porous sessile oak and diffuse-porous beech trees, *Tree Physiol.*, *22*, 1201–1210.

Beer, C. et al. (2009), Temporal and among-site variability of inherent water use efficiency at the ecosystem level, Global Biogeochem. Cycles, 23, GB2018, doi:10.1029/2008GB003233.

Boden, T. A., G. Marland, and R. J. Andres (2009), Global, regional, and national fossil-fuel CO_2 emissions. carbon dioxide information analysis center, *Carbon Dioxide Information Analysis Center, Oak Ridge National Laboratory, U.S. Department of Energy, Oak Ridge, TN, U.S.A.*, doi:10.5194/acp-10-11707-2010.

Boden, T., G. Marland, and R. Andres (2011), Global CO_2 emissions from fossil-fuel burning, cement manufacture, and gas flaring: 1751-2008, Oak Ridge National Laboratory, U. S. Department of Energy, Carbon Dioxide Information Analysis Center, Oak Ridge, TN, US, doi:10.3334/CDIAC/00001_V2011.

Booth, B. B., C. D. Jones, M. Collins, I. J. Totterdell, P. M. Cox, S. Sitch, C. Huntingford, R. A. Betts, G. R. Harris, and J. Lloyd (2012), High sensitivity of future global warming to land carbon cycle processes, *Environmental Research Letters*, *7*(2), doi:10.1088/1748-9326/7/2/024002.

Bowling, D. R., N. G. McDowell, B. J. Bond, B. E. Law, and J. R. Ehleringer (2002), ^{13}C content of ecosystem respiration is linked to precipitation and vapor pressure deficit, *Oecologia*, *131*, 113–124.

Bowling, D. R., D. E. Pataki and J. T. Randerson (2008), Carbon isotopes in terrestrial ecosystem pools and CO_2 fluxes, *New Phytologist*, *148*, 24–40.

Bowling, D. R., A. P. Ballantyne, J. B. Miller, S. P. Burns, T. J. Conway, O. Menzer, B. B. Stephens, and B. H. Vaughn (2014), Ecological processes dominate the ^{13}C land disequilibrium in a Rocky Mountain subalpine forest, *Global Biogeochem. Cycles*, *28*, 352–370, doi:10.1002/2013GB004686.

Bozhinova, D., M. K. van der Molen, I. R. van der Velde, M. C. Krol, S. van der Laan, H. A. J. Meijer, and W. Peters (2014), Simulating the integrated summertime $\Delta^{14}CO_2$ signature from anthropogenic emissions over Western Europe, *Atmos. Chem. Phys.*, *14*, 7273–7290, doi:10.5194/acp-14-7273-2014.

Brüggemann N., A. Gessler, Z. Kayler, S. G. Keel, F. Badeck, M. Barthel, P. Boeckx, N. Buchmann, E. Brugnoli, J. Esperschütz, O. Gavrichkova, J. Ghashghaie, N. Gomez-Casanovas, C. Keitel, A. Knohl, D. Kuptz, S. Palacio, Y. Salmon, Y. Uchida, and M. Bahn (2011), Carbon allocation and carbon isotope fluxes in the plant-soil-atmosphere continuum: A review, *Biogeosciences*, *8*(11), 3457–3489.

Brugnoli, E., and G. D. Farquhar (2000), Photosynthetic fractionation of carbon isotopes, in *Photosynthesis: Physiology and Metabolism.* edited by R. C. Leegood, T. D. Sharkey, and S. von Caemmerer, pp. 399–434, Kluwer Acad., Norwell, Mass.

Bush, S. E., D. E. Pataki, and J. R. Ehleringer (2007), Sources of variation in δ^{13}C of fossil fuel emissions in Salt Lake City, USA, *Applied Geochemistry*, *22*(4), 715–723.

Carvalhais, N., et al. (2014), Global covariation of carbon turnover times with climate in terrestrial ecosystems, *Nature*, *514*(7521), 213–217.

Chang, R. (2013), Physical Chemistry for the Biosciences, University Science Books, Sausalito, CA, USA.

Ciais, P., P. P. Tans, J. White, and M. Trolier (1995), Partitioning of ocean and land uptake of CO_2 as inferred by δ^{13}C measurements from the NOAA Climate Monitoring

and Diagnostics Laboratory Global Air Sampling Network, *Journal of Geophysical Research*, *100*, 5051–5070.

Ciais, P., et al. (1997), A three-dimensional synthesis study of $\delta^{18}O$ in atmospheric CO_2. 1. Surface Fluxes., *Journal of Geophysical Research - Atmosphere*, *102*, 5857-5872.

Ciais, P., W. Cramer, P. Jarvis, H. Kheshgi, C. Nobre, S. Semenov, W. Steffen (2000), Global Perspective. In: Land Use, Land-Use Change and Forestry, A special report of the Intergovernmental Panel on Climate Change, Cambridge University Press, Cambridge, United Kingdom and New York, NY, USA.

Ciais, P., et al. (2005), Europe-wide reduction in primary productivity caused by the heat and drought in 2003, *Nature*, *437*(7058), 529-533.

Ciais, P., C. Sabine, G. Bala, L. Bopp, V. Brovkin, J. Canadell, A. Chhabra, R. DeFries, J. Galloway, M. Heimann, C. Jones, C. Le Quere, R.B. Myneni, S. Piao and P. Thornton (2013), Carbon and Other Biogeochemical Cycles. In: Climate Change 2013: The Physical Science Basis. Contribution of Working Group I to the Fifth Assessment Report of the Intergovernmental Panel on Climate Change, Cambridge University Press, Cambridge, United Kingdom and New York, NY, USA.

Collatz, G. J., J. Ball, C. Grivet, and J. A. Berry (1991), Physiological and environmental regulation of stomatal conductance, photosynthesis and transpiration: a model that includes a laminar boundary layer, *Agricultural and Forest Meteorology*, *54*, 107–136.

Collatz, G. J., M. Ribas-Carbo, and J. A. Berry (1992), Coupled photosynthesis-stomatal conductance model for leaves of C4 plants, *Aust. J. Plant Physiol.*, *19*(5), 519–538.

Cox, P. M., D. Pearson, B. B. Booth, P. Friedlingstein, C. Huntingford, C. D. Jones, and C. M. Luke (2013), Sensitivity of tropical carbon to climate change constrained by carbon dioxide variability, *Nature*, *1-5*, doi:10.1038/nature11882.

Craig, H., (1953), The geochemistry of stable carbon isotopes, *Geochim. Cosmochim. Acta*, *3*, 53–92.

Craig, H., (1957), Isotopic standards for carbon and oxygen and correction factors for mass-spectrometric analysis of carbon dioxide, *Geochim. Cosmochim. Acta*, *12*, 133–149.

Dai, A., et al. (2012), Increasing drought under global warming in observations and models , *Nature Clim. Change*, *3*, doi:10.1038/nclimate1633.

Dong, X., et al. (2011), Investigation of the 2006 drought and 2007 flood extremes at the Southern Great Plains through an integrative analysis of observations , *Journal of Geophysical Research*, *116*, D03204, doi:10.1029/2010JD014776.

Ehleringer, J. R., and C. S. Cook (1998), Carbon and oxygen isotope ratios of ecosystem respiration along an Oregon conifer transect: Preliminary observations based upon small-flask sampling, *Tree Physiol.*, *18*, 513–519.

Ekblad, A., and P. Hogberg (2001), Natural abundance of ^{13}C in CO_2 respired from forest soils reveals speed of link between tree photosynthesis and root respiration, *Oecologia*, *127*, 305–308, doi:10.1007/s004420100667.

Etheridge, D. M., L. P. Steele, R. L. Langenfelds, R. J. Francey, J. M. Barnola, and V. I. Morgan (2001), Natural and anthropogenic changes in atmospheric CO_2 over the last 1000 years from air in Antarctic ice and firn, *J. Geophys. Res. Atmos.*, 101(D2), 4115–4128, doi:10.1029/95JD03410.

Farquhar, G. D., S. V. Caemmerer, and J. A. Berry (1980), A biochemical-model of photosynthetic CO_2 assimilation in leaves of C_3 species, *Planta*, *149*(1), 78–90.

Farquhar, G. D., M. H. O'leary, and J. A. Berry (1982), On the relationship between carbon isotope discrimination and the inter-cellular carbondioxide concentration in leaves, *Aust. J. Plant Physiol.*, *9*(1), 121–137.

Farquhar, G. D., (1983), On the nature of carbon isotope discrimination in C_4 species, *Aust. J. Plant Physiol.*, *10*(1), 205–226.

Farquhar, G. D., J. R. Ehleringer, and K. T. Hubrick (1989), Carbon isotope discrimination and photosynthesis, *Annual review of Plant Physiology and Plant Molecular Biology*, *40*, 503–537.

Francey, R. J., P. P. Tans, C. E. Allison, I. G. Enting, J. W. C. White, and M. Trolier (1995), Changes in oceanic and terrestrial carbon uptake since 1982, *Nature*, *373*(6512), 326–330.

Francey, R. J., C. E. Allison, D. M. Etheridge, C. M. Trudinger, I. G. Enting, M. Leuenberger, R. L. Langenfelds, E. Michel, and L. P. Steele (1999), A 1000-year high precision record of delta C-13 in atmospheric CO_2, *Tellus, Ser. B*, *51*, 170–193.

Friedlingstein, P. et al. (2006), Climate-Carbon Cycle Feedback Analysis: Results from the C4MIP Model Intercomparison, *Journal of Climate*, *19*, 3337–3353.

Fung, I., C. B. Field, J. A. Berry, M. V. Thompson, J. T. Randerson, C. M. Malmström, P. M. Vitousek, G. James Collatz, P. J. Sellers, D. A. Randall, A. S. Denning, F. Badeck, and J. John (1997), Carbon 13 exchanges between the atmosphere and biosphere, *Global Biogeochemical Cycles*, *11*(4), 507–533.

Furbank, R. T., M. D. Hatch and C. L. D. Jenkins (2000), C_4 Photosynthesis: Mechanism and Regulation, in *Photosynthesis: Physiology and Metabolism.* edited by R. C. Leegood, T. D. Sharkey, and S. von Caemmerer, pp. 399–434, Kluwer Acad., Norwell, Mass.

Garrett, et al. (2011), Complexity in climate-change impacts: an analytical framework for effects mediated by plant disease, *Plant Pathology, 60*(1), 15–30.

Gatti, L. V. et al. (2014), Drought sensitivity of Amazonian carbon balance revealed by atmospheric measurements, *Nature, 506*(7486), doi:10.1038/nature12957.

Gaucher, C., S. Gougeon, Y. Mauffette, and C. Messier (2005), Seasonal variation in biomass and carbohydrate partitioning of understory sugar maple (Acer saccharum) and yellow birch (Betula alleghanienis) seedlings, *Tree Physiol., 25*, 93–100.

Gerbig, C., J. C. Lin, S. C. Wofsy, B. C. Daube, A. E. Andrews, B. B. Stephens, P. S. Bakwin and C. A. Grainger (2003), Toward constraining regional-scale fluxes of CO_2 with atmospheric observations over a continent: 2. Analysis of COBRA data using a receptor-oriented framework, *J. Geoph. Res., 108*, doi:10.1029/2003JD003770, D24.

Giglio, L., J. T. Randerson, G. R. van der Werf, P. S. Kasibhatla, G. J. Collatz, D. C. Morton, and R. S. DeFries (2010), Assessing variability and long-term trends in burned area by merging multiple satellite fire products, *Biogeosciences, 7*(3), 1171–1186.

Greenwood, N. and A. Earnshaw (1997), Chemistry of the Elements, Elsevier Butterworth-Heinemann; 2 edition, Oxford, UK.

Gregg, J. S., R. J. Andres, and G. Marland (2008), China: Emissions pattern of the world leader in CO_2 emissions from fossil fuel consumption and cement production, *Geophys. Res. Lett., 35*, L08806.

Griffiths, H. (2006), Plant biology: Designs on Rubisco, *Nature, 441*, 940–941.

Gruber, N., C. D. Keeling, R. B. Bacastow, P. R. Guenther, T. J. Lueker, M. Wahlen, H. A. J. Meijer, W. G. Mook, and T. F. Stocker (1999), Spatiotemporal patterns of carbon-13 in the global surface oceans and the oceanic Suess effect, *Global Biogeochemical Cycles, 13*(2), 307–335.

Gruber, N., et al. (2002), Oceanic sources, sinks, and transport of atmospheric CO_2, *Global Biogeochemical Cycles, 23*(1), GB1005, doi:10.1029/2008GB003349.

Gurney, K. R., et al. (2002), Towards robust regional estimates of CO_2 sources and sinks using atmospheric transport models, *Nature, 415*, 626–630.

Hartmann, D. L. (1994), Global Physical Climatology, Academic Press, New York, NY, USA.

Herrera, A. (2009), Crassulacean acid metabolism and fitness under water deficit stress: if not for carbon gain, what is facultative CAM good for?, *Annals of Botany, 103*, 645–653.

Hietz, P., W. Wolfgand, and O. Dunisch (2005), Long-term trends in cellulose 13C and water-use efficiency of tropical Cedrela and Swietenia from Brazil , *Tree Physiology*, *25*, 745–752.

Hoag, K. J., C. J. Still, I. Y. Fung, and K. A. Boering (2005), Triple oxygen isotope composition of tropospheric carbon dioxide as a tracer of terrestrial gross carbon fluxes, *Geophys. Res. Lett.*, *32*, L02802. doi:10.1029/2004GL021011.

Indermuhle, A., et al. (1999), Holocene carbon-cycle dynamics based on CO_2 trapped in ice at Taylor Dome, Antarctica, *Nature, 398*, 121–126.

IPCC (2014), Summary for policymakers. In: Climate Change 2014: Impacts, Adaptation, and Vulnerability. Part A: Global and Sectoral Aspects. Contribution of Working Group II to the Fifth Assessment Report of the Intergovernmental Panel on Climate Change, Cambridge University Press, Cambridge, United Kingdom and New York, NY, USA, pp. 1-32.

Jacobson, A. R., N. Gruber, J. L. Sarmiento, M. Gloor, and S. E. Mikaloff Fletcher (2007), A joint atmosphere-ocean inversion for surface fluxes of carbon dioxide: I. Methods and global-scale fluxes, *Global Biogeochemical Cycles*, *21*, doi:10.1029/2005GB002556.

Joos, F., and M. Bruno (1998), Long-term variability of the terrestrial and oceanic carbon sinks and the budgets of the carbon isotopes C-13 and C-14, *Global Biogeochemical Cycles*, *12*(2), 277–295.

Jung, M., M. Reichstein, and A. Bondeau (2009), Towards global empirical upscaling of FLUXNET eddy covariance observations: Validation of a model tree ensemble approach using a biosphere model, *Biogeosciences*, *6*, 2001–2013.

Kaplan, J. O., I. C. Prentice, and N. Buchmann (2002), The stable carbon isotope composition of the terrestrial biosphere: Modeling at scales from the leaf to the globe, *Global Biogeochemical Cycles*, *16*(4), 1060, doi:10.1029/2001GB001403.

Keeling, C. D., R. B. Bacastow, A. E. Bainbridge, C. A. Ekdahl, P. R. Guenther, and L. S. Waterman (1976),Atmospheric carbon dioxide variations at Mauna Loa Observatory, Hawaii, *Tellus, 28*, 538–551.

Keeling, C. D. (1979), The Suess effect: 13Carbon-14Carbon interrelations, *Environment International*, *2*(4-6), 229–300.

Keeling, C. D. and R. Revelle (1985), Effects of El Nino/Southern Oscillation on the atmospheric content of carbon dioxide, *Meteoritics*, *20*(2), 437–450.

Keeling, C. D., R. B. Bacastow, A. F. Carter, S. C. Piper, T. P. Whorf, M. Heimann, W. G. Mook, H. Roeloffzen (1989), A three-dimensional model of atmospheric CO_2 transport based on observed winds: 1. Analysis of observational data, in *Aspects of climate variability in the Pacific and the Western Americas*, edited by D. H. Peterson, pp. 165–236, American Geophysical Union, Washington D.C., United States.

Keenan, T. F., D. Y. Hollinger, G. Bohrer, D. Dragoni, J. W. Munger, H. P. Schmid, A. D. Richardson (2013), Increase in forest water-use efficiency as atmospheric carbon dioxide concentrations rise, *Nature*, doi:10.1038/nature12291

Knapp, A. K. and M. D. Smith (2001), Variation among biomes in temporal dynamics of aboveground primary production, *Science*, *291*, 481–484.

Krol, M., S. Houweling, B. Bregman, M. van den Broek, A. Segers, P. van Velthoven, W. Peters, F. Dentener, and P. Bergamaschi (2005), The two-way nested global chemistry-transport zoom model TM5: algorithm and applications, *Atmos. Chem. Phys. Discuss.*, *4*, 3975–4018.

Kwon, H., E. Pendall, B. E. Ewers, M. Cleary, and K. Naithani (2008), Spring drought regulates summer net ecosystem CO_2 exchange in a sagebrush-steppe ecosystem, *Agricultural and Forest Meteorology*, *148*, 381–391.

Langenfels, R. L., E. Michel, and L. P. Steele (1999), A 1000-year high precision record of $\delta^{13}C$ in atmospheric CO_2, *Tellus*, *51B*, 170–193.

Leegood, R. C. (2000), Introduction, in *Photosynthesis: Physiology and Metabolism.* edited by R. C. Leegood, T. D. Sharkey, and S. von Caemmerer, pp. 1–8, Kluwer Acad., Norwell, Mass.

Le Quere, C., et al. (2003), Two decades of ocean CO2 sink and variability, *Tellus B*, *55*(2), 649–656.

Le Quere, C., et al. (2007), Saturation of the southern ocean CO_2 sink due to recent climate change, *Science*, *316*, 1735–1738.

Leuning, R. (1995), A critical appraisal of a combined stomatal photosynthesis model for C_3 plants, *Plant Cell Environ.*, *18*, 339–355, doi:10.1111/j.1365-3040.1995.tb00370.x.

Levin, I., B. Kromer, M. Schmidt, and H. Sartorius (2003), A novel approach for independent budgeting of fossil fuel CO_2 over Europe by $^{14}CO_2$ observations, *Geophys. Res. Lett.*, *30*(23), 2194, doi:10.1029/2003GL018477.

Lin, G., and J. R. Ehleringer (1997), Carbon isotopic fractionation does not occur during dark respiration in C3 and C4 plants, *Plant Physiol.*, *114*, 391–394.

Lloyd, J., and G. D. Farquhar (1994), ^{13}C discrimination during CO_2 assimilation by the terrestrial biosphere, *Oecolgia*, *99*, 201–215.

Mansfield, T. A., A. J. Travis, and P. G. Jarvis (1981), Responses to light and carbon dioxide, edited by P. G. Jarvis and T. A. Mansfield, in *Stomatal Physiology*, pp. 121–135, Cambridge University Press, Cambridge.

Martin, W., R. Scheibe, and C. Schnarrenberger (2000), The Calvin Cycle and Its Regulation, in *Photosynthesis: Physiology and Metabolism.* edited by R. C. Leegood, T. D. Sharkey, and S. von Caemmerer, pp. 9–52, Kluwer Acad., Norwell, Mass.

Masarie, K. A., and P. P. Tans (1995), Extension and integration of atmospheric carbon-dioxide data into a globally consistent measurement record, *Journal of Geophysical Research-Atmospheres*, *100*(D6), 11,593–11,610.

Meidner, H., and T. A. Mansfield (1968), *Physiology of Stomata*, McGraw-Hill, London

Mook, W. G., J. G. Bommerson, and W. H. Staverman (1974), Carbon isotope fractionation between dissolved bicarbonate and gaseous carbon dioxide, *Earth Planet. Sci. Lett.*, *22*, 169–176.

Moore, A. L., (1977), Photosynthesis and photorespiration, *Nature*, *267*, 307–308.

Mora, C., et al. (2013), The projected timing of climate departure from recent variability, *Nature*, *502*, 183–187.

Mora, C., et al. (2013), Biotic and Human Vulnerability to Projected Changes in Ocean Biogeochemistry over the 21st Century, *PLoS Biol.*, *11*(10), e1001682, doi:10.1371/journal.pbio.1001682.

Myhre, G., D. Shindell, F. M. Breon, W. Collins, J. Fuglestvedt, J. Huang, D. Koch, J. F. Lamarque, D. Lee, B. Mendoza, T. Nakajima, A. Robock, G. Stephens, T. Takemura and H. Zhang (2013), Anthropogenic and Natural Radiative Forcing. In: Climate Change 2013: The Physical Science Basis. Contribution of Working Group I to the Fifth Assessment Report of the Intergovernmental Panel on Climate Change, Cambridge University Press, Cambridge, United Kingdom and New York, NY, USA.

Nakazawa, T., S. Morimoto, S. Aoki, and M. Tanaka (1993), Time and space variations of the carbon isotopic ratio of tropospheric carbon dioxide over Japan, *Tellus*, *45B*, 258–274.

O'Leary, M. H. (1981), Carbon isotope fractionation in plants, *Phytochemistry*, *20*, 553–567.

O'Leary, M. H. (1984), Measurement of the isotopic fractionation associated with diffusion of carbon dioxide in aqueous solution, *J. Phys. Chem.*, *88*, 823–825.

O'Leary, M. H. (1988), Carbon isotopes in photosynthesis, *Bioscience*, *38*, 328–336.

Olson, J. S., J. A. Watts, and L. J. Allsion (1985), Major World Ecosystem Complexes Ranked by Carbon in Live Vegetation: A Database. ORNL/CDIAC-134, NDP-017. Carbon Dioxide Information Analysis Center, U.S. Department of Energy, Oak Ridge National Laboratory, Oak Ridge, Tennessee, U.S.A. (Revised 2001)

Ometto, J. P. H. B., L. B. Flanagan, L. A. Martinelli, M. Z. Moreira, N. Higuchi, and J. R. Ehleringer (2002), Carbon isotope discrimination in forest and pasture ecosystems of the Amazon Basin, Brazil, *Global Biogeochem. Cycles*, *16*(4), 1109, doi:10.1029/2001GB001462.

Orr, J. C., et al. (2005), Anthropogenic ocean acidification over the twenty-first century and its impact on calcifying organisms, *Nature*, *88*, 681–686.

Page, S. E., F. Siegert, J. O. Rieley, H. D. V. Boehm, A. Jaya, and S. Limin (2002), The amount of carbon released from peat and forest fires in Indonesia during 1997, *Nature*, *437*, 61–65, doi:10.1038/nature01131,2002.

Passioura, J. B. (1986), Resistance to drought and salinity: avenues for improvement. *Aust J Plant Physiol*, *13*, 191–201.

Pataki, D. E., J. R. Ehleringer, L. B. Flanagan, D. Yakir, D. R. Bowling, C. J. Still, N. Buchmann, J. O. Kaplan, and J. A. Berry (2003), The application and interpretation of Keeling plots in terrestrial carbon-cycle research, *Global Biogeochem. Cycles*, *17*(1), doi:10.1029/2001GB001850.

Peters, W., J. B. Miller, J. Whitaker, A. S. Denning, A. Hirsch, M. C. Krol, D. Zupanski, L. Bruhwiler, P. P. Tans (2005), An ensemble data assimilation system to estimate CO_2 surface fluxes from atmospheric trace gas observations, *Journal of Geophysical Research*, *110*, D24304, doi:doi:10.1029/2005JD006157.

Peters, W., et. al. (2007), An atmospheric perspective on North American carbon dioxide exchange: CarbonTracker, *PNAS*, *107*(48), 18,925–18,930.

Peters, W., et. al. (2010), Seven years of recent European net terrestrial carbon dioxide exchange constrained by atmospheric observations. *Glob. Change Biol.*, *16*(4), 1317–1337.

Peters, G. P., G. Marland, C. L. Quere, T. Boden, J. G. Canadell, and M. R. Raupach (2012), Rapid growth in CO_2 emissions after the 2008-2009 global financial crisis, *Nature Climate Change*, doi:10.1038/nclimate1332.

Piao, S. et al. (2013), Evaluation of terrestrial carbon cycle models for their response to climate variability and to CO_2 trends, *Global Change Biology*, doi:10.1111/gcb.12187.

Piispanen, R., and P. Saranpaa (2001), Variation of non-structural carbohydrates in silver birch (Betula pendula Roth) wood, *Trees (Berl.)*, *15* doi:10.1007/s004680100125.

Potter, C. S., J. T. Randerson, C. B. Field, P. A. Matson, P. M. Vitousek, H. A. Mooney, and S. A. Klooster (1993), A process-oriented model based on global satellite and surface data, *Global Biogeochem. Cycles*, *7*, doi:10.1029/93GB02725.

Rabinowitch, E., and Govindjee (1969), Photosynthesis, Wiley, New York, 1969.

Ramankutty, N., and J. A. Foley (1998), Characterizing patterns of global land use: An analysis of global croplands data, *Global Biogeochem. Cycles*, *12*(4), 667–686.

Randerson, J. T., M. V. Thompson, C. M. Malmstrom, C. B. Field, and I. Y. Fung (1996), Substrate limitations for heterotrophs: Implications for models that estimate the seasonal cycle of atmospheric CO_2, *Global Biogeochem. Cycles*, *10*(4), 585–602.

Randerson, J. T., C. J. Still, J. J. Balle, I. Y. Fung, S. C. Doney, P. P. Tans, T. J. Conway, J. W. C. White, B. Vaughn, N. Suits and A. S. Denning (2002), Carbon isotope discrimination of arctic and boreal biomes inferred from remote atmospheric measurements and a biosphere-atmosphere model, *Global Biogeochem. Cycles*, *16*(3), 1–15.

Randerson, J. T., et al. (2005), Fire emissions from C_3 and C_4 vegetation and their influence on interannual variability of atmospheric CO_2 and $\delta^{13}CO_2$, *Global Biogeochem. Cycles*, *19*, GB2019, doi:10.1029/2004GB002366.

Rayner, P. J. and R. M. Law (1999), The interannual variability of the global carbon cycle, *Tellus, Ser. B*, *51*(2), 210–212.

Rayner, P. J., M. Scholze, W. Knorr, T. Kaminski, R. Giering, and H. Widmann (2005), Two decades of terrestrial carbon fluxes from a carbon cycle data assimilation system (CCDAS), *Global Biogeochem. Cycles*, *19*(2), 1–20.

Rayner, P. J., R. M. Law, C. E. Allison, R. J. Francey, C. M. Trudinger, and C. Pickett-Heaps (2008), Interannual variability of the global carbon cycle (1992-2005) inferred by inversion of atmospheric CO_2 and $\delta^{13}CO_2$ measurements, *Global Biogeochem. Cycles*, *22*(3), GB3008, doi:10.1029/2007GB003068.

Reynolds, O. (1895), On the dynamical theory of incompressible viscous fluids and the determination of the criterion, *Philosophical Transactions of the Royal Society*, *186*, 123–164.

Rhein, M., S. R. Rintoul, S. Aoki, E. Campos, D. Chambers, R. A. Feely, S. Gulev, G. C. Johnson, S. A. Josey, A. Kostianoy, C. Mauritzen, D. Roemmich, L.D. Talley and F. Wang, (2013), Observations: Ocean. In: Climate Change 2013: The Physical Science Basis. Contribution of Working Group I to the Fifth Assessment Report of the Intergovernmental Panel on Climate Change, Cambridge University Press, Cambridge, United Kingdom and New York, NY, USA.

Rödenbeck, C. S. Houweling, M. Gloor, and M. Heimann (2003), CO_2 flux history 1982-2001 inferred from atmospheric data using a global inversion of atmospheric transport, *Atmos. Chem. Phys.*, *3*, 1919–1964.

Rowlands, D. J., et al. (2012), Broad range of 2050 warming from an observationally constrained large climate model ensemble, *Nature Geoscience*, *5*, 256–260.

Sabine, C. L., et al. (2004), The Oceanic Sink for Anthropogenic CO_2, *Science*, *305*(5682), 367–371.

Saurer, M., R. T. W.. Siegwolf, and F. H. Schweingruber (2004), Carbon isotope discrimination indicates improving water-use efficiency of trees in northern Eurasia over the last 100 years, *Glob. Change Biol.*, *10*, 2109–2120.

Schaefer, K., G. J. Collatz, P. P. Tans, A. S. Denning, I. Baker, J. A. Berry, L. Prihodko, N. Suits, and A. Philpott (2008), Combined Simple Biosphere/Carnegie-Ames-Stanford Approach terrestrial carbon cycle model, *J. Geophys. Res.*, *113*(G3), G03,034, doi:10.1029/2007JG000603.

Schaeffer, S. M., J. B. Miller, B. H. Vaughn, J. W. C. White, and D. R. Bowling (2008), Long-term field performance of a tunable diode laser absorption spectrometer for analysis of carbon isotopes of CO_2 in forest air, *Atmospheric Chemistry and Physics*, *8*, 5263–5277.

Scholze, M., J. O. Kaplan, W. Knorr, and M. Heimann (2003), Climate and interannual variability of the atmosphere-biosphere $^{13}CO_2$ flux, *Geophys. Res. Lett.*, *30*(2), 1097, doi:10.1029/2002GL015631.

Scholze, M., P. Ciais, and M. Heimann (2008), Modeling terrestrial ^{13}C cycling: Climate, land use and fire, *Global Biogeochem. Cycles*, *22*(1), GB1009, doi:10.1029/2006GB002899.

Schulze, E. D., N. C. Turner, T. Gollan, and K. A. Shackel (1987), Stomatal responses, water loss and CO_2 assimilation rates of plants in contrasting environments, edited by O. L. Lange, P. S. Nobel, C. B. Osmond, and H. Ziegler, in *Stomatal Function*, pp. 311–321, Stanford University Press, Stanford, California.

Seibt, U., A. Rajabi, H. Griffiths, and J. A.. Berry (2008), Carbon isotopes and water use efficiency: sense and sensitivity, *Oecologia*, *155*, 441–454.

Sellers, P. J., Y. Mintz, Y. C. Sud, and A. Dalcher (1986), A Simple Biosphere Model (SIB) for use within General Circulation Models, *J. Atmos. Sci.*, *43*, 505–531.

Sellers, P. J., C. J. Tucker, G. J. Collatz, S. O. Los, C. O. Justice, D. A. Dazlich, D. A. Randall, (1994), A global 1∘ by 1∘ NDVI data set for climate studies, part II: The generation of global fields of terrestrial biophysical parameters from NDVI, *Int. J. Remote. Sens.*, *15*(17), 3519–3545.

Sellers, P. J., D. A. Randall, G. J. Collatz, J. A. Berry, C. B. Field, D. A. Dazlich, C. Zhang, G. D. Collelo, and L. Bounoua (1996), A revised land surface parameterization (SiB2) for atmospheric GCMs. Part I: Model formulation, *Journal of Climate*, *9*(4), 676–705.

Sellers, P. J., S. O. Los, C. J. Tucker, C. O. Justice, D. A. Dazlich, G. J. Collatz, D. A. Randall, (1996), A revised land surface parameterization (SiB2) for atmospheric GCMs. Part II: The generation of global fields of terrestrial biophysical parameters from satellite data, *Journal of Climate*, *9*(4), 706–737.

Siegenthaler, U., and H. Oeschger (1987), Biospheric CO_2 emissions during the past 200 years reconstructed by deconvolution of ice core data, *Tellus*, *39B*, 140–154.

Siegenthaler, U., and J. L. Sarmiento (1993), Atmospheric carbon dioxide and the ocean, *Nature*, *365*, 119–125.

Still, C. J., J. A. Berry, G. J. Collatz, and R. S. DeFries (2003), Global distribution of C-3 and C-4 vegetation: carbon cycle implications, *Nature Climate Change*, *17*, 1006–1019.

Suess, H. E. (1955), Radiocarbon concentration in modern wood, *Science*, *122*(3166), 415–417.

Suits, N., A. Denning, J. Berry, and C. Still (2005), Simulation of carbon isotope discrimination of the terrestrial biosphere, *Global Biogeochem. Cycles*, *19*, GB1017, doi: 10.1029/2003GB002141.

Takahashi, T., et al. (2002), Global sea-air CO_2 flux based on climatological surface ocean pCO_2, and seasonal biological and temperature effects, *Deep-Sea Research II*, *49*, 1601–1622.

Takahashi, T., et al. (2009), Climatological mean and decadal change in surface ocean pCO_2, and net sea-air CO_2 flux over the global oceans, *Deep-Sea Research II*, *56*, 554–577.

Tans, P. P. (1980), On calculating the transfer of C-13 in reservoir models of the carbon-cycle, *Tellus*, *32*(5), 464–469.

Tans, P. P., I. Y. Fung, and T. Takahashi (1990), Observational Constraints on the Global Atmospheric CO_2 Budget, *Science*, *247*(4949), 1431–1438.

Tans, P. P., J. A. Berry, and R. F. Keeling (1993), Oceanic $^{13}C/^{12}C$ observations - a new window on ocean CO_2 uptake, *Global Biogeochem. Cycles*, *7*(2), 353–368.

Tarantola, A. (2004), Inverse Problem Theory and Methods for Model Parameter Estimation, Soc. for Ind. and Appl. Math., Philadelphia, Pa.

Thompson, M. V. and J. T. Randerson (1999), Impulse response functions of terrestrial carbon cycle models: method and application, *Global Change Biol.*, *5*, 371–394.

Turner, N. C. (1991), Measurements and influence of environmental and plant factors on stomatal conductance in the field, *Agric. For. Meteorol.*, *54*, 137–154.

van der Velde, I. R., J. B. Miller K. Schaefer, K. A. Masarie, S. Denning, J. W. C. White, P. P. Tans, M. C. Krol, and W. Peters (2013), Biosphere model simulations of interannual variability in terrestrial 13C/12C exchange, *Global Biogeochem. Cycles*, *27*(3), 637–649.

van der Velde, I. R., J. B. Miller K. Schaefer, G. R. van der Werf, M. C. Krol, and W. Peters (2014), Terrestrial cycling of $^{13}CO_2$ by photosynthesis, respiration and biomass burning in SiBCASA, *Biogeosciences*, *11*, 6553–6571.

van der Werf, G. R., J. T. Randerson, G. J. Collatz, and L. Giglio (2003), Carbon emissions from fires in tropical and subtropical ecosystems, *Global Change Biology*, *9*(4), 547–562.

van der Werf, G. R., et al. (2006), Interannual variability in global biomass burning emissions from 1997 to 2004, *Atmospheric Chemistry and Physics*, *6*, 3423–3441.

van der Werf, G. R., J. T. Randerson , L.Giglio, G. J. Collatz, M. Mu, P. S. Kasibhatla, D. C. Morton, R. S. DeFries, Y. Jin, and T. T. van Leeuwen (2010), Global fire emissions and the contribution of deforestation, savanna, forest, agricultural, and peat fires (1997–2009), *Atmospheric Chemistry and Physics*, *10*(23), 11,707–11,735, doi: 10.5194/acp-10-11707-2010.

van Leeuwen, T. T., W. Peters, M. C. Krol, G. R. van der Werf (2013), Dynamic biomass burning emission factors and their impact on atmospheric CO mixing ratios, *Journal of Geophysical Research-Atmospheres*, *118*, 6797–6815.

Vicente-Serrano, S. M., S. Begueria, J. I. Lopez-Moreno (2010), A Multi-scalar drought index sensitive to global warming: The Standardized Precipitation Evapotranspiration Index - SPEI, *Journal of Climate*, *23*, 1696–1718.

Vidale, P., L., and R. Stockli (2005), Prognostic canopy air space solutions for land surface exchanges, *Theor. Appl. Climatol.*, *80*, doi:1007/s00704-004-0103-2.

Wanninkhof, R. (1992), Relationship between wind speed and gas exchange over the ocean, *J. Geophys. Res*, *97*(5), 7373–7382.

Welp, L. R., et al. (2011), Interannual variability in the oxygen isotopes of atmospheric CO_2 driven by El Nino, *Nature*, *477*(7366), 579–582.

Wingate, L., J. Ogee, R. Burlett, A. Bosc, M. Devaux, J. Grace, D. Loustau, and A. Gessler (2010), Photosynthetic carbon isotope discrimination and its relationship to the carbon isotope signals of stem, soil and ecosystem respiration, *New Phytologist*, *188*(2), 576–589.

Winguth, A. M. E., M. Heimann, K. D. Kurz, E. Maierreimer, U. Mikolajewicz, and J. Segschneider (1994), El-nino-southern oscillation related fluctuations of the marine carbon-cycle, *Global Biogeochemical Cycles*, *8*(1), 39–63.

Zhang J., Quay P. D. and Wilbur D. O. (1995), Carbon isotope fractionation during gas-water exchange and dissolution of CO., *Geochim. Cosmochim. Acta*, *59*, 107–114.

Zhang, L., J. Xiao, J. Li, K. Wang, L. Lei, and H. Guo (2012), The 2010 spring drought reduced primary productivity in southwestern China, *New Phytologist*, *188*(2), 576–589. *Environ. Res. Lett. 7*, 045706, doi:10.1088/1748-9326/7/4/045706.

Zhang, H. F., et al. (2014), Estimating Asian terrestrial carbon fluxes from CONTRAIL aircraft and surface CO_2 observations for the period 2006–2010, *Atmos. Chem. Phys. 14*, 5807–5824.

Summary

Making predictions of future climate is difficult, mainly due to large uncertainties in the carbon cycle. The rate at which carbon is stored in the oceans and terrestrial biosphere is not keeping pace with the rapid increase in fossil fuel combustion and deforestation, resulting in an increase of atmospheric carbon dioxide (CO_2). To gain a better understanding of the global carbon cycle we need to combine multiple sources of data into one consistent analysis, such as, forest and agricultural statistics, satellite data, atmospheric and ecological observations, and mechanistic models. This thesis describes fundamental research on some of the key components of the terrestrial carbon cycle, i.e., gross primary production (GPP) and terrestrial ecosystem respiration (TER) of CO_2, which forms the key to improved prediction of net exchange. Droughts have been shown to strongly influence this exchange, and to interpret these responses adequately we have turned to a large collection of new atmospheric observations of CO_2, and its ^{13}C isotope ($^{13}CO_2$), to constrain key model components.

In Chapter 2 we studied the global budget of atmospheric CO_2 and the ratio of $^{13}CO_2/^{12}CO_2$ ($\delta^{13}C$) and investigated the main terrestrial drivers of interannual variability (IAV) responsible for the observed atmospheric $\delta^{13}C$ variations. In this chapter we introduced the SiBCASA biogeochemical model, that we provided with a detailed isotopic discrimination scheme (to calculate the natural preference of $^{12}CO_2$ over $^{13}CO_2$ in uptake processes), separate ^{12}C and ^{13}C biogeochemical pools, and satellite-observed fire disturbances. This model was able to calculate uptake of $^{13}CO_2$ and $^{12}CO_2$ and produced return fluxes from its differently aged carbon pools, contributing to the so-called disequilibrium flux. Our simulated terrestrial isotope processes, plant discrimination and disequilibrium, closely resembled previously published values and similarly suggested that discrimination variations in C_3 type plants and year-to-year variations in C_3 and C_4 productivity are the main drivers of IAV. The year-to-year variability in the terrestrial disequilibrium flux was much lower than required to match variations in atmospheric observations, under the common assumption of low variability in net ocean CO_2 exchange, constant discrimination, and a closed CO_2 budget. It was unclear how to increase IAV in the terrestrial

biosphere, which suggested that SiBCASA missed adequate drought responses resulting in a latent isotope discrimination and variability in C_3/C_4 plant productivity.

Implementation of carbon isotope cycling, biomass burning, and SiBCASA's drought response were closely studied in Chapter 3. Our biomass burning emissions were similar as in CASA-GFED; both in magnitude and spatial patterns, and the implementation of isotope exchange gave a global mean discrimination value of approximately 15 ‰, and varied spatially depending on the photosynthetic pathway in the plant. These values compared well (annually and seasonally) with other published results. Similarly, the size of the terrestrial isotopic disequilibrium was close to that of other studies. As plants experience drought stress, they respond by closing their stomata to prevent the loss of water. This process also inhibits the uptake of CO_2 and reduces the isotope discrimination against $^{13}CO_2$ molecules. We found that the amplitude of drought response in SiBCASA was smaller than suggested by the measured isotope signatures. We also found that a slight increase in stomatal closure for large vapor pressure deficits amplified the variations in the respired isotope signature. Finally, we saw the need for modified starch/sugar storage pools to improve the propagation of isotopic discrimination anomalies to respiration on short-term time scales.

In Chapter 4 we developed a multi-tracer inversion system to interpret signals in atmospheric CO_2 and $\delta^{13}C$ observations simultaneously. We wanted to know whether drought stress in plants can induce changes in atmospheric $\delta^{13}C$ and whether they are interpretable. Using inverse modeling we were able to refine the discrimination parameter for plants as it reflected detectable variations in atmospheric $\delta^{13}C$. The results showed that the isotope discrimination values were consistently smaller during large severe droughts in the Northern Hemisphere, exceeding the estimates from SiBCASA (i.e., a larger reduction). Decreased discrimination suggested an increase in the regional intrinsic water use efficiency, which was also recorded at a large number of measurement sites. The IAV in net ecosystem exchange was relatively insensitive as we allowed the variability of the discrimination parameter to increase more than 8-fold, but it also allowed significant correlation between annual net exchange and discrimination. This study suggested a larger effect of droughts on discrimination than previously thought and that the treatment of drought response in biosphere models needs to be improved.

Carbon cycle research is far from complete as many components are still largely uncertain, which prevents us from making better predictions of future climate. This thesis, however, highlights the importance of isotope observations to assess and improve biogeochemical models, especially with regard to the allocation and turnover of carbon, and responses to droughts.

Samenvatting

Het maken van nauwkeurige voorspellingen van ons toekomstig klimaat is vooral lastig door grote onzekerheden in de huidige koolstofcyclus. De snelheid waarmee koolstof wordt opgeslagen in de natuurlijke reservoirs; oceanen en de landecosystemen houdt geen gelijke tred met de snel toenemende ontbossing en verbranding van fossiele brandstoffen. Om de mondiale koolstofcyclus beter te begrijpen moeten we meerdere informatiestromen gaan combineren die samen tot een betere en consistentere analyse leiden. Voorbeelden zijn; bos- en agrarische koolstofstatistieken, satellietinformatie die plantengroei in kaart brengt, metingen van koolstof in de atmosfeer en in ecosystemen, en computermodellen. Dit proefschrift beschrijft nieuw fundamenteel onderzoek naar een aantal belangrijke on-derdelen van de koolstofcyclus over land; de totale koolstofopname en de totale koolstof-afgifte, die samen de sleutel vormen om de netto-uitwisseling van CO_2 beter te kunnen voorspellen. Met name grootschalige droogtes beïnvloeden sterk de netto uitwisseling van CO_2 en om dit beter te begrijpen zullen we metingen van CO_2, en de koolstof-13 isotoop van CO_2 ($^{13}CO_2$) nader analyseren. De opname van $^{13}CO_2$ moleculen door planten en oceanen gaat net iets minder makkelijk dan de opname van de lichtere $^{12}CO_2$ moleculen. Deze voorkeur ten nadele van $^{13}CO_2$ wordt ook wel isotopen-discriminatie genoemd.

In Hoofdstuk 2 beschrijven wij het onderzoek naar de mondiale koolstofbalans van CO_2 in de atmosfeer en de verhouding van koolstofisotopen $^{13}CO_2/^{12}CO_2$ ($\delta^{13}C$). We waren met name geïnteresseerd naar de belangrijkste factoren die verantwoordelijk zijn voor de jaar-tot-jaar variabiliteit in de gemeten $\delta^{13}C$ waarden in de atmosfeer. In dit hoofdstuk introduceren we het SiBCASA model dat in staat is plantengroei en uitwisseling van CO_2 en water te simuleren op mondiale schaal. Dit model hebben we voorzien van een gede-tailleerde isotopen-uitwisselingsmodule om de opname van $^{13}CO_2$ te berekenen, aparte koolstof-13 compartimenten om de hoeveelheid koolstof-13 biomassa te bepalen, en als laatste een nieuwe module om bosbranden te simuleren. Dit model is zowel in staat om de fotosynthese-opname van $^{13}CO_2$ en $^{12}CO_2$ te berekenen, als de afgifte door verbrand-ing van biomassa en natuurlijke koolstofafbraak. Deze laatste draagt bij aan de zoge-naamde isotopen *disequilibrium flux*. De gesimuleerde uitwisseling van koolstofisotopen

door processen zoals isotopen-discriminatie leek sterk op eerder gepubliceerde waarden. De belangrijkste aanjagers van variabiliteit in isotopen-discriminatie zijn: vochtgehalte in de lucht dat de opening van de huidmondjes in het blad beïnvloedt, en jaar-tot-jaar variaties in de productiviteit van verschillende type planten. De variabiliteit in de gesimuleerde isotopenflux was te klein om variaties in de metingen te verklaren, gegeven het feit dat de variabiliteit van CO_2-uitwisseling in de oceanen sowieso klein is. Het onderzoek maakte duidelijk dat SiBCASA mogelijk onvoldoende reageert op grootschalige droogtes waardoor zowel discriminatie-effecten als de variabiliteit van ecologische productiviteit onderschat worden.

Hoe de koolstofisotopen-uitwisseling, de biomassa-verbrandingsemissies, en de mate SiBCASA reageert op droogtes wordt in Hoofdstuk 3 meer uitgebreid bestudeerd. Onze verbrandingemissies waren vergelijkbaar met de gepubliceerde waarden van CASA-GFED; zowel in omvang als de ruimtelijke spreiding. De isotopen-uitwisseling gaf een mondiaal gemiddelde discriminatie van circa 15 ‰ en varieerde afhankelijk van de plantensoort en het fotosyntheseproces. Ook deze waarden waren vergelijkbaar (per jaar en per seizoen) met andere gepubliceerde resultaten. De grootte van de isotopen disequilibrium lag eveneens dicht bij die van andere studies. Als planten droogtestress ervaren proberen ze vochtverlies te verminderen door de huidmondjes te sluiten. Echter, dit remt ook de opname van CO_2 en vermindert de isotopen-discriminatie van $^{13}CO_2$ moleculen. We vonden in vergelijking met gemeten $\delta^{13}C$ waarden dat de droogterespons in ons model in sommige gevallen onvoldoende was. Met een kleine aanpassing in het model konden we de huidmondjes iets meer afknijpen tijdens een sterke droogte en dat gaf meer consistente $\delta^{13}C$ waarden in de atmosfeer die beter overeenkwamen met beschikbare metingen. Tot slot zagen we de noodzaak om binnen ons model de nabootsing van zetmeel- en suikerreserves in planten te verbeteren zodat koolstofisotopen nauwkeuriger verplaatst worden binnen de plant.

In Hoofdstuk 4 beschrijven wij een multitracer-inversiesysteem om gemeten waarden van CO_2 en $\delta^{13}C$ zo te interpreteren dat we nieuwe consistente fluxen kunnen afleiden. We wilden weten of droogtestress bij planten specifiek invloed heeft op de atmosferische $\delta^{13}C$ waarden. Met behulp van dit inversiesysteem, dat gekoppeld is aan een atmosferisch transportmodel, waren we in staat om de isotopen-discriminatieparameter zo te verfijnen dat de variaties in de atmosferische $\delta^{13}C$ beter overeenkwamen met de daadwerkelijke metingen. De resultaten toonden aan dat de isotopen-discriminatie elke keer kleiner wordt tijdens een grootschalige droogte op het noordelijk halfrond die de oorspronkelijke schattingen van SiBCASA overtroffen. Daling in isotopen-discriminatie betekende ook dat het rendement van watergebruik in planten moest toenemen. Dit gedrag werd ook waargenomen bij een groot aantal meetpunten. De jaar-tot-jaar variabiliteit van isotopen-discriminatie nam sterk toe (8 maal) zonder dat het veel invloed

had op de CO_2-uitwisseling zelf. Ook zagen we een sterke toename in de correlatie tussen de CO_2-uitwisseling en isotopen-discriminatie. Onze studie laat zien dat grootschalige droogtes een grotere invloed hebben op isotopen-discriminatie wat suggereert dat de droogterespons in CO_2-uitwisselingsmodellen moet worden verbeterd.

Het onderzoek naar de koolstofcyclus is nog lang niet afgerond, zeker gezien de onzekerheden die nog steeds gelden op CO_2-uitwisselingsprocessen. Daardoor is het nog steeds moeilijk om een nauwkeurige voorspelling te maken van ons toekomstig klimaat. Echter, dit proefschrift benadrukt het belang en de toegevoegde waarde van isotopenwaarnemingen om CO_2-uitwisselingsmodellen te evalueren, in het bijzonder gedurende droogtestress.

Dankwoord

Zo, klaar! Mijn proefschrift is af. Een project met de gebruikelijke hoogte- en dieptepunten, momenten van euforie en momenten dat je aan stoppen denkt. Maar gelukkig heb ik veel steun gekregen en dat verdient natuurlijk een dankwoordje. Als eerste wil ik mijn promotor en dagelijkse begeleider Wouter Peters bedanken. Jij haalde het NWO VIDI-voorstel binnen, waardoor ik aan dit promotieonderzoek kon werken. Je enthousiasme voor het onderzoek en onderwijs was altijd erg aanstekelijk. Ook tijdens moeilijke momenten bleef je vertrouwen tonen, wat voor mij een belangrijke stimulans was om het onderzoek af te ronden. Je had ook de bijzondere gave om de meest complexe concepten eenvoudig uit te leggen, hetgeen mij enorm hielp bij het eigen maken van deze moeilijke materie. Mijn andere promotor, Maarten Krol, wil ik eveneens bedanken voor het gegeven vertrouwen en de motiverende gesprekken. Je scherpe oog voor detail en je uitgebreide suggesties en opbouwende kritiek op mijn artikelen en hoofdstukken heb ik altijd erg gewaardeerd. Maarten en Wouter, ik wil jullie samen ook bedanken voor de gastvrijheid en de gezelligheid buiten de werkvloer.

Special thanks go to my co-promotor John Miller. Your knowledge on ^{13}C isotopes and CO_2 inversions were invaluable during my thesis research. I am grateful for the wonderful month we spent working together at NOAA. I was especially impressed with the ease at which you passed your knowledge onto me. I am also sincerely grateful to Kevin Schaefer. Thanks for your hospitality, your support, and the many insights you provided on the SiBCASA model.

Natuurlijk bedank ik ook de MAQ-crew, alle (oud-) collega's, voor de steun en discussies op de werkvloer, maar ook voor de gezelligheid, voor het frisbeeën tijdens de lunchpauzes, de afdelingsuitjes, de filmavonden, de pub-quizavonden en ga zo maar door. Toch wil ik in het bijzonder Kees van den Dries en Caroline Wiltink bedanken voor alle technische en administratieve ondersteuning. Ik bedank ook Huug Ouwersloot en Eduardo Bárbaro voor de fijne samenwerking rond de ontwikkeling en organisatie van onze zomerschool.

Pete - Oi! Oi! Thanks for being my paranympf and proofreader. You were of great help and support, and you always encouraged me to see it through to the end. I'm

looking forward to getting together for a proper UFC night with some Laurel Aitken in the background, just like the good old days. Beers and cheers bro!

Mijn zusje Lara, ook jij bedankt dat je mijn paranimf wilt zijn, maar natuurlijk ook voor je tomeloze inzet en tijd die je gestoken hebt in het maken van het kaftontwerp. Het is heel mooi geworden, bedankt! Pap, mam en mijn andere zusjes, ook jullie bedankt voor alle steun en kansen die jullie mij geboden hebben. Hopelijk begrijpen jullie nu een beetje waar ik al die jaren aan werkte.

Als laatste natuurlijk mijn steun en toeverlaat Magdalena. Zonder jou was dit alles nooit mogelijk geweest. Ik dank je voor je geduld en vertrouwen. Teraz czas nauczyć się polskiego.

List of publications

Verkley, W. T. M. and I. R. van der Velde (2010), Balanced dynamics in the Tropics. *Q. J. R. Meteorol. Soc.*, *136*, 41–49, doi:10.1002/qj.530.

Van der Velde, I. R., G. J. Steeneveld, B. G. J. Wichers Schreur, and A. A. M. Holtslag (2010), Modeling and Forecasting the Onset and Duration of Severe Radiation Fog under Frost Conditions, *Mon. Wea. Rev.*, *138*, 4237–4253, doi:http://dx.doi.org/10.1175/2010MWR3427.1

Van der Velde, I. R., J. B. Miller K. Schaefer, K. A. Masarie, S. Denning, J. W. C. White, P. P. Tans, M. C. Krol, and W. Peters (2013), Biosphere model simulations of interannual variability in terrestrial 13C/12C exchange, *Global Biogeochem. Cycles*, *27*(3), 637–649, doi:10.1002/gbc.20048

Van der Velde, I. R., J. B. Miller K. Schaefer, G. R. van der Werf, M. C. Krol, and W. Peters (2014), Terrestrial cycling of $^{13}CO_2$ by photosynthesis, respiration and biomass burning in SiBCASA, *Biogeosciences*, *11*, 6553–6571, doi:10.5194/bg-11-6553-2014, 2014.

Bozhinova, D., M. K. van der Molen, I. R. van der Velde, M. C. Krol, S. van der Laan, H. A. J. Meijer and W. Peters (2014), Simulating the integrated summertime $\Delta^{14}CO_2$ signature from anthropogenic emissions over Western Europe, *Atmos. Chem. Phys.*, *14*, 7273–7290, doi:10.5194/acp-14-7273-2014, 2014.

Netherlands Research School for the
Socio-Economic and Natural Sciences of the Environment

D I P L O M A

For specialised PhD training

The Netherlands Research School for the
Socio-Economic and Natural Sciences of the Environment
(SENSE) declares that

Ivar van der Velde

born on 9 March 1983 in Bennekom, The Netherlands

has successfully fulfilled all requirements of the
Educational Programme of SENSE.

Wageningen, 5 June 2015

the Chairman of the SENSE board

Prof. dr. Huub Rijnaarts

the SENSE Director of Education

Dr. Ad van Dommelen

The SENSE Research School declares that **Mr Ivar van der Velde** has successfully fulfilled all requirements of the Educational PhD Programme of SENSE with a work load of 45 EC, including the following activities:

SENSE PhD Courses

o SENSE Autumn School: 'Biogeochemistry and -physics of the lower atmosphere', Cyprus (2010)
o Environmental Research in Context, Apeldoorn (2011)
o Research in Context Activity: 'Co-organising course: Bridging the gap between atmospheric scales', Wageningen (2012)
o Bridging the gap between atmospheric scales, Wageningen (2012)

Other PhD and Advanced MSc Courses

o PhD course Scientific Writing (2011)

Management and Didactic Skills Training

o Teaching practical 'Earth system model PlanetSimulator' (2011)
o Teaching practical 'Climate regulation of fire emissions in equatorial Asia' (2012)
o Providing training at University of Edinburgh School of GeoSciences on adding fire emissions into their terrestrial biosphere model DALEC (2014)

Oral Presentations

o *Using atmospheric observations to estimate the surface $^{13}CO_2$ exchange*. Buys Ballot Research School (BBOS) Autumn Symposium, 28-30 October 2009, Oisterwijk, The Netherlands
o *Interpreting global CO_2 exchange processes using observed isotopic signals.* Sense Symposium, 9 March 2010, Wageningen, The Netherlands
o *Using 13CO2 as an extra carbon balance constraint in CarbonTracker*. TransCom Meeting, 4-8 June 2012, Nanjing, China
o *Using $^{13}CO_2$ as an extra carbon balance constraint in CarbonTracker*. AGU Fall Meeting 2012, 3-7 December 2012, San Francisco, United States

SENSE Coordinator PhD Education

Dr. ing. Monique Gulickx